A search for new physics in the $\gamma\gamma$ channel with the ATLAS experiment at $\sqrt{s} = 7\,\text{TeV}$

Thesis submitted in accordance with

the requirements of the University of Liverpool

for the degree of Doctor in Philosophy

by Peter Malcolm Waller

July 2013

UNIVERSITY OF LIVERPOOL

To my partner, Ona,

and my parents, Patrick and Jean.

Without whose moral support

I couldn't have made it here.

A search for new physics in the $\gamma\gamma$ channel with the ATLAS experiment at $\sqrt{s} = 7\,\text{TeV}$

by Peter Malcolm Waller

July 2013

Abstract

In this thesis, the diphoton invariant mass distribution $m_{\gamma\gamma}$ is measured using data collected with the ATLAS detector at the LHC during 2011. The integrated luminosity collected suitable for data analysis during this time was $L = 4.9\,\text{fb}^{-1} \pm 1.3\%$. The properties of the $m_{\gamma\gamma}$ distribution are studied by observing the data in a control region $140\,\text{GeV} < \text{m}_{\gamma\gamma} < 400\,\text{GeV}$. A statistical procedure is used to search the $m_{\gamma\gamma}$ distribution for the presence of a statistically significant excess of events in a generalised manner. The p-value for this search is 0.734 ± 0.004, which is consistent with the null hypothesis. The 95% Bayesian limit on the cross-section times branching ratio of the Randall Sundrum graviton decaying to diphotons $\sigma \times \text{Br}\left(G \rightarrow \gamma\gamma\right)$ in the data, along with the expected limit, is determined as a function of mass with a coupling parameter of $k/\overline{M_{\text{pl}}} = 0.1$. The exclusion limits are recast to other values of $k/\overline{M_{\text{pl}}}$ by scaling the cross-section limit according to its theoretical dependence of the cross-section on $k/\overline{M_{\text{pl}}}$. The parameters of the Randall Sundrum model are bounded by the analysis with approximately $m_G > 1\,\text{TeV}$ for $k/\overline{M_{\text{pl}}} = 0.01$ and $m_G > 2\,\text{TeV}$ for $k/\overline{M_{\text{pl}}} = 0.1$.

Declaration

No portion of the author's work described in this thesis has been submitted in support of an application for another degree or qualification in this, or any other, institute of learning.

Synopsis

Mountains are not climbed nor marathons run merely to reach a geographical location — there are much easier ways to accomplish these feats — but as personal and spiritual challenges to the participants.

DAVID STEIN

Fundamental physics has a long-standing problem called the "*Hierarchy Problem*": that the forces of nature have very different strengths. Gravity is weaker than the strong force by almost 40 orders of magnitude and there is no obvious theoretical reason for this. One possible solution is a model proposed by Randall and Sundrum, which is tested in this thesis. This model postulates the existence of extra dimensions of space which dilute the gravitational force to its observed magnitude. It also predicts the existence of additional massive gravitons which could be produced in high energy collisions and detected through their decays to lighter particles; hence the validity of the model may be discerned through experiment.

The LHC collides protons, the products of which were observed with the ATLAS detector over the course of 2011. Approximately 700 trillion proton collisions are estimated to

have taken place, of which about 400 million were recorded on disk after passing a real-time selection made by hardware and software triggers. The trigger system is designed to mitigate physical and experimental backgrounds for a range of physics signatures. Once recorded, the data are available for repeated interrogation ("*offline*").

Proton collisions result in interactions of fundamental particles such as quarks and gluons. In a small fraction of such interactions according to the kinematics of the interaction, a graviton can form and then decay to pairs of particles which would have a large invariant mass $m_{\gamma\gamma}$. This thesis studies the decay of the graviton to two photons, $\gamma\gamma$, where the $\gamma\gamma$ have an $m_{\gamma\gamma} > 400\,\mathrm{GeV}$. In order to solve the hierarchy problem, the mass of the graviton is expected to lie at a scale of $\mathcal{O}\,(1\,\mathrm{TeV})$.

The graviton model has two parameters whose values are unknown from first principles; the "*mass of the graviton*", m_G, and the so-called *"coupling parameter"*, $k/\overline{M}_{\mathrm{pl}}$, which influences the cross-section and resonance width of the graviton in its $m_{\gamma\gamma}$ distribution. The search therefore proceeds by measuring the $m_{\gamma\gamma}$ distribution and obtaining an estimate of the contribution from background processes.

There are two types of background events which contaminate the measured $m_{\gamma\gamma}$ distribution. There are sources of background whose physics signature is the same as that of the signal. These are indistinguishable through any measurement and are referred to as the "*irreducible*" background. Then there are physics signatures which are different from the graviton, but the measured detector signature is such that they may be reconstructed as a signal event. This is called the "*reducible*" background.

The selection rejects some fraction of signal events (also irreducible background) and accepts a fraction of reducible background events. The fraction of signal events accepted is

the "*efficiency*" and fraction accepted which are signal is called the "*purity*". The expected irreducible background is estimated using the PYTHIA 6 Monte Carlo physics generator, the output of which is run through a full GEANT 4 ATLAS detector simulation. The generated $m_{\gamma\gamma}$ distribution is re-weighted so that it reproduces the shape predicted by the DIPHOX generator, a Monte Carlo generator based on Next-to-Leading order Standard Model direct diphoton cross-sections. It is not possible to simulate the reducible background with a useful amount of statistics owing to the computational expense of the detector simulation; along with the high frequency of potential reducible background events and the rarity with which a given background event will contribute to the reducible background by faking a photon signal.

To determine the reducible background from data, a set of events dominated by reducible background is obtained by requiring that certain selection criteria fail. A template fit method is then used on the isolation distribution of this set. This method determines the shape of the background isolation distribution and then normalizes it to the total isolation distribution in a region known to be dominated by the background. This allows the background component to be subtracted from the total to obtain an estimate of the shape of the signal component. A two-dimensional template fit in the two-photon isolation distribution is then performed using the shapes obtained from the background subtraction; obtaining the relative yields of the different components of the background.

The total background estimate for the $m_{\gamma\gamma}$ distribution is then determined by summing the reducible and irreducible shapes weighted according to the yields obtained from the template fit and normalizing to the data in a control region $140\,\text{GeV} < m_{\gamma\gamma} < 400\,\text{GeV}$. The irreducible shape is determined directly from the PYTHIA 6 estimate re-weighted to

DIPHOX. The reducible component consists of three sub-components, each of which is determined with a fit to the data distribution in background-dominated control samples.

Once the total background estimate has been obtained, a statistical procedure known as the BUMPHUNTER is used to search for an excess in the data in a generalized manner. It looks in many possible windows for an excess and takes into account the so called "*look-elsewhere effect*", an issue that can falsely enhance the apparent significance of an excess. The p-value of the BUMPHUNTER statistic in the data was measured to be 0.734 ± 0.004, which is consistent with the null hypothesis, *i.e.* that the data does not contain a significant excess.

The BAYESIAN ANALYSIS TOOLKIT is used to obtain a 95% upper limit on the number of signal events N_{signal} present in the data along with the expected limit as a function of m_G. To obtain this limit, templates of the reconstructed detector $m_{\gamma\gamma}$ distribution of the graviton with $k/\overline{M_{\text{pl}}} = 0.1$ are used. This is cast in terms of a cross-section times branching ratio $\sigma \times \text{Br}\left(G \to \gamma\gamma\right)$ and then in terms of the Randall Sundrum theory through the PYTHIA 8 cross-section prediction for this process with an NLO k-factor supplied by theorists. The result is an exclusion region in the $m_G - k/\overline{M_{\text{pl}}}$ plane.

The presence of the Randall Sundrum graviton model is excluded by the above technique with an m_G lower than approximately 1 TeV and 2 TeV at a $k/\overline{M_{\text{pl}}}$ of 0.01 and 0.1 respectively.

Contents

List of Figures

List of Tables

Chapter 1

Introduction

Research is what I'm doing when I don't know what I'm doing.

WERNHER VON BRAUN

The graviton is the only force carrier which has not been directly observed. The particle's existence follows from theories which attempt to describe gravity. A straightforward interpretation of our current knowledge of the universe would lead us to conclude that gravity is far too weak to ever be observed at a collider experiment.

Gravitons could be produced through processes such as matter-antimatter annihilation; they would then decay through pair-production. This process would occur with a rate in proportion to the strength of the force. Gravity is a much weaker force than the other three known forces; the so-called "*weak*" force is 10^{25} times stronger. New physics notwithstanding, gravitational interactions should happen with a frequency of order 10^{25} times less than the weak force.

It is impossible in these circumstances to create a graviton at the LHC, or observe one with any experiment that can be imagined [1]. However, fundamental physics has a significant open problem; resolving it may also allow for models which have significantly increased rates of graviton production.

1.1 Searches in particle physics

There are many ways to discover new fundamental physics. Broadly, they divide into two categories: direct and indirect searches. A direct search looks for an excess in the number of measured events and an indirect search might involve looking at preferred values of a fit or the evolution of parameters measured from the data. Both methods make a prediction for a quantity (*e.g*, the rate at which a process occurs), and compare the measured value with the prediction.

The Randall Sundrum (RS) model, which will be tested in this thesis, predicts gravitons that will decay to two photons within a narrow window at an invariant mass of $\mathcal{O}(1\,\text{TeV})$; by comparison the Higgs lives at $\mathcal{O}(.125\,\text{TeV})$. In these circumstances, a direct counting experiment can be used to discover or put constraints on the model. Typically, we aim to either discover a model by excluding the null hypothesis with a large probability, or state an exclusion limit. Placing an exclusion limit for the RS search involves determining the largest cross-section that the process could have and still lead to the null hypothesis 95% of the time.

In the absence of background and detector effects, the problem is conceptually simple. The null hypothesis would require that no events are observed; measuring one or more events would lead to a discovery. An upper limit on the cross-section could be derived using a frequentist approach by taking a Poisson distribution and testing all possible mean values of the distribution to see how many events one would expect to observe in each case.

In reality, there are background processes, which contribute to the measured number of events. An effort is made to reduce the number of background events that which are counted, but this is only possible probabilistically. In these cases it is necessary to estimate the amount of background we would expect given the Standard Model. For irreducible backgrounds, it is physically impossible to distinguish them from events of interest.

1.2 Aims and objectives of this research

This research implements an analysis using data collected by the ATLAS experiment during 2011. A measurement is made of the $\gamma\gamma$ cross-section and cast in terms of the excluded region of the Randall Sundrum graviton model. To make this measurement an estimate for the production cross-section of $\gamma\gamma$ background processes is obtained.

The structure of this document is as follows: chapter 2 outlines the theoretical motivation for the Randall Sundrum graviton, how it might be detected, and what the backgrounds to its measurement are. The experimental apparatus is discussed in chapter 3 and the quality requirements imposed on the data collected are covered in chapter 4. In chapter 5 the data samples and simulations used are specified. Chapter 6 covers how the photons are observed by the detector and how they are discriminated from the background; the cuts placed on the data are in chapter 7. The expected background and signal are determined in chapter 8. Systematic uncertainties impacting the analysis are discussed in chapter 9. The statistical procedure used to search for new physics is detailed chapter 10, along with the method used for setting an exclusion bound on the number of signal events present in the data. The results are presented in chapter 11.

Chapter 2

Theory

Confidence: The feeling you have before you understand the situation.

ANONYMOUS

The Standard Model of particle physics, first formulated by Glashow, Salam and Weinberg in the 1970s [2, 3], is widely considered one of the most successful theories in physics. Using the language of quantum field theory it describes the behaviour of the matter particles and the forces between them. All numerical measurements performed so far are in agreement with the model's predictions. Open questions remain however, as the theory does not provide a basis for dark matter nor dark energy and attempts to find a valid quantum field theoretic description of gravity have failed so far.

In the last couple of decades, theoretical developments have revived the old idea of extra dimensions. One model referred to as the Randall Sundrum model could join the Standard Model with gravity and resolve a long standing theoretical issue known as the "*hierarchy problem*".

2.1 The Standard Model

There are four known forces of nature: electromagnetic, weak, strong, and gravitation. The Standard Model provides a predictive description based on quantum field theory of the fundamental matter particles, (spin 1/2 "*fermions*"), and of three of these forces (in terms of force carrying integer spin "*bosons*"). These particles are illustrated in Table 2.1. Each particle is described by a separate field in quantum field theory; excitations of a field give rise to particles. The matter and force fields are coupled, allowing interactions to take place.

The structure of the theory is required to be invariant when transformed by elements from the group $SU(3) \otimes SU(2) \otimes U(1)$ and the space-time symmetries of the Poincaré group

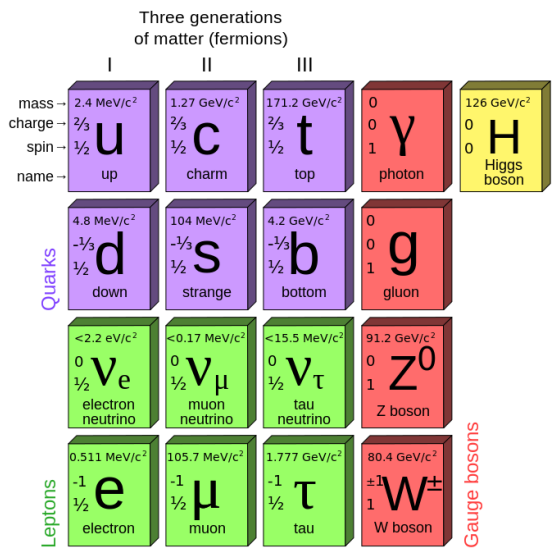

Table 2.1: Generations of matter in the Standard Model, derived from [4].

in order to provide Lorentz invariance and conserve quantum numbers which cannot be created or destroyed globally. The symmetry constraint requires the existence of the bosons which mediate the interactions. Each component of the group expression resp-resents a different force: $\mathrm{SU}(3)$ describes the strong force and $\mathrm{SU}(2) \otimes \mathrm{SU}(1)$ describe the mixing of two fields which give rise to electroweak interactions. These groups have a structure which produces the number of force carriers in each field.

The symmetry requirement also demands that the bosons be massless, which they are not. The solution to this problem is the Higgs mechanism which breaks this symmetry in a way which retains all of the nice properties of the Standard Model. This symmetry breaking called “spontaneous symmetry breaking” is achieved by the introduction of a complex doublet of scalar fields, collectively referred to as “the Higgs field”. After the symmetry breaking, the field has a non-zero vacuum expectation value. Three of the

components of the Higgs field mix with the boson fields and results in them acquiring mass. The remaining component becomes the Higgs particle. The existence of the Higgs particle has recently been verified by ATLAS and CMS at the LHC.

The Standard Model contains three generations of fermions. Each generation consists of two quarks: "*up-type*", with particles of electric charge $+\frac{2}{3}$ and "*down-type*" with charge $-\frac{1}{3}$. In addition, there is an electron-like fermion, and a neutral neutrino. Each of these particles has an anti-particle which is a charge-parity conjugate of its partner.

As discussed above, the forces between the fermions are mediated by the force propagators, called bosons. The electromagnetic force is propagated by the photon (denoted γ), the electroweak has a Z^0 and a $W^{\pm}$, and the strong force has the gluon (denoted g). The strong force has a type of charge analogous to electric charge referred to as "*colour*". In contrast to the electric force, the strength of the strong force does not decrease with increasing separation between two colour charges. This is due to the gluon self coupling, which arises because they carry two colour charges. If two quarks become sufficiently separated, the potential energy in the field becomes great enough for pair-production. This results in a phenomenon known as "*colour confinement*": the fact that individual quarks cannot be observed in nature. Despite having a self-coupling, the weak force does not exhibit confinement due to the mass of the bosons which limit the range of the force and decrease its strength at low energies. Multiple quarks form composite states called hadrons: in pairs of two they are called mesons; baryons contain three quarks. Colour confinement manifests itself at a particle collider as hadronization: the process whereby initial-state quarks become a shower of colour-neutral hadrons.

Protons are baryons, consisting of the quarks uud. In addition to these "*valence*" quarks,

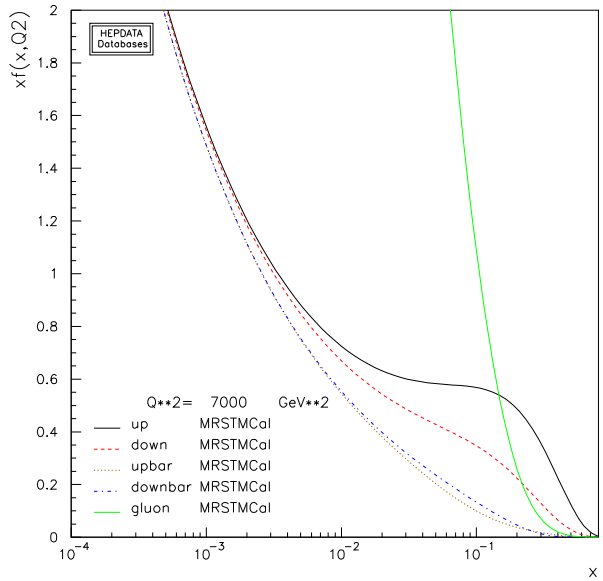

Figure 2.1: `MRSTMCal` [8] parton density functions of the up quark, down quark, their anti-particles and gluons at an energy scale of $Q^2 = 7\,\text{TeV}$ as a function of the longitudinal momentum fraction, x. Generated using the Durham HepData site [10].

protons contain additional particles arising from quantum fluctuations which are referred to as "*sea*" quarks. Collectively, these are referred to as partons. The parton structure of protons is described by parton density functions (PDFs). The PDFs are measured through global analysis of scattering data from electron-proton experiments such as ZEUS at HERA [5, 6]. Information gleaned from these experiments are assembled by various collaborations, such as CTEQ [7] and MRST [8, 9]. Figure 2.1 shows the predicted behaviour of the PDFs at an energy scale of 7 TeV as a function of the longitudinal momentum fraction, x, defined as the fraction of the incoming proton's longitudinal momentum that the resulting partons have after the interaction.

2.2 Theoretical issues with the Standard Model

There is strong theoretical motivation for the existence of new physics beyond the Standard Model. One obvious deficiency is that gravity is not described at all within it. There is no natural explanation which fits within the model as to why gravity is so many orders of magnitude weaker than the other forces. This is related to the so-called hierarchy problem: the energy scale at which gravity is thought to be important in particle interactions is the Planck scale, which is $\mathcal{O}\left(10^{19}\,\text{GeV}\right)$; contrasted with the electro-weak scale $\mathcal{O}\left(100\,\text{GeV}\right)$, making gravity an exceedingly weak fundamental force.

The Standard Model provides no basis for determining a number of aspects of its structure from first principles, including the number of generations of matter and a large number of parameters. These must be measured and fed as input into the model. It would be preferable to have a model which requires fewer inputs to come from measurement. In addition, the model cannot be adapted in a straightforward way to include gravity.

Whilst the Standard Model is very successful in the regions of phase space which it was built to describe, there are still aesthetic problems that many theorists believe may point to a deeper underlying structure which is so far undiscovered. If the Standard Model as it stands today is correct and the newly discovered Higgs particle turns out to agree with the predicted cross-sections and couplings with high precision, it is thought that the model must describe all physical interactions all the way up to the Planck scale before it breaks down in the face of quantum gravity. This means that there is a very large region of parameter space in which nothing new happens. This is referred to as the particle "*desert*". It also means that there must be some property of TeV energy scales which makes them

special. The large disparity between the electroweak scales and the Planck scale serve as the driver for attempts to go beyond the Standard Model, including supersymmetry, technicolour and extra-dimensional models [11].

Quantum loop corrections to the effective Higgs mass diverge, making it tend towards the Planck mass unless a cutoff scale (Λ) is employed above which the theory is unable to make predictions. In order to take Λ up to the Planck scale, there must exist an almost perfect cancellation of two large terms in order to have a stable model (so-called "*fine tuning*"). Such a coincidence is not a desirable property for a model to have. Another possible solution is to introduce additional spatial dimensions. This can provide a solution to the hierarchy problem, explaining the weakness of gravity naturally through the geometric structure of the model.

2.3 Extra dimensions

Models with extra dimensions can potentially explain the weakness of gravity without having to resort to fine tuning. Instead of arranging the model so that corrections to the Higgs mass cancel perfectly, the true value of the Planck mass, M^*_{pl}, is close to the electroweak scale. The apparent high value we measure (through the effect it has on the strength of gravity) is a side effect of the unobserved additional dimensions. In these models, extra spatial dimensions exist into which some particles are allowed to propagate, but not others.

Extra dimension models use the machinery of General Relativity to describe the behaviour of the gravitational interaction. The apparent weakness of the force of gravity

can be understood in terms of the graviton, gravity's force carrier, travelling through the extra dimensions. This causes the strength of gravity to be diluted from the perspective of our familiar three dimensions. This geometric solution gives a natural theory without the need for fine tuning.

In order to have a realistic theory, it is necessary to explain why we do not experience these extra dimensions in everyday physics. This could be because only gravitons are allowed to propagate through them, and/or the additional dimensions are wrapped up (compactified) to such small lengths that they are not experienced at everyday scales.

Models with compactified extra dimensions predict new resonances. These resonances arise because the wave function in the additional dimension must return to its starting point with the same phase, otherwise destructive interference will occur. It has a wavelength λ which is a multiple of $2\pi R$ where R is the radius of the compactified dimension; these discrete wavelengths correspond to discrete momenta ($p_{\mathrm{ED}} = \frac{2\pi}{\lambda}$). A massless particle propagating in four spatial dimensions satisfies Einstein's equation relating energy E and momentum p, with an additional component of momentum in the extra dimension, p_{ED}:

$$E^2 - p_x^2 - p_y^2 - p_z^2 - p_{\mathrm{ED}}^2 = 0.$$

Since the wave function must be cyclical along the axis of the additional dimension (all other solutions cancel when integrated), the amplitude must be the same after one turn:

$$\mathrm{e}^{\mathrm{i}p_{\mathrm{ED}}\cdot x} = \mathrm{e}^{\mathrm{i}p_{\mathrm{ED}}\cdot(x+2\pi R)} = \mathrm{e}^{ip_{\mathrm{ED}}\cdot x}\underbrace{\mathrm{e}^{ip_{\mathrm{ED}}2\pi R}}_{=1},$$

which entails:

$$p_{\mathrm{ED}} 2\pi R = n 2\pi \qquad \Rightarrow \qquad p_{\mathrm{ED}} = \frac{n}{R}.$$

Therefore:

$$E^2 - p_x^2 - p_y^2 - p_z^2 = \frac{n^2}{R^2}.$$

The term on the right hand side can be interpreted as a mass (squared) from our three spatial dimensional perspective where p_{ED} cannot be observed. Thus, these extra dimensional theories predict a spectrum of resonances, one for each value of n, a so-called "*Kaluza Klein Tower*". Such a tower should exist for any particle which can propagate through the compactified dimension.

2.4 The Randall Sundrum model

The Randall-Sundrum (RS) model [12, 13] predicts a Kaluza Klein Tower, which arises through a mechanism different from the compactified dimensions discussed above. In this model, our familiar 3(+1) dimensions are a slice, referred to as "*The TeV brane*", embedded within a higher-dimensional universe, called "*the bulk*", depicted in figure 2.2. Within the bulk there exists another brane, called the Planck brane. The Planck brane is massive compared with our own, and it warps the space between the two. This warping of space behaves like a potential well, trapping most gravitons close to the Planck brane. The gravitons are effectively in a bound state, giving them a discrete set of energy levels, which appear as Kaluza Klein resonances.

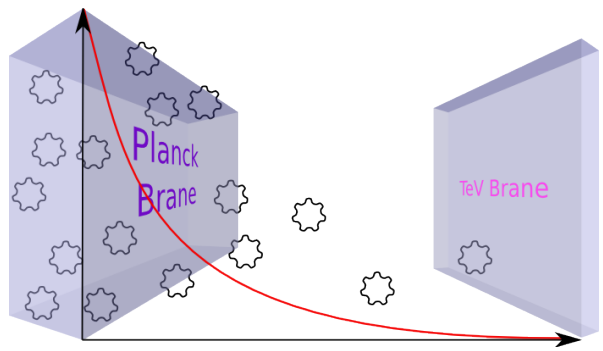

Figure 2.2: A depiction of the RS scenario. The x-axis represents the separation in the extra dimension and the y-axis is the potential, which is exponentially suppressed at the TeV brane due to the warping of space caused by the mass of the Planck brane. As a consequence, gravitons (represented by the circular wave) and the force of gravity tend to be localized away from the TeV brane, making the effective force of gravity appear weak.

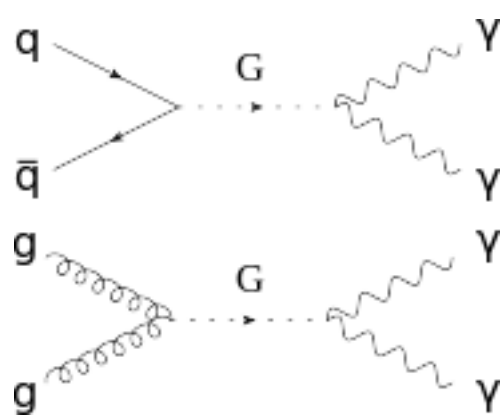

Figure 2.3: Leading order diagrams for $G \to \gamma\gamma$ at the LHC.

The theory introduces a warped metric [14]:

$$ds^2 = \mathrm{e}^{-2kr_c\phi}\eta_{\mu\nu}dx^\mu dx^\nu + r_c^2 d\phi^2,$$

where ϕ is the extra dimensional coordinate such that $0 \leq \phi \leq \pi$ and r_c sets the size, where $r_c\pi$ is the separation of the Planck and TeV branes. The degree of geometric warping is characterized by the geometric curvature, k. The exponential factor is called the "warp factor" and causes length and mass scales to vary as a function of the coordinate, ϕ, making the geometry non-factorizable. In particular, mass and energy are scales are made exponentially smaller when moving from the Planck to the TeV brane. The degree of warping of the extra dimensions can be chosen such that the real Planck mass is brought down to the TeV scale at the TeV brane, solving the hierarchy problem.

Just as in classical gravity, where the strength of the gravitational coupling is $\propto \sqrt{G} \propto 1/M_{\mathrm{pl}}^2$. In the Randall Sundrum model, the coupling will be proportional to $1/\overline{M_{\mathrm{pl}}}$ where $\overline{M_{\mathrm{pl}}}$ is the reduced Planck mass. The model has two free parameters, the mass of the lowest mass resonance (m_G) and the ratio of curvature to the reduced Planck mass ($k/\overline{M_{\mathrm{pl}}}$), which determines the coupling strength and hence the cross-sections of the resonances.

The leading order processes involving gravitons which could be observed at the LHC are shown in figure 2.3. Gravitons are produced in s-channel quark-antiquark annihilation or gluon-gluon fusion. They would appear in the detector through their decays into $f\overline{f}$, $\gamma\gamma$, gg, ZZ, W^+W^-, *etc.*, as narrow resonances in the final state mass spectrum. The widths of the resonances are related to the magnitude of the coupling strength, smaller coupling strengths giving narrower resonances. The widths Γ_G would range between 100 MeV to a few GeV. These resonances would be relatively straightforward to detect at

ATLAS, because the Standard Model background at these high masses is expected to be small.

It is worth mentioning that in addition to the above processes, there exist other extra-dimension models with different signals which may be accessible to a collider experiment such as ATLAS. For example, [15] describes a theory where the graviton can radiate into the extra dimension, giving rise to a strong missing energy signature. Another example is the scenario described by Arkani-Hamed, Dimopoulos and Dvali (ADD) [11]. Such models are outside the scope of this thesis.

2.5 Randall Sundrum branching ratio and cross-section

It is a feature of the Randall Sundrum model that the coupling of the Graviton to other particles is "universal". This means that branching ratios are solely determined by the spin (and possibly threshold effects for massive particles). The branching ratios of gravitons decaying to different processes are shown in figure 2.4. They are almost constant as a function of mass at high mass. The gg channel dominates at all masses because there are 8 types of gluon, however it is an experimentally unfavourable channel due to the large dijet background. The $\gamma\gamma$ channel has a lower branching fraction than the Z^0 or the $W^{\pm}$ but presents an easier search experimentally, requiring fewer particles to be correctly reconstructed. In addition, the branching fraction for the $\gamma\gamma$ channel is double that of the dilepton channel and therefore the $\gamma\gamma$ channel is more sensitive. The potential for a graviton to decay to the $\gamma\gamma$ channel can also distinguish it from a Z' decay. The Z' is a heavier version of the spin-1 Z^0 boson which is predicted in several extensions to the

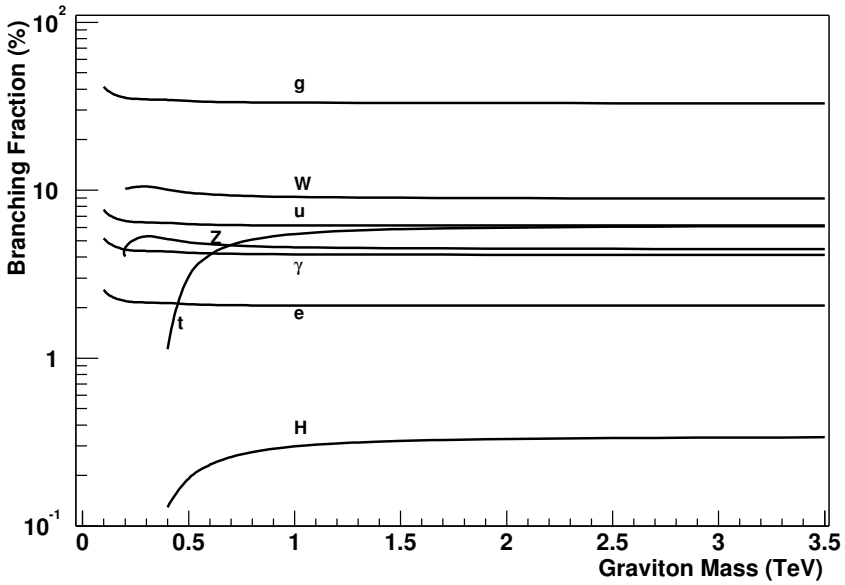

Figure 2.4: Branching ratios for particle pair-production as a function of m_G for various particles, from [19]. The $\mu^+\mu^-$ channel has the same branching fraction as e^+e^-, labelled "e".

Standard Model [16].

Figure 2.5 shows the invariant mass distribution for diphoton decays of example graviton resonances at different masses superimposed on the estimated Standard Model background contribution derived in chapter 8. The cross-section times branching ratio of the signal is shown in figure 2.6. The RS cross-section is determined using PYTHIA 8 [17], with a Next-to-Leading Order k-factor of 1.75 ± 0.1 which is provided by the authors of [18].

2.5.1 Angular distributions

Uniquely amongst the force-mediating gauge bosons, the graviton is not a spin-1 vector boson but a spin-2 tensor boson. These spins give rise to different angular distributions

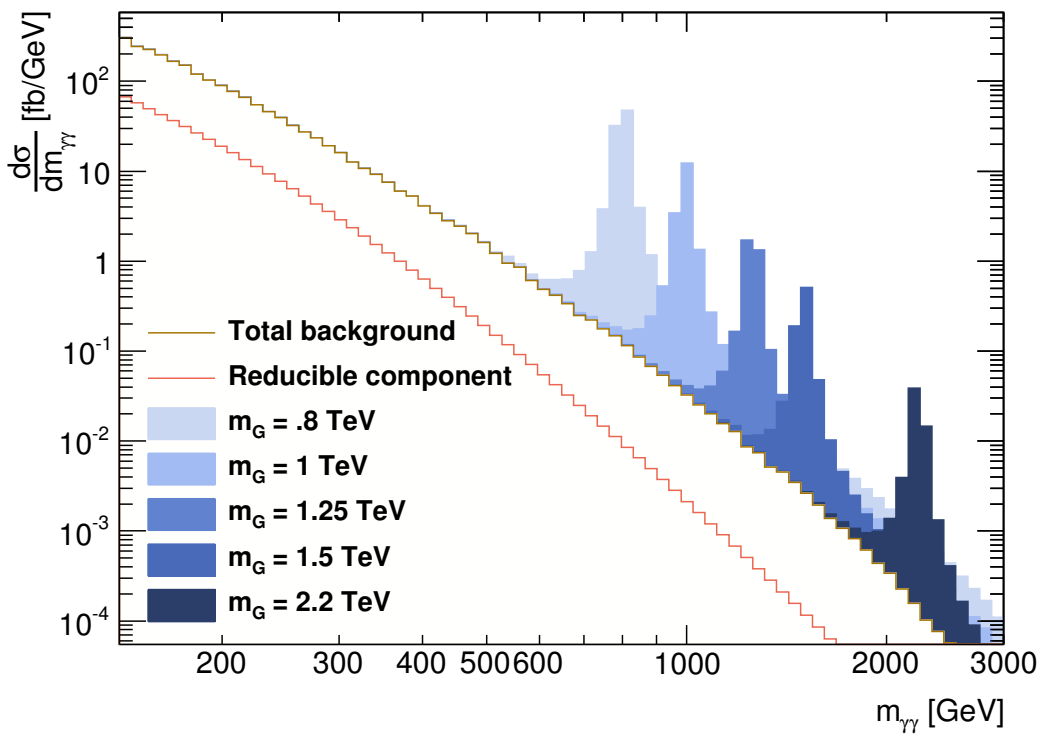

Figure 2.5: Differential cross-section in $m_{\gamma\gamma}$ showing the total background along with the reducible component distribution and graviton resonances with $k/\overline{M_{\mathrm{pl}}}$ at different masses.

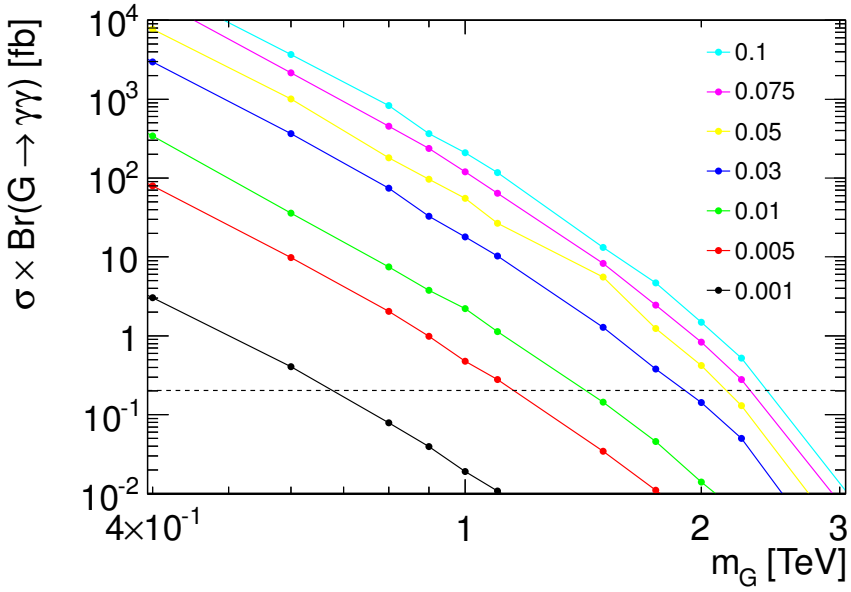

Figure 2.6: PYTHIA 8 cross-section times branching ratio prediction for $G \to \gamma\gamma$ at $\sqrt{s} = 7\,\text{TeV}$ as a function of mass for different values of $k/\overline{M}_{\text{pl}}$, with an NLO k-factor of 1.75 applied. The horizontal dashed line shows the cross-section for which one event would be expected to occur at a luminosity of $4.9\,\text{fb}^{-1}$.

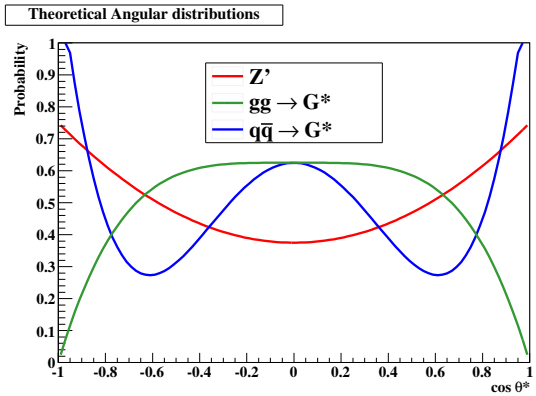

Figure 2.7: Theoretical angular distributions for the G and Z' decaying to e^+e^-.

in the final state, which can be used to distinguish between the two types of bosons. The observed angular distribution depends on the spins of the interacting particles, the resonance itself, and the final state particles. In figure 2.7 and table 2.2, the angular distributions of the final state are shown in the rest frame of the resonance for graviton and Z' production for different initial states. As can be seen, the angular distribution of the Z' is significantly different from those of the graviton and the isotropically decaying Higgs. However it should be noted that for a given final state, the angular distribution for the graviton resonance will be a mixture of those arising from gg fusion and $q\overline{q}$ annihilation, a fact that it may be possible to exploit to differentiate between different current and possible future theoretical models which predict resonances, if a such a resonance is ever discovered.

Process	Distribution
$q\overline{q} \to Z' \to e^+e^-$	$\frac{3}{8}\left(1+\cos^2\theta^*\right)$
$q\overline{q} \to G \to e^+e^-$	$\frac{5}{8}\left(1-3\cos^2\theta^*+4\cos^4\theta^*\right)$
$gg \to G \to e^+e^-$	$\frac{5}{8}\left(1-\cos^4\theta^*\right)$
$gg \to G \to \gamma\gamma$	$\frac{1}{4}+\frac{3}{2}\cos^2\theta^*+\frac{1}{4}\cos^4\theta^*$
$H \to \gamma\gamma$ (spin 0)	Isotropic

Table 2.2: Functional forms of the angular distributions of graviton, Z' and H decay [20]. θ^* is the separation angle in the rest frame of the final state two-particle system.

2.6 Searching for new physics at a hadron collider

The RS model predicts the rate at which diphoton pairs should be produced for a region of phase space. If the model is true and the universe has chosen parameters which are favourable, it may be possible to measure an excess of diphoton candidates (the signal) compared with the expectation for the Standard Model alone (the background). In order to do that, it is necessary to fully understand the ways in which diphoton candidates can arise from the Standard Model.

In a world not limited by budget or resources, the ideal experiment for new physics searches would involve colliding together individual fundamental particles with quantum numbers chosen by the experimenter. The power loss due to Bremsstrahlung radiation limits the maximum energy a synchrotron can achieve. This effect is proportional to the fourth power of the mass of the particles under acceleration and inversely proportional to the square of the radius of the accelerator. Since building a tunnel to host an accelerator is expensive and currently impractical, higher collision energies can only be achieved by using heavier particles, such as protons.

Protons are experimentally disadvantageous compared to leptons because they are

composite particles; the underlying quark collisions and the subsequent colour interactions are more complex than lepton collisions. This results in a large number of strong interactions producing multiple jets. In addition, the experimenter cannot choose the centre of mass collision energy as with a lepton collider, instead collisions occur at all kinematically accessible energies and the invariant mass of a collision must be reconstructed by measuring the four-momentum of the hard collision products.

Estimating the background shape and normalization is one of the challenges for such an analysis. Background events lie in two categories: the *"reducible"*, those which are distinguishable in principle through detector selection; and *"irreducible"*, for which the final state of the event looks identical to the signal of interest.

2.6.1 Diphotons with the Standard Model

Before a search for beyond Standard Model physics can take place, it is first essential to estimate the rate of diphoton production in the Standard Model. Figure 2.8 shows production diagrams for Standard Model hard diphoton production contributing to the irreducible background. In addition to the processes shown in a)-c), figures d) and e) (jet fragmentation) are also considered to be a part of the irreducible background because of their ability to produce hard photons. DIPHOX [21] is a state of the art Monte Carlo generator which is able to provide predictions in the differential cross-section as a function of the diphoton invariant mass at next-to-leading order (NLO). It is used in this analysis for the Standard Model diphoton mass distribution shape since the NLO calculation is not available in the more general generators such as PYTHIA. It has been measured to predict the shape of the background distribution reasonably well out to the high mass region

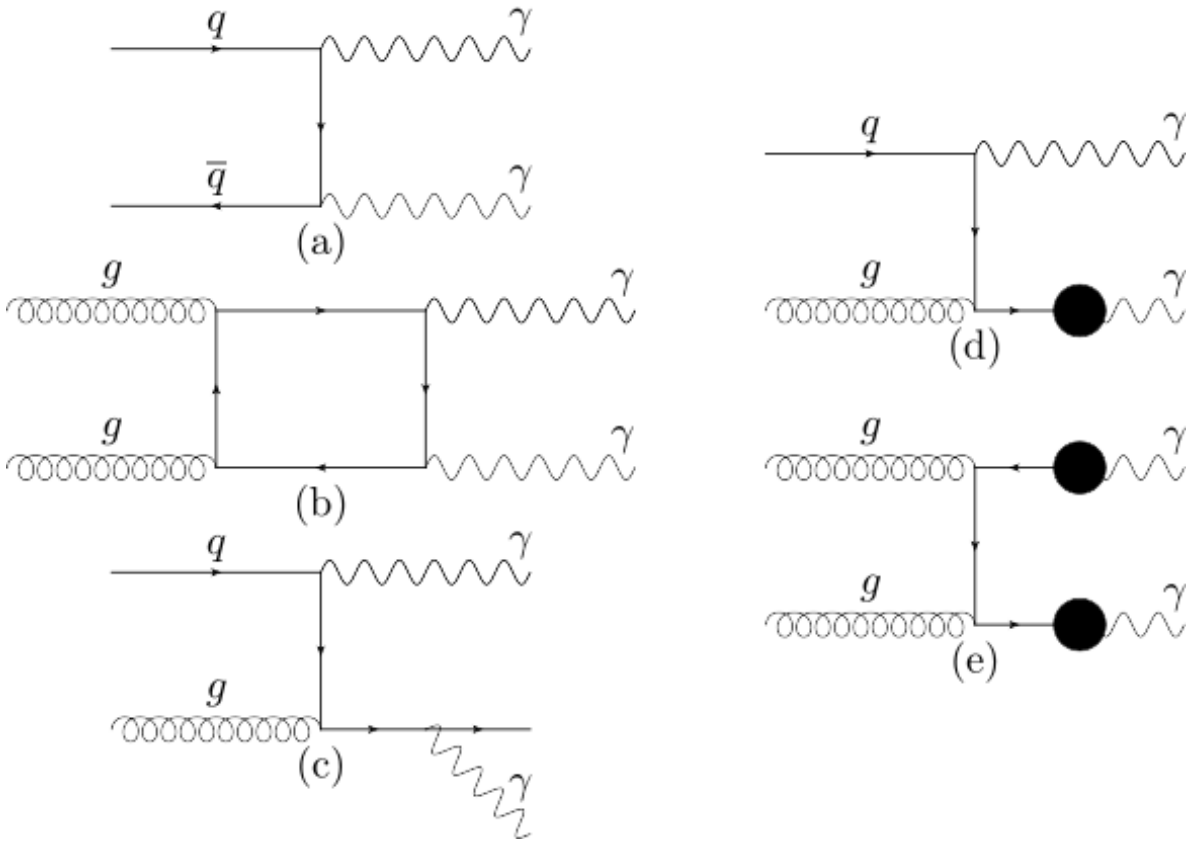

Figure 2.8: Production diagrams for Standard Model $\gamma\gamma$ production, representing the irreducible background to this analysis. (a) "Born", $\mathcal{O}\left(\alpha^2\right)$ (b) "Box process" $\mathcal{O}\left(\alpha^2\alpha_s^2\right)$ (c) "Quark Bremsstrahlung" $\mathcal{O}\left(\alpha^2\alpha_s\right)$, (d, e) Jet fragmentation processes included in the irreducible background.

which is used in this analysis [22]. It is used in section 8.1.1 to obtain the shape of the irreducible background in the $m_{\gamma\gamma}$ distribution.

In addition to the irreducible background, it is necessary to consider high energy γ+Jet events where the jet contains a high energy $\pi^0 \to \gamma\gamma$ decay where the $\gamma\gamma$ has a small angular separation which can produce a single γ-like signal in the detector. An example γ+Jet event is shown in figure 2.9. The impact on this analysis of these events is discussed in detail in section 6.1. The rate at which jet events produce a γ-like signal is small, but the jet rate is high. These events represent a challenge for simulation since they require very large amounts of CPU-expensive detector simulation and the Monte Carlo predictions are known to be unreliable.

2.7 Existing constraints

Figure 2.10 shows the state of the Randall Sundrum parameter space constraints before the start-up of the LHC. The model is constrained into a triangular shaped region, bounded by the ($\int \mathscr{L} = 5.4\,\mathrm{fb}^{-1}$) Tevatron measurements on the left and theoretical stability considerations on the top, bottom and right. The LHC will eventually explore all of the allowed region. As more data is collected without sign of a discovery, the exclusion frontier will move from left to right, until it ultimately reaches the line marked "LHC" when $\mathscr{O}\left(100\,\mathrm{fb}^{-1}\right)$ is obtained.

There is currently no evidence for a high-mass resonance at existing experiments. For lower values of the coupling (~ 0.01), measurements at the Tevatron have excluded graviton masses $\lesssim 600\,\mathrm{GeV}$. For higher values ($\sim 0.1$) the excluded region lies below

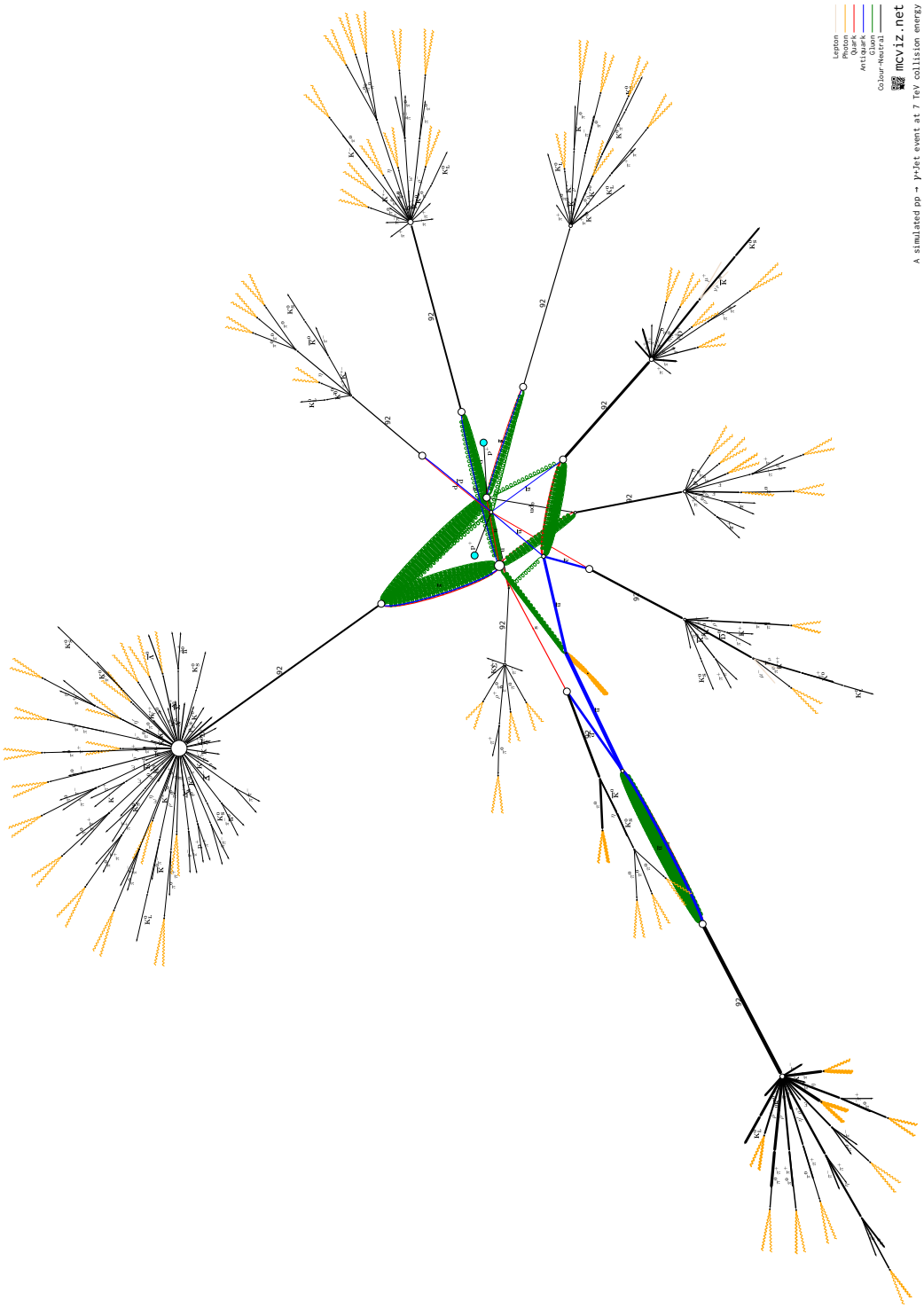

Figure 2.9: A topological depiction of a PYTHIA 6 γ + Jet event at $\sqrt{s} = 500\,\text{GeV}$, generated with MCVIZ [23]. Lines represent particles with the line width in proportion to $\ln p_T$ of that particle.

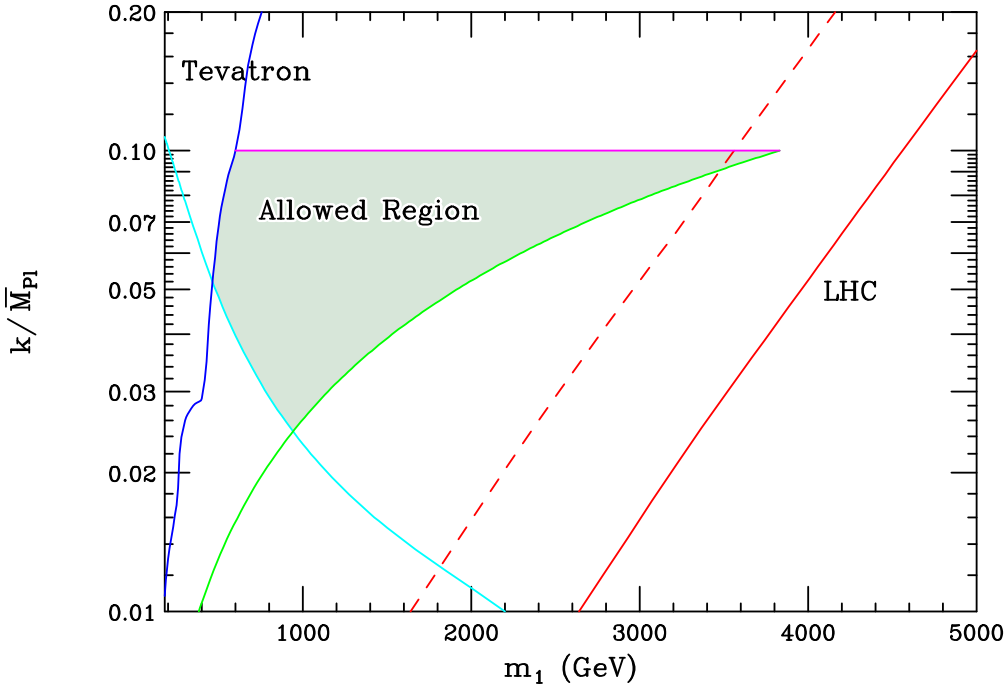

Figure 2.10: Constraints on the stability of the Randall-Sundrum model [13, 24]. The left region shows the previous Tevatron limit, the line on the right shows the expected reach after the 10 fb^{-1} (dashed) and 100 fb^{-1} (solid).

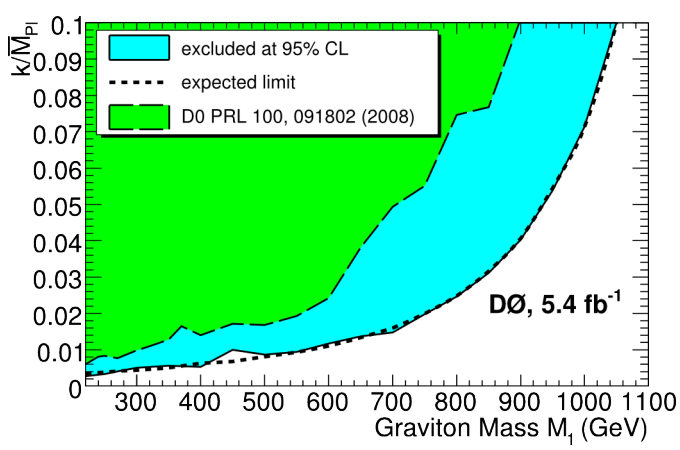

Figure 2.11: Latest limit from DØ [25], which is similar to the limit from CDF [26].

$\lesssim 1050\,\text{GeV}$, see figure 2.11. Previous studies have shown that the LHC should be sensitive to gravitons with masses up to $2.5 - 5\,\text{TeV}$ with $100\,\text{fb}^{-1}$, depending on the coupling strength [27]. This thesis presents in chapter 11 the same measurement as in figure 2.11 using 2011 LHC data.

Chapter 3

Experimental Apparatus

In terms of the distances between the last control elements of the LHC and the collision point, it's a bit like firing knitting needles from across the Atlantic and getting them to collide half way.

JAMES GILLIES

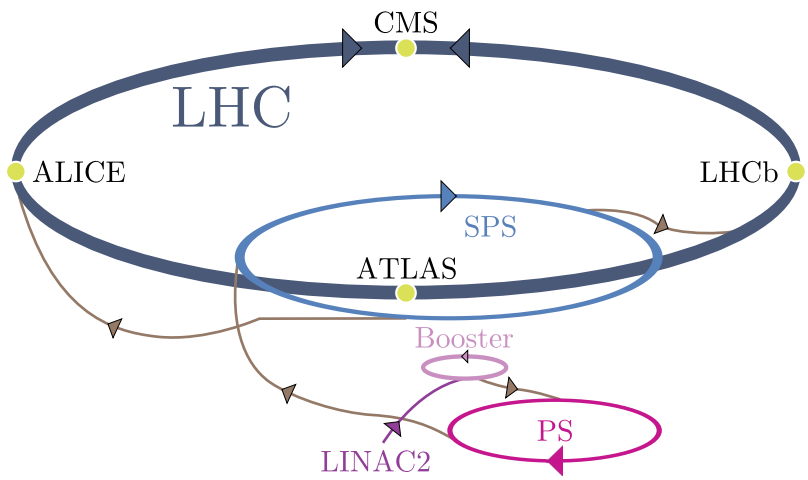

Figure 3.1: A schematic showing the parts of the CERN complex used to accelerate protons. The arrows indicate the direction of proton travel; also shown are the transfer lines in brown. The LHC is designed to accept hadrons at the Super Proton Synchrotron's (SPS) maximum energy of 450 GeV. The Proton Synchrotron (PS), Booster and LINAC2 are used to accelerate protons which are obtained by ionizing hydrogen from a bottle of gas [28]. Also shown are the four large experiments, ATLAS, ALICE, CMS and LHCb.

This chapter describes the experimental set-up at CERN, starting with the Large Hadron Collider (LHC) in section 3.1. The ATLAS detector and its larger components are described in section 3.2 and the process of triggering on interesting events and collecting the data are described in section 3.3 and section 3.4 respectively.

3.1 The Large Hadron Collider

The LHC [28] is currently the world's highest energy particle collider. It is built to create and allow the study of interactions between particles similar to those which occurred in the first seconds of the universe's existence. It is located at the end of a chain of accelerators, shown in figure 3.1, and forms a 27 km circle which crosses the French-Swiss

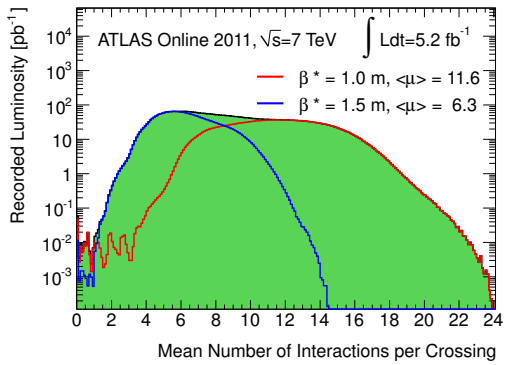

Figure 3.2: The luminosity-weighted Poisson mean number of interactions per bunch crossing $\langle\mu\rangle$ during 2011 [33, 34].

border. The LHC is designed to accelerate "*hadrons*": protons or heavy ions. Heavy-ion collisions happen during special runs of the accelerator; only proton collisions will be discussed in this thesis.

Protons begin life in as hydrogen in a gas bottle, after which they are stripped of their electrons by an electric field. They are accelerated thereafter by a linear accelerator and injected into a series of synchrotrons of increasing size where they are accelerated by radio-frequency cavities. The LHC accepts protons at an initial energy of 450 GeV and accelerates them up to a design maximum of 7 TeV. The centre of mass (COM) collision energy is double that of the individual beam energies; the LHC is designed for a COM energy of 14 TeV, although for the data collected which is used in this thesis the COM energy is only 7 TeV. Collisions are observed by four independent experiments at different points around the ring: ATLAS [29], ALICE [30], CMS [31] and LHCb [32].

3.1.1 Luminosity

There are two beam-related quantities of particular importance for every experimentalist at a particle collider: the COM energy (denoted $\sqrt{s}$), and the instantaneous luminosity ($\mathscr{L}$) integrated over the lifetime of the experiment ($L = \int \mathscr{L}\,\mathrm{d}t$). They directly influence the ability to observe rare physics events which have a small cross-section. The number of events for a physical process (N) which occur at a collider is given by:

$$N = \sigma L$$

where σ, the cross-section of that process, has dimensions of area. The number of detected events is $N_{\text{detected}} = \epsilon N$ where ϵ is the efficiency times acceptance of the detector. For proton collisions, the LHC is designed to produce maximum instantaneous luminosity of $\mathscr{L} = 10^{34}\,\mathrm{cm}^{-2}\mathrm{s}^{-1}$. The total proton cross-section at the LHC is measured by the TOTEM collaboration to be 98 mb at $\sqrt{s} = 7\,\mathrm{TeV}$ [35], which implies an approximate interaction rate of $\mathscr{O}\,(1\,\mathrm{GHz})$.

Protons circulate the LHC in groups of $\mathscr{O}\left(10^{11}\right)$ protons, called "*bunches*". A bunch has a cross-sectional area $\mathscr{O}\left(\mu\mathrm{m}^2\right)$ and length $\mathscr{O}\,(c \times 1\,\mathrm{ns})$. Bunches are confined into a small volume and brought into collision in the centre of ATLAS once every 50 ns. The high luminosity causes multiple proton interactions per bunch crossing. This is referred to as "*pile-up*"; multiple collisions occur during one bunch crossing. The mean number of simultaneous interactions per bunch crossing ($\langle\mu\rangle$) is shown in figure 3.2. Pile-up events represent an experimental challenge because they entail a high detector occupancy, making it hard for reconstruction software to correctly identify particles.

3.2 The ATLAS experiment

ATLAS*, shown in figure 3.3, is a general purpose particle detector situated on the LHC ring [29]. Encompassing a beryllium beam-pipe and centred on the nominal interaction region, it is approximately 50 m long and 20 m in diameter. It follows a common design pattern for particle detectors, with independent sub-detectors arranged concentrically in layered formation about the beam pipe. Solenoid and toroid magnets create a field throughout the detector which causes charged particles to deflect in inverse proportion to their momentum.

Positions within the detector are globally specified with a right-handed Cartesian coordinate system with the origin at the centre of the detector. The x-axis points towards the centre of the LHC, the y-axis upwards, the z-axis anticlockwise along the beamline as viewed from above. The polar angle (θ) is the angle from the positive z-axis and the azimuthal (ϕ) angle is measured anticlockwise from the positive x-axis. The pseudo-rapidity $\eta = -\ln\tan(\theta/2)$ is often used for its convenience†. The transverse component of momentum is $p_{\mathrm{T}} = \sqrt{p^2 - p_{\mathrm{z}}^2}$ where p^2 is the square of the magnitude of the momentum and p_{z} the z-component. The transverse energy (also the energy deposited in a calorimeter element) $E_{\mathrm{T}} = E/\cosh\eta$ is equal to the p_{T} for photons. Radial distances in the transverse plane are calculated as $r = \sqrt{x^2 + y^2}$. Distances in angular space are labelled $\Delta R = \sqrt{\Delta\eta^2 + \Delta\phi^2}$.

In order of increasing r, the detector's components are: the Inner Detector (ID; dis-

*ATLAS (A Toroidal LHC ApparatuS) gets its name from its toroidal geometry

†This is owing to the fact it is invariant under Lorentz transformations, and approximately the same number of particles will decay into a given region in fixed $\Delta\eta$; a fact the detector is designed to exploit.

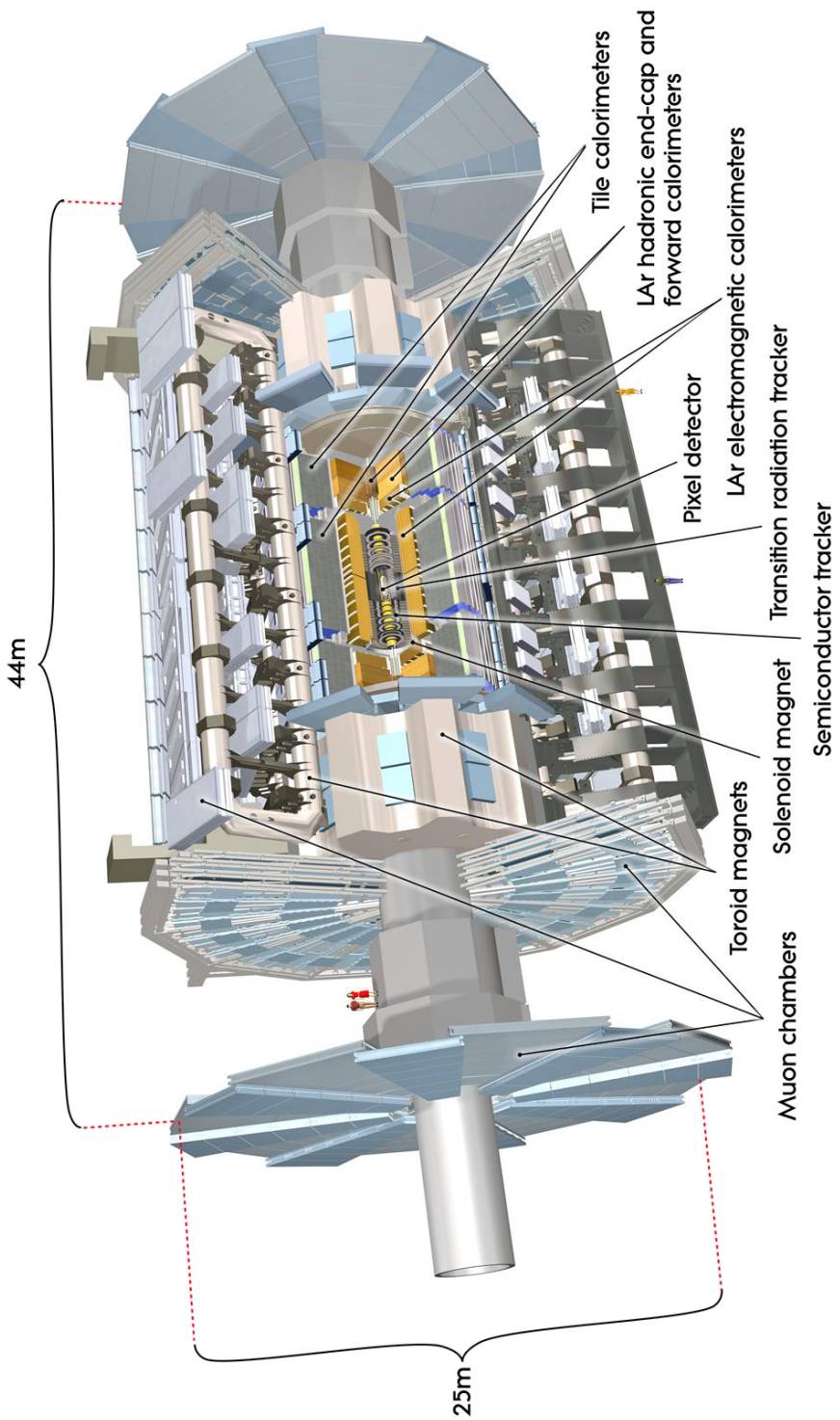

Figure 3.3: A cutaway view of the ATLAS detector with the proton beam axis going left to right and the interaction region in the centre. The liquid argon calorimeter is shown in orange near the centre, surrounded by the Tile calorimeter immediately outside of it. The end-cap toroid magnets are along the beam line from the interaction region, followed by the muon wheels on the far left and right. At the outermost of the detector are the muon chambers with the barrel toroid. It is described in more detail in [29].

cussed in section 3.2.2), the solenoid (section 3.2.1), calorimetry (section 3.2.3); segmented into the electromagnetic calorimeter (ECal) and the hadronic calorimeter (HCal), and the Muon Spectrometer (section 3.2.4) along with the toroid magnets (section 3.2.1).

3.2.1 Magnets

The trajectory of charged particles is curved in proportion to the strength of a magnetic field. ATLAS has two cold superconducting magnet systems consisting of one solenoid and three toroids (a barrel and two end-caps), shown in figure 3.4.

Solenoid

The solenoid magnet provides a 2 T magnetic field within the Inner Detector region, aligned with the beam axis. This bends tracks of charged particles and is used in conjunction with the Inner Detector to identify the polarity and measure the transverse momentum. Its design is optimized to minimize the amount of material it presents in front of the calorimeter, which is approximately 0.7 radiation lengths for perpendicular incidence [29].

Toroid

The toroid magnet creates a field of approximately 0.5 T in the barrel and 1 T in the end-caps, which is used to bend muons trajectories in proportion to their p_{T} as they traverse the muon spectrometer.

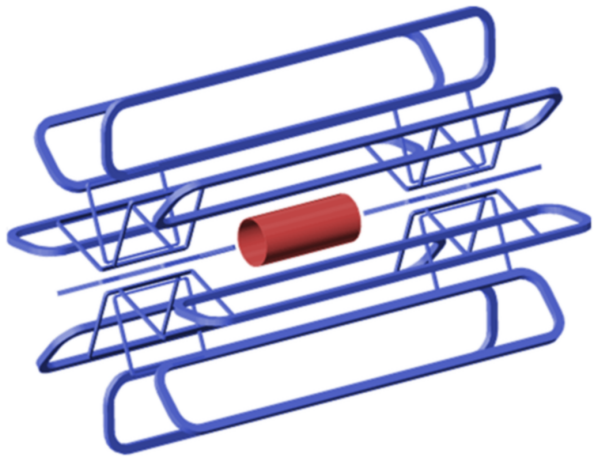

Figure 3.4: The geometry of the superconducting toroid (blue) and solenoid (red) magnets, used to deflect charged particles as they traverse the detector [29].

3.2.2 The Inner Detector and particle tracking

The Inner Detector, outlined in figure 3.5 and described in detail in [29, §4], consists of the Pixel Detector, SemiConductor Tracker (SCT) and Transition Radiation Tracker (TRT). Each of these systems measure positions in space ("*space-points*") when charged particles traverse them. From these points it is possible to algorithmically determine the particle's trajectory. It is designed to obtain the position of collisions (the primary vertex) and any subsequent decays, which create distinct secondary vertices. To obtain a high precision on the measurement of a particle's trajectory and vertex it is necessary to start tracking particles as close to the beam as possible.

The beam-pipe is approximately 6 mm thick and its outer extent is $r = 36$ mm from the beam. The first layer of the pixel detector is at $r = 50.5$ mm. High resolution and granularity are needed closest to the interaction region in order to disambiguate which points belong to which tracks; further away from the interaction point, the granularity

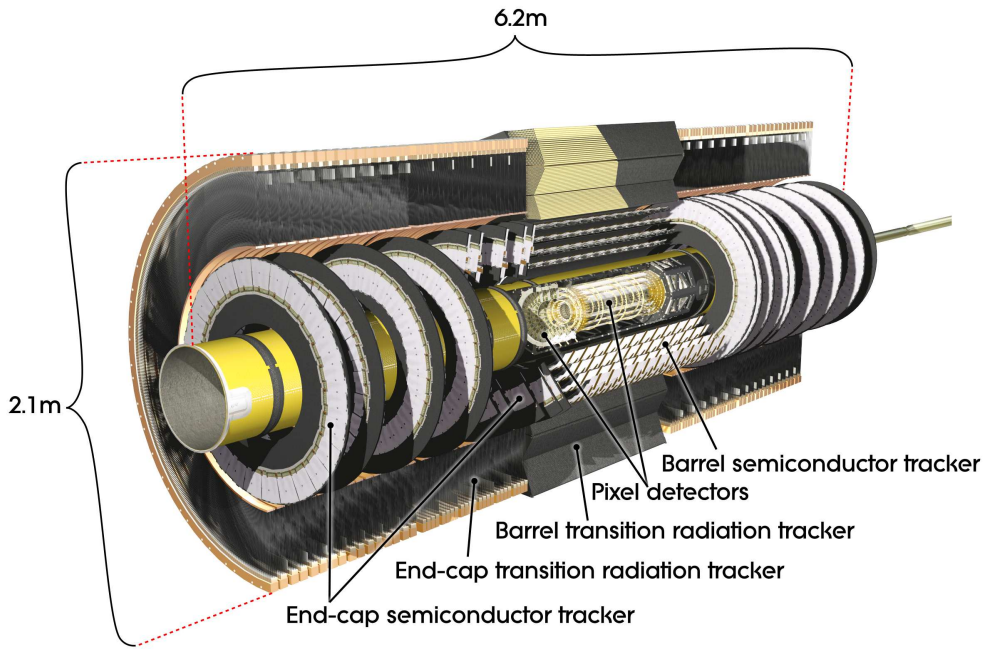

(a) A wide overview with the overall dimensions.

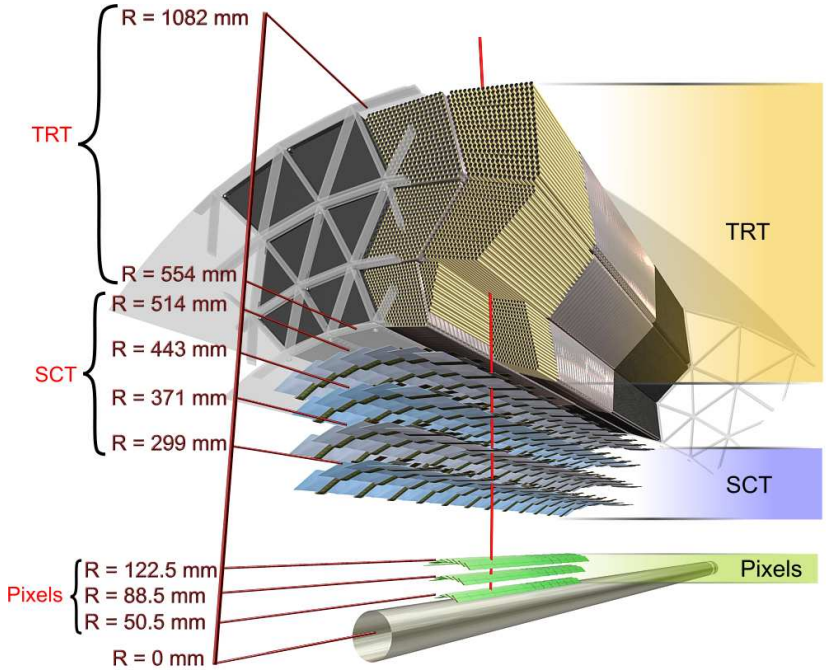

(b) A cross-section of the barrel and the scales of the individual components.

Figure 3.5: Two views of the Inner Detector [29, §4].

is decreased. Each subsystem has a barrel and end-cap portion and is arranged in an overlapping formation to avoid gaps. In the barrel portion, detector elements are arranged concentrically around the beam-pipe and each end-cap region has a number of layers arranged perpendicularly to the beam-pipe in an annulus.

Pixel Detector

The Pixel detector consists of 1,744 identical silicon sensors, with three layers each in the barrel and the end-cap. Each sensor has 46,080 readout channels, with a nominal pixel size of $50 \times 400\,\mu\text{m}^2$. A typical track passes through three sensors, providing a measurement with a resolution of the order $10\,\mu\text{m}$ in $r - \phi$ and $115\,\mu\text{m}$ in z for the barrel; r in the end-cap.

Semiconductor Tracker

The SCT consists of four layers in the barrel and nine layers in each end-cap. They cover a surface area of $63\,\text{m}^2$, providing almost hermetic coverage around the interaction point. The sensors provide at least four space point measurements for tracks passing through. Each module holds a pair of silicon wafers containing strips with a pitch of $80\,\mu\text{m}$ which measure $12\,\text{cm}$ in length. These cover two sides of a plane measuring approximately $12\,\text{cm} \times 6\,\text{cm}$. The strips have a stereo angle of $40\,\text{mrad}$ to enable better resolution of ambiguities which can result from nearby hits in coincidence. The SCT provides a resolution of $17\,\mu\text{m}$ in $r - \phi$ and $580\,\mu\text{m}$ in z (r) for the barrel (end-cap).

Transition Radiation Tracker

A TRT works on the principle that charged particles traversing a material boundary with a $\gamma \gtrsim \mathcal{O}\left(10^3\right)$ will emit soft x-rays with a probability $\mathcal{O}\,(1\%)$. These x-rays ionize a gaseous medium in the presence of an electric field. Liberated electrons drift towards an anode, in turn causing more ionization and eventually a measurable charge accumulates at the anode.

The ATLAS TRT consists of 73 (160) layers in the barrel (end-cap) containing cylindrical straw tubes with a radius of 4 mm which are filled with a gas. The tube wall itself is the cathode and the anode is a wire suspended in the centre; the electric field is provided by a potential difference of $\mathcal{O}\,(1500\,\mathrm{V})$. The straws have a length of 144 cm with an active length of 142.4 cm. An average track will traverse 36 straws. The detector provides a measurement in $r - \phi$ with an accuracy of 130 μm out to $\left|\eta\right| < 2$. Electrons and pions have different probabilities to emit transition radiation, and this detector can provide a good separation of the two particles.

3.2.3 Calorimetry

ATLAS measures particle energies with two separate systems, the Electromagnetic Calorimeter (ECal) and the Hadronic Calorimeter (HCal). They are shown in figure 3.6. In this analysis the ECal is used to measure photons and the HCal is primarily used to reject jets. Hadrons interact minimally in the ECal due to their high mass. Neutral hadrons do not interact with the ECal but are stopped in the HCal. However, neutral mesons may decay to two photons which can be detected in the ECal.

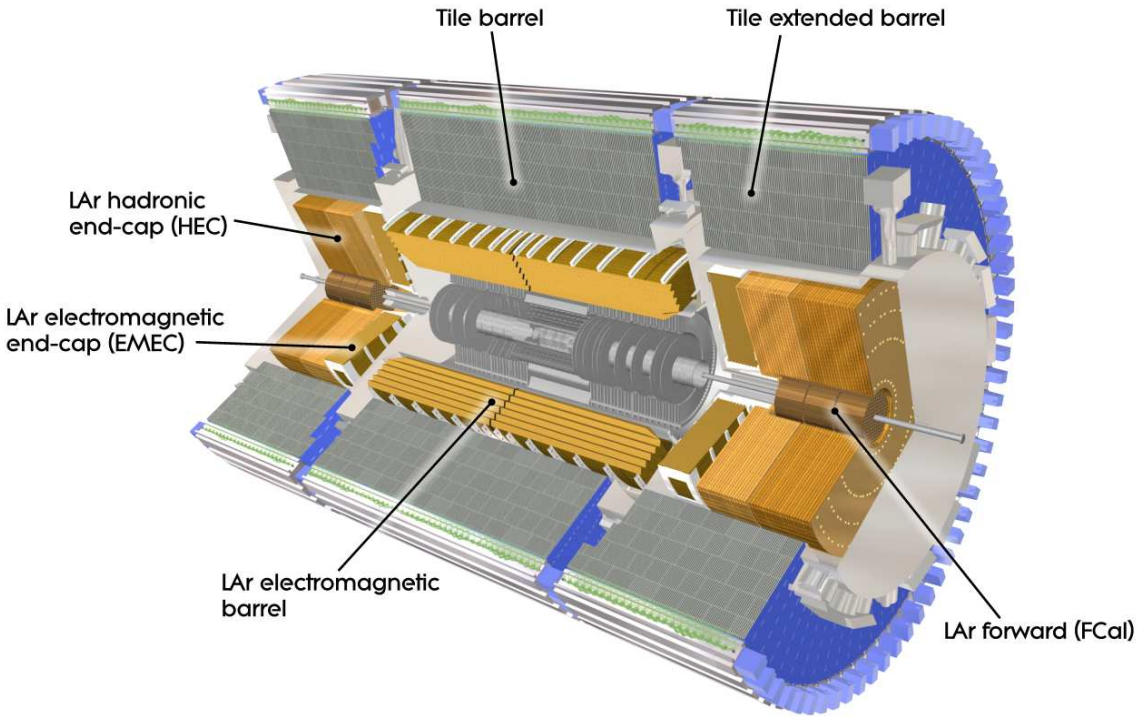

Figure 3.6: A rendering of ATLAS's calorimeter system [29, §5], showing the liquid argon calorimeter in orange on the inside, surrounded by the hadronic tile calorimeter.

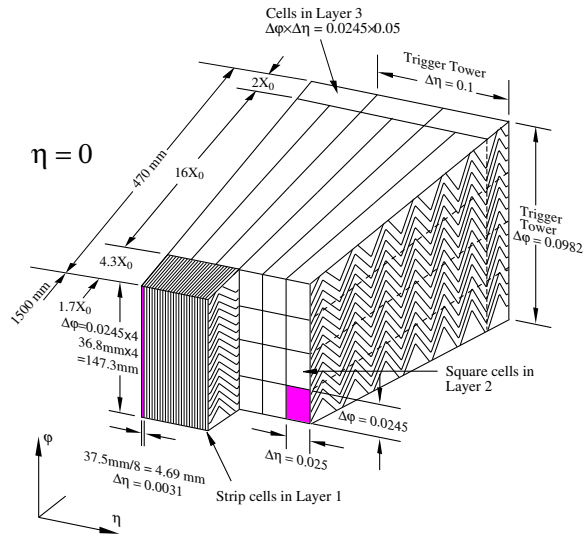

Figure 3.7: A cutaway schematic showing a slice of the LAr calorimeter [36]. The interaction point would be close to the viewer and a particle would travel into the page.

In order to measure the energy it is necessary to fully stop the particle before it leaves the calorimeter, otherwise an unknown amount of energy is unaccounted for. This dictates the size and density of material which is used. Particles are slowed by placing dense material between layers of active material which measure the energy, either by measuring charge generated due to ionisation (for the liquid argon) or scintillation light (in the Tile calorimeter).

Electromagnetic Calorimeter

The ATLAS ECal [37] uses a repeated lead accordion structure which is depicted in figure 3.7. The barrel region covers $\left|\eta\right| < 1.475$, and the end-cap $1.375 < \left|\eta\right| < 3.2$. Liquid argon (LAr) fills gaps between the lead absorbing plates. Charged particles traversing the ECal undergo scattering and emit bremsstrahlung radiation in the presence of the lead.

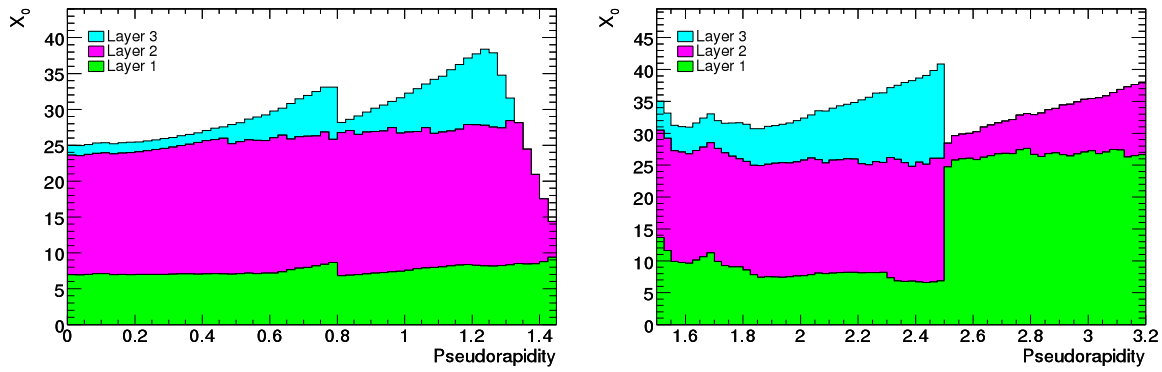

Figure 3.8: Amount of material, measured in radiation lengths, in the three layers of the ATLAS ECal (left) in the barrel, (right) in the end-cap [29].

This radiation can have an energy sufficient for pair production, creating further particles with sufficient energy to also undergo bremsstrahlung. This process branches until the final products do not have enough energy to continue the showering process. The important characteristic of the ECal is the number of radiation lengths (X_0) it presents to high energy particles travelling through it. A radiation length is related to the distance over which an electron loses all but $1/e$ of its energy through bremsstrahlung emission. The ATLAS ECal has a total number of radiation lengths ranging between 25 and 40, varying as a function of $|\eta|$ as shown in figure 3.8.

Particles travelling through the LAr ionize it, creating a charge which is measured using kapton electrodes on the surface of the lead absorbers. This can be used to infer the energy of the original incoming particle. For particles which begin showering before they reach the calorimeter, a thin LAr "*pre-sampler*" is in front of the body of the calorimeter. This can be used to approximate the fraction of the shower that occurred before the calorimeter.

Within the Inner Detector acceptance of $\left|\eta\right| < 2.5$, the ECal is segmented into three layers. The first layer is finely segmented, providing high resolution in η which can be used for good $\gamma/\left([\text{neutral meson}] \rightarrow \gamma\gamma\right)$ separation. The majority of the shower energy is deposited in the middle layer, and the final layer can be used to determine if the shower extends outside the volume of the ECal.

The energy resolution of the ECal varies as a function of energy. It is usually parametrised as [37, 38]:

$$\frac{\sigma(E)}{E} = \frac{a}{\sqrt{E\,(\text{GeV})}} \oplus \frac{b}{E\,(\text{GeV})} \oplus c,$$

with $\oplus$ representing addition in quadrature; $a \approx 10\%\,\sqrt{\text{GeV}}$ represents a stochastic term which accounts for fluctuations due the randomness of the shower evolution, $b \approx 270\,\text{MeV}$ accounts for biases originating from electronic noise, pile-up and other sources, and $c \approx 0.7\%$ characterises all contributions which do not depend on energy; it dominates at high energy.

Hadronic Calorimeter

The hadronic calorimeter [39] is designed to absorb strongly interacting particles before they reach the muon chambers so that their energy can be measured. It consists of three components; in the barrel ($\left|\eta\right| < 1.0$) there is a scintillating tile calorimeter and in the end-cap there are the Hadronic LAr ("*HEC*", up to $\left|\eta\right| < 3.2$) and high density forward calorimeters ("*FCAL*", spanning $3.1 < \left|\eta\right| < 4.9$). Each component has at least three layers to measure the spatial profile of showers. The tile calorimeter has a four to one ratio of steel absorber to active scintillator. Ionizing radiation passing through the scintillator

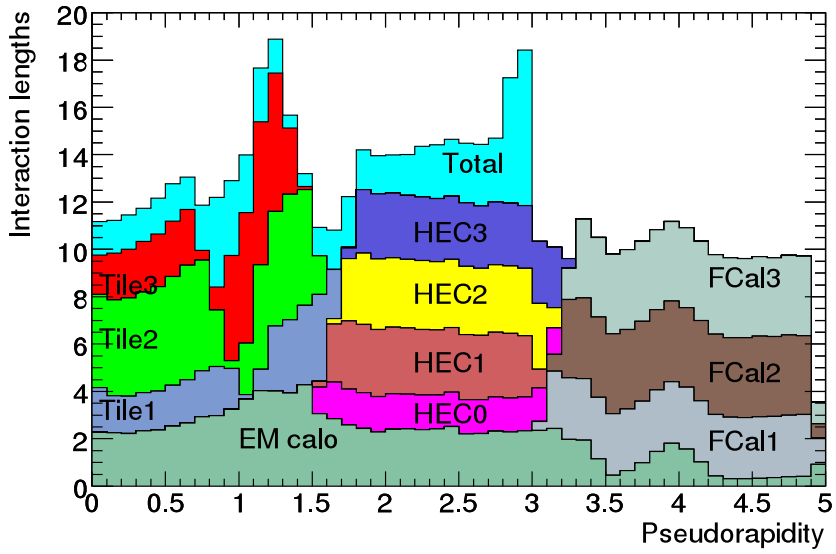

Figure 3.9: Amount of material measured in number of interaction lengths measured as a function of pseudorapidity $|\eta|$ in the ATLAS calorimeters [29].

cause electrons in the material to become temporarily excited. When these return to their ground state they emit ultraviolet photons which are transmitted via wavelength shifting fibres to photomultiplier tubes, where the intensity is measured. The figure of interest for a hadronic calorimeter is the nuclear interaction length. This is defined as the mean distance over which the number of charged particles in a hadronic shower are reduced by a factor of $1/e$. The number of interaction lengths presented by the ATLAS calorimeters ranges from 10-18 and is shown in figure 3.9 as function of $|\eta|$.

3.2.4 Muon Spectrometer

In the Standard Model, aside from neutrinos, muons travel the furthest from the interaction point without decaying. The muon spectrometer is the largest component of ATLAS

and is the other factor (aside from the need to stop particles in the calorimeters) which dictates the detectors largest dimensions. A high magnetic field and long lever arm are neededto measure the curvature of tracks left by high energy muons arising from a hypothetical high mass exotic particle decay (such as the $G \to \mu\mu$) with sufficient resolution. The expected sagitta of a $p_{\mathrm{T}} = 1\,\mathrm{TeV}$ muon travelling across the length of the spectrometer is 0.5 mm [29]. The spectrometer provides an position resolution of $\mathcal{O}\left(30\,\mu\mathrm{m}\right)$. For this analysis, muons are not considered, as their contribution to the $\gamma\gamma$ channel is negligible.

3.3 Trigger and data acquisition

The ATLAS trigger is described in [40, 29] and outlined in figure 3.10. Due to the storage and data management logistics involved, ATLAS is currently limited to recording events at approximately 400 Hz. As mentioned earlier, the LHC produces proton interactions at a rate of $\mathcal{O}$(GHz), most of which are soft strong force interactions; rarer and more interesting events such as those involving the $W^{\pm}$, Z^0 or G^* will occur with a frequency $\mathcal{O}$(10 Hz to 1/month). The ATLAS trigger has the job of determining which events contain interesting physics and should be stored permanently for offline analysis. It must do this at the LHC bunch crossing frequency of 20 MHz. When the trigger has made its decision, the data acquisition system brings together information from all of the different subsystems and records them to disk. The two systems are closely related, and are commonly referred to as TDAQ (Trigger and Data Acquisition).

The trigger [41] is split into three levels called L1 ("*Level 1*"), L2 and the EF ("*Event Filter*"). The first level is implemented in hardware using FPGA boards; the last two are

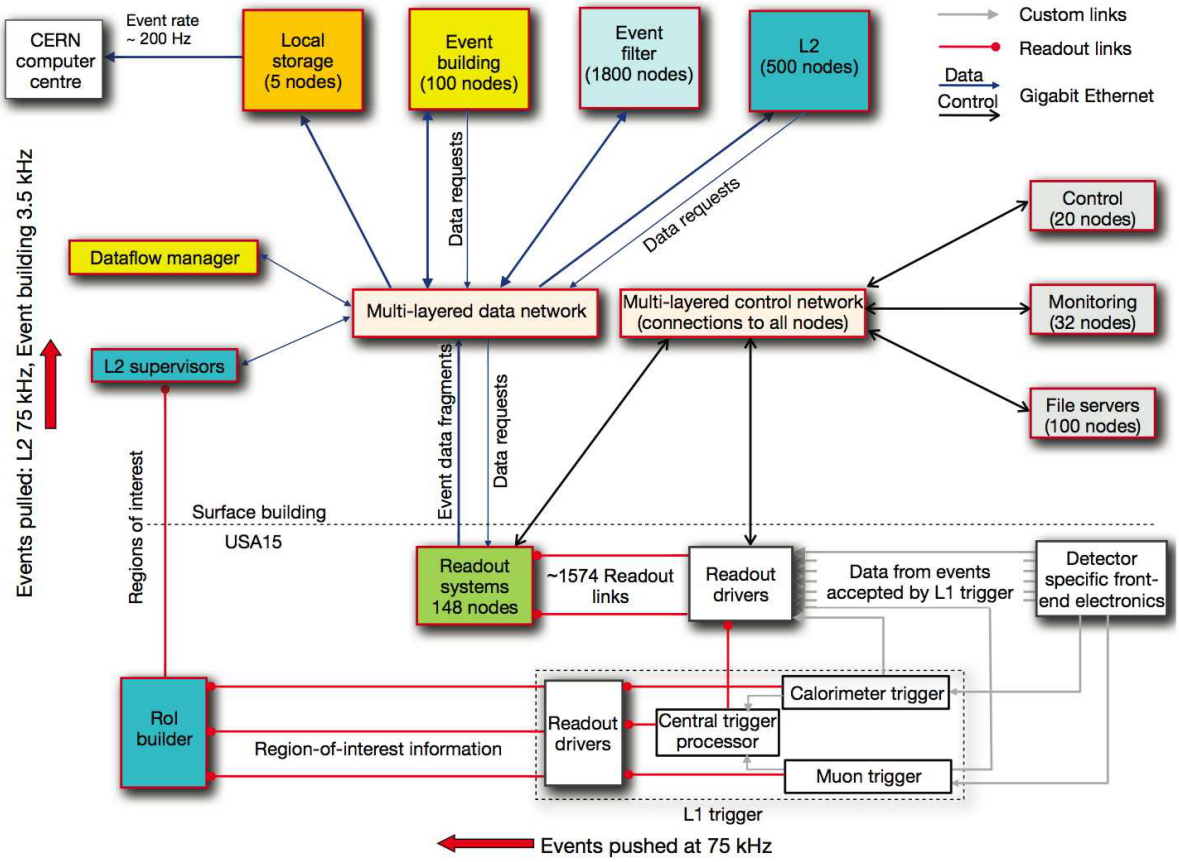

Figure 3.10: A schematic of the ATLAS trigger system [29], showing the detector elements and the logical relationship between different parts of the trigger and the eventual readout.

collectively referred to as the "*High Level Trigger*" and are implemented in software which runs on a cluster of approximately 3,000 computers [42]. Each level uses the previous level as input and makes decisions based on progressively more information about the detector. The L1 trigger considers the calorimeter and muon detector in independent conical regions of the detector referred to individually as a "*Region of Interest*"; it emits positive decisions at a design rate of 75 kHz. L2 runs a partial software reconstruction using sectors of the event based on the geometric regions of interest output from L1. If L2 reports that the event contains interesting candidate physics objects, the EF then performs reconstruction using additional information from the event, at a rate of 3.5 kHz. Finally, if the EF returns a positive result the full event data is written to disk in "`RAW`" format at a rate $\mathcal{O}$ (400 Hz), and eventually copied to the CERN computing centre.

Depending on which triggers an event passes it is then written into one or more logical sets referred to as "*streams*". The stream used in this analysis consists of events with electron and photon candidates. A specific trigger is used which is designed to select events with two photon candidates having $p_{\mathrm{T}} > 20$ GeV and satisfy a set of loose discriminating variable requirements (discussed in section 6.3)[‡], which are guaranteed to be looser than the analysis-level cuts (described in section 7.1) and tighter than the requirements at the L1 and L2 triggers. At L1 the requirement is for two EM clusters with $E_{\mathrm{T}} > 12$ GeV and at L2 there must be two photon candidates with $p_{\mathrm{T}} > 20$ GeV passing looser cuts on the discriminating variables than at the event filter.

[‡]Internally, this is referred to the "`Egamma`" stream and the "`EF_2g20_loose`" trigger.

3.4 Data reprocessing

The reconstruction is dependent on numerous run-dependent calibration constants. Many of these constants are measured during a run and are not available at the time of the first reconstruction, for example the detector alignment and noise. Therefore, the reconstruction is repeated approximately 48 hours later after there has been time to ensure that the constants are in order.

The `RAW` event data amounts to approximately 1 petabyte of data stored per year. This contains the complete information about the event at the original detector granularity. For offline analysis, less information is needed, for example once the four-momentum is derived from track and calorimeter hits, the individual hits can be discarded. For this analysis an official ATLAS file format is used[§], a ROOT [43] file containing a `TTree` with physics data useful specifically to analyses concentrating on photons.

[§]The so-called "`NTUP_PHOTON D3PD`".

Chapter 4

Data Quality

Ratbert (as lab rat, to scientist): *Doc, we have to talk. Every day you feed me over a hundred pounds of macaroni and cheese. At first I thought you were just being a good host. But lately I've been thinking it could be something far more sinister.*

Scientist (thinking): *Macaroni and cheese causes paranoia.*

SCOTT ADAMS, DILBERT

Colour	Nominal meaning
Black	Detector is switched off
Grey	Something went wrong during the automated assessment of the flag
Red	The data are unrecoverable and should be rejected from analyses
Yellow	The data may be recoverable after a reprocessing
Green	No issues reported

Table 4.1: List of meanings of the 2010 data quality flags. One of these five colours was assigned to all subsystems.

As discussed in the previous chapter, ATLAS consists of multiple independent subsystems which work together during data taking to reconstruct physics events. These subsystems may be independently affected by issues leading to data corruption or loss, which needs to be taken into account before the data is used for physics analysis.

ATLAS data is divided into runs and luminosity blocks. The run number is incremented whenever the whole detector is brought together in concert into a stable running state. A luminosity block is a variable length measure of time which represents stable running conditions. A new luminosity block can be started at an arbitrary time, for example if the trigger keys are changed during the run; otherwise they last of the order of one minute.

Data about many aspects of the detector state, for example, voltages and temperatures, are recorded into the so-called "*conditions database*". This information may be recorded with a time stamp, or by run number and luminosity block. Runs and luminosity blocks are used to select which data are good for analyses; if a problem occurs during a luminosity block, potentially the whole luminosity block must be discarded.

4.1 The flags system

During 2010 running each system was assigned, as a function of run and luminosity block, a "*colour*" flag; see Table 4.1 for the list of meanings. This will be referred to as the "*flags system*". Flags were derived automatically, with software such as the DCSCALCULATOR [44] and DQMF [45]. Human judgement was also used before the flags were ultimately summarised, recorded into a COOL database [46, 47] and permanently frozen using COOL's versioning mechanism: tagging. Data analysts were given a set of COOL tags to work with, from which a good runs lists could be derived reproducibly to select data free of issues and suitable for high-quality physics analysis.

The flags system is sub-optimal for an experiment with many collaborators such as ATLAS, primarily because information loss occurs at the point of mapping an issue with a detector onto the limited number of flags available. In the flags system, it is necessary to make a decision about what colour should be assigned to a system shortly after the issue occurs in order to give a prompt turnaround time between data taking and data analysis. As a consequence, the value judgement as to whether a given issue should cause a red flag to be assigned to a system has to be made before there has been time to fully understand the physics implications.

An issue which affects a particular subsystem may not affect all users of that subsystem. For example, during a run with a record-breaking luminosity in 2010, the system for reporting the bunch structure of the LHC fill to ATLAS was incorrectly reporting that a few bunches were not present when they were. Such an issue does not affect most standard analyses, so discarding this precious data would have been a waste. However, specialised

analyses looking for particles with lifetimes much greater than the bunch period may want to look at data recorded when bunches are known to be absent.

Issues such as this may be very hard to communicate to the people who need to know about it, as it is of little interest to the majority of users. The above example makes it clear that it is necessary to record machine readable information about the *issue* present, not just that a *subsystem* is afflicted.

4.2 The defects database

To improve upon the flags system, before the start of 2011 data taking, it was replaced with a new "*defects database*", described in reference [48]. Rather than representing the state of a *detector* as a function of luminosity block with multiple possible colours, merely the presence or absence of *"defects"* are recorded. A defect is any deviation from normal operation which affects data-taking.

Should a defect arise which is not previously encountered, there is no impediment to informing the defects database about it. This is in contrast to the flags system where the number of detector components and possible states was rigid and many pieces of software needed to be modified if a new one was introduced. A binary decision (presence or absence) reduces ambiguity and is less complex than having to choose between multiple possible states. The ability to create a new defect in the database when a new type of issue arises means that the compromises made when selecting a state in the flag system are no longer needed and no information need be lost in the process.

As an optimization, a record is only stored in the database when a primary defect is

present. Since a large number of defects are rarely present, this represents a large space saving. Less manpower is required since it is only necessary to insert records into the database marking known defects, in contrast to the need to accredit each subsystem for whole runs in the previous flags system.

4.2.1 Defect relationships

The defects described so far are "*primary*" defects. These are inserted into the database without consideration as to how they will affect specific physics analyses. Virtual defects are defined in terms of primary defects and other virtual defects. This allows a chain of dependencies to be specified. Figure 4.1 shows the primary defects for one of the virtual defects, and figure 4.2 shows an example virtual defect and its relationship to other defects.

The relationship between defects is also stored inside a folder in the COOL database. This means that all of the information required to make decisions based on defects is stored in the same place. It also allows the use of COOL's versioning system [46] to track changes to the dependencies, in addition to the presence of defects. This means that a single tag can be created which specifies both the contents of the defects and the relationships between them, giving reproducible results even as the defects database evolves.

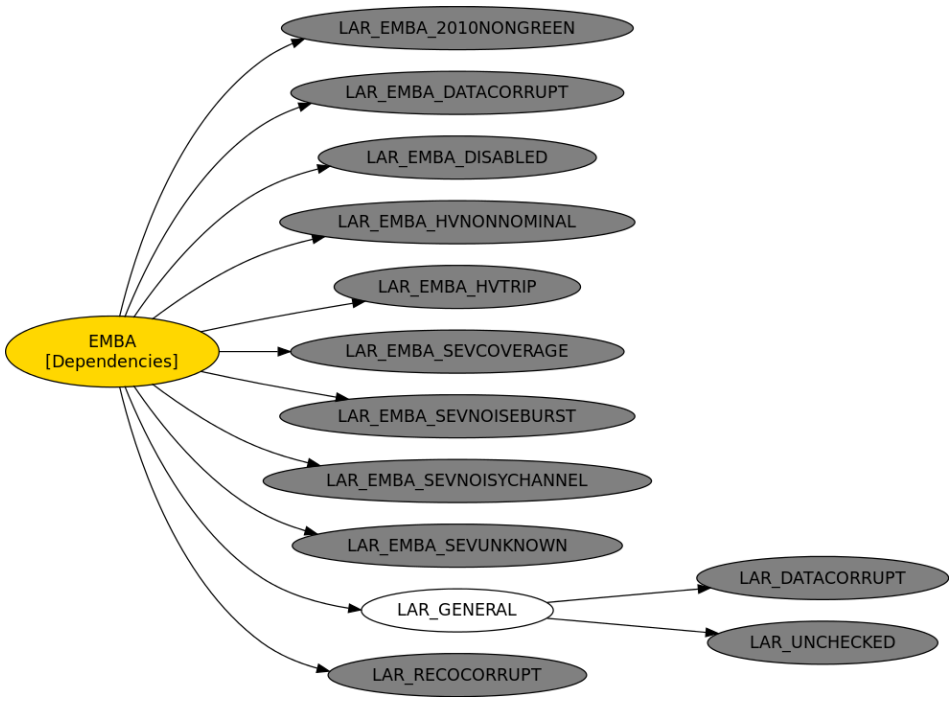

Figure 4.1: A view of the Liquid Argon Electromagnetic Barrel A-side (`EMBA`) virtual defect and its dependencies. Those shown in grey are primary defects. As an illustrative example, `LAR_EMBA_SEVNOISEBURST` represents a condition where a channel has a large amount of noise, rendering it unusable for analyses requiring use of this sub detector.

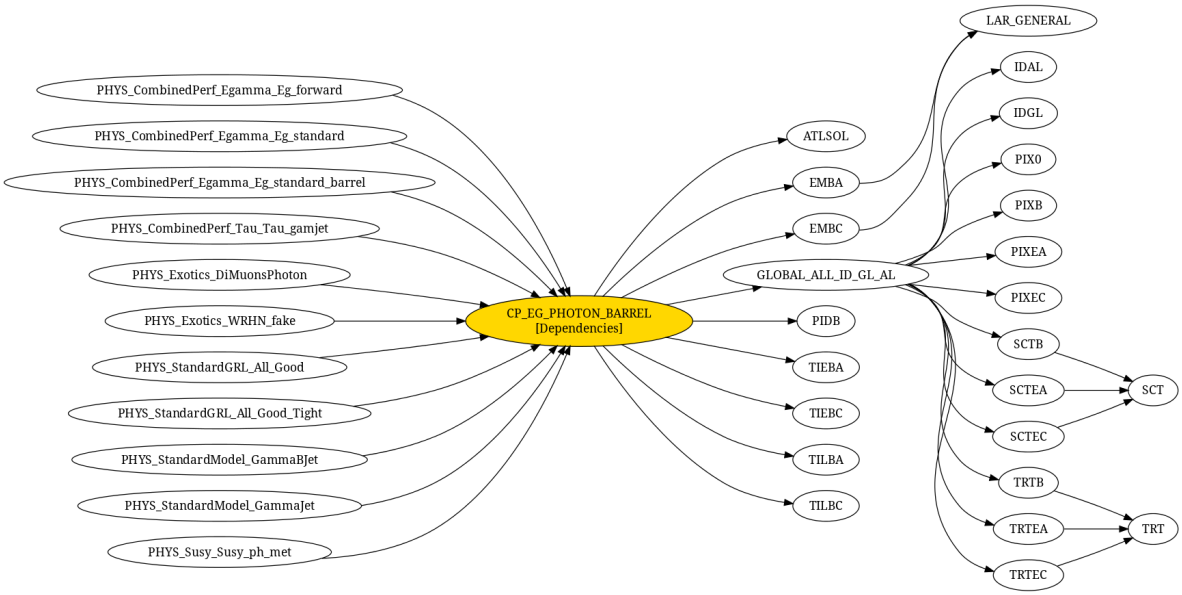

Figure 4.2: A graph showing the defect relationships for the electron-gamma photon barrel combined performance defect (`CP_EG_PHOTON_BARREL`). To the left are the physics flags which depend on it, to the right are the detector components upon which it depends. Listed are the toroidal and solenoidal magnets (`ATLTOR/ATLSOL`), the Liquid Argon (`LAR, EMB`), Tile calorimeter (`TIE, TIL`), Inner-detector alignment and global flags (`IDAL/IDGL`), Pixel (`PIX, PIX0`) and Semiconductor tracker (`SCT`). A suffix of `A/C` indicates the side of the detector, `B/E` indicates barrel/end-cap. The flags with no descendants also depend on primary defects, which are not shown an example of primary defects are shown in figure 4.1.

4.3 Good runs lists

The ultimate medium for communicating which data are suitable for analyses is through a good runs list. This is an XML document containing the run number and luminosity block ranges which are absent of defects. Analysis-specific good runs lists are generated directly from high-level virtual defects whose names are prefixed with "`PHYS_`". As new issues become known, they can be incorporated into appropriate higher-level defects and a new good runs list can be immediately generated.

For the data used in this thesis, the good runs list was generated from the virtual defect "`PHYS_CombinedPerf_Egamma_Eg_standard`", whose immediate dependencies are indicated in Table 4.2. The most luminosity delivered by the machine whilst ATLAS was otherwise ready for data taking which was lost due to these defects was in those starting `CP_` (known as "*combined performance*" flags). This was $\mathcal{O}\left(300\,\mathrm{pb}^{-1}\right)$ with a significant overlap in dependencies in the underlying defects. For the other flags, $\mathcal{O}\left(30\,\mathrm{pb}^{-1}\right)$ was lost to `IDBS/IDVX` and $\mathcal{O}\left(10\,\mathrm{pb}^{-1}\right)$ was lost to `LUMI`. There is likely a significant overlap in the luminosity lost between the defects named in this table.

Defect	Description
GLOBAL_STATUS	The data-quality hasn't been considered, the trigger is not running in a suitable mode, there is a shift in the global ATLAS timing, the LHC is in a special fill, or there is a problem with the offline processing.
IDBS	The beam-spot is not present, out of bounds or there are issues determining its position.
IDVX	Problem with the vertex reconstruction.
LUMI	The beams are moving, a Van-der-Meer scan is taking place, there is an issue with the central trigger, or there are issues with luminosity calibration.
TRIG_GAM TRIG_ELE	Issues preventing the electron or photon trigger from running correctly. Cluster reconstruction or tracking are faulty or only possible for part of the detector. A primary trigger is mis-configured.
CP_EG_PHOTON_BARREL CP_EG_PHOTON_ENDCAP CP_EG_PHOTON_CRACK CP_EG_ELECTRON_BARREL CP_EG_ELECTRON_ENDCAP CP_EG_ELECTRON_CRACK	Combined performance flags: dependencies on the nominal operation of systems necessary for photon and electron reconstruction, including: Tile, LAr, SCT, TRT, Pixels. Also rejects luminosity blocks with no tracks, out of time tracks and software bugs affecting alignment, tracking or clustering.

Table 4.2: A brief description of the defects which must be absent in order for data to be considered in this analysis, as of the tag `DetStatusDEFECTLOGIC-0049` [49].

Chapter 5

Data Samples

This chapter discusses the data used in this thesis. In order to study the impact of the detector, a simulation of the physics and detector is used. A description of the simulated samples used is presented in section 5.2. Section 5.3 discusses how the simulated data are treated in order to match objects from the physics simulation with objects obtained after reconstructing them through the detector simulation. Finally, a special sample referred to as the "*graviton template*" sample is discussed in section 5.4.

5.1 ATLAS data

Data collected by ATLAS in 2011 is used for the results in this thesis. In 2011 the LHC delivered a total of $5.6\,\mathrm{fb}^{-1}$ at a centre of mass energy of $\sqrt{s} = 7\,\mathrm{TeV}$, representing $4.91\,\mathrm{fb}^{-1} \pm 1.8\%$ collected with stable detector conditions and good data quality suitable for photon analysis. Figure 5.1 shows the amount of luminosity collected as a function of time.

The data sample used is derived from the Egamma stream (see section 3.3), with cuts requiring two objects either of which can be an electron or photon with an uncorrected $E_{\mathrm{T}} \geq 20\,\mathrm{GeV}$* and standard data quality requirements† as described in section 4.3.

*Internal detail: The AMI tag for this sample is `p682_p868`, which are the `NTUP_PHOTON` datasets produced from `D2AOD_DIPHO`.

†Derived from the good run list `data11_7TeV.periodAllYear_DetStatus-v36-pro10_CoolRunQuery-00-04-08_Eg_standard.xml`

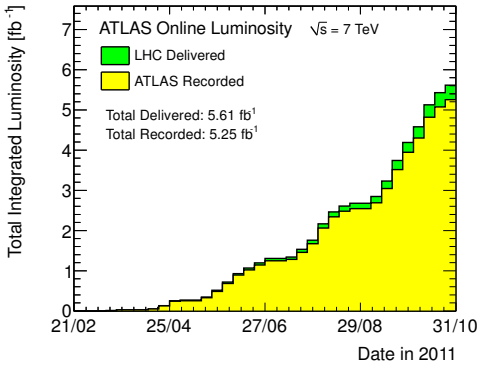

Figure 5.1: Cumulative total luminosity delivered by the LHC during 2011, by week [33, 34]. The green histogram shows the amount of luminosity delivered and the yellow the amount recorded by ATLAS.

5.2 Detector simulation and Monte Carlo samples

The simulated samples used in this analysis were all produced via ATLAS's official production system [50, 51]. In these samples, PYTHIA 6.4.25 [52] simulates proton-proton interactions and then emits the set of particles which participated, along with information such as their four-vectors. The `MRSTMCal` PDF sets [8] from LHAPDF [53] version 5.8.5 were used. The final-state particles participating in the interaction are then input into a simulation of the ATLAS detector using GEANT 4 [54].

Table 5.1 shows the background samples used in this analysis. As the invariant mass distribution for these samples is steeply falling, they are simulated in separate bins of p_{T} so that there is sufficient statistics in each bin. The events are weighted according to the cross-section and number of events in that p_{T} bin so that they represent the amount of luminosity in the data.

The simulated signal samples are shown in table 5.2. The most useful of these was

the template sample, which is used to perform most of the signal studies and derive the templates used to model the signal templates for limit setting in section 8.4. The other resonances in this table are used as a cross-check to ensure that the template sample re-weighting described in section 5.4 gives a good description of the resonances and to study resonances with a small $k/\overline{M_{\mathrm{pl}}}$ (and therefore width), for which the template sample does not have sufficient statistics.

5.2.1 Pile-up re-weighting

Due to how long it takes to generate simulated data samples, it is necessary to commence their creation before data taking. The conditions of data-taking were unknown and unpredictable at that point, especially due to the period of rapid machine development that the LHC undertook during 2011. In particular, the expected $\langle\mu\rangle$ (*c.f.* figure 3.2) was unknown and therefore simulated samples contained a range of this value with a "best guess" for what this value would be. It is important that this distribution is well modelled in the simulated samples especially because of the impact that the multiple interactions have on the detector occupancy, energy reconstruction and isolation measurement (see section 6.4). All simulated samples are therefore re-weighted per event using an official tool called `TPileupReweighting`[‡] so that the $\langle\mu\rangle$ distribution of the simulated samples agree with the data.

[‡]Internal reference:
https://twiki.cern.ch/twiki/bin/viewauth/AtlasProtected/ExtendedPileupReweighting

Physics Content	Name	AMI Tag	Dataset Number	Short Name	$L_{\text{effective}}$ $\left[\text{fb}^{-1}\right]$	N	Cuts [GeV]
parton-parton $\rightarrow \gamma + \text{jet}$	Filtered Direct Photon	e825 s1299 s1300 r3043 r2993 p868	115802	DP17	1,450	2,998,700	$20 \leq p_{\text{T}} < 45$
			115803	DP35	54	3,000,000	$45 \leq p_{\text{T}} < 85$
			115804	DP70	2	2,999,300	$85 \leq p_{\text{T}} < 150$
			115809	DP140	1.8×10^{-1}	2,000,000	$150 \leq p_{\text{T}} < 300$
			115810	DP280	1.6×10^{-2}	1,999,500	$300 \leq p_{\text{T}} < 550$
			119077	DP500	1.3×10^{-3}	2,000,000	$550 \leq p_{\text{T}}$
parton-parton $\rightarrow \gamma\gamma$	Standard Model Irreducible		105964	N/A		200,000	$15 \leq m_{\gamma\gamma} < 200$
			119584		143.5	200,000	$200 \leq m_{\gamma\gamma} < 800$
			145606		9,224	80,000	$800 \leq m_{\gamma\gamma} < 1500$
			145607		60,711	20,000	$1500 \leq m_{\gamma\gamma}$

Table 5.1: Simulated background samples. Cuts are in units of GeV. The effective luminosity (L_{eff}) shows the equivalent amount of luminosity given the leading order cross-section of the sample and the number of events (N) generated.

Mass [GeV]	$k/\overline{M_{\mathrm{pl}}}$	Width [GeV]	$L_{\mathrm{effective}}$ $\left[\mathrm{fb}^{-1}\right]$	N	Dataset Number
(Template)	N/A	N/A	7.6×10^{-11}	400,000	145536
300	0.01	0.041	8.98	10,000	106684
500	0.01	0.068	112.5	10,000	105623
	0.03	0.639	12.55	10,000	106644
700	0.01	0.095	357.9	5,000	115557
	0.03	0.894	39.49	5,000	115558
	0.05	2.49	29.1	10,000	105835
800	0.01	0.109	1,576.	10,000	106623
	0.03	1.02	174.6	10,000	105833
	0.05	2.85	31.51	5,000	115559
	0.1	11.4	15.99	10,000	105838
900	0.03	1.15	179.7	5,000	115560
	0.05	3.21	64.97	5,000	115561
	0.07	6.29	33.38	5,000	115562
	0.1	12.8	16.72	5,000	115563
1000	0.01	0.136	6,313.	10,000	106643
	0.03	1.28	695.4	10,000	105834
	0.05	3.56	251.7	10,000	105836
	0.1	14.3	64.1	10,000	105839
1100	0.05	3.92	228.5	5,000	115564
	0.07	7.69	118.5	5,000	115565
	0.1	15.7	58.31	5,000	115566
	0.2	62.9	14.99	5,000	115567
1250	0.05	4.45	1,088.	10,000	105324
	0.07	8.74	277.6	5,000	115568
	0.1	17.8	273.	10,000	105841
	0.15	40.2	60.75	5,000	115569
	0.2	71.4	34.55	5,000	115570
1500	0.05	5.34	3,851.	10,000	105837
	0.1	21.4	980.3	10,000	105842
1750	0.1	25.0	3,019.	10,000	119870
2200	0.1	31.4	8,613.	10,000	119871
2250	0.1	32.1	23,200.	10,000	119872

Table 5.2: Graviton signal samples and their properties. Mass and $k/\overline{M_{\mathrm{pl}}}$ fully specify the physical model. Width is the partial width in the $\gamma\gamma$ decay channel of the resonance measured by fitting the truth-level diphoton invariant mass with a Breit Wigner [55] distribution. The effective luminosity $\left(L_{\mathrm{eff}}\right)$ shows the equivalent amount of luminosity given the leading order cross-section of the sample and the number of events (N) generated. The dataset number identifies the dataset inside ATLAS.

5.3 Monte Carlo truth matching

Two truth matching methods were used for studying detector effects, in this thesis referred to as *"forward matching"* and "*backward matching*". For reconstruction and purity studies, backward matching is used. The official ATLAS truth matching algorithm is used, which, given a reconstructed photon finds the final state truth particle with the smallest distance in angular space ($\Delta R = \sqrt{(\Delta\eta)^2 + (\Delta\phi)^2}$) between the two particles considering only true particles with $p_{\mathrm{T}} > 1\,\mathrm{GeV}$.

For efficiency studies, forward truth matching is used. This is because generated particles may not end up with any representation as a reconstructed photon. The forward matching implementation for this analysis takes the two highest p_{T} photons from the truth container which come from the hard process. For each of these it tries to find a reconstructed photon whose backward-matching reconstructed particle is the truth particle in question. If there is no backward match it may be that it was instead reconstructed as a different physics object, in which case it does not enter into the analysis. There may be more than one backward match for a given generated particle, in this case the one with minimum $\left|p_{\mathrm{T}}(\text{generated}) - p_{\mathrm{T}}(\text{reconstructed})\right|$ is used.

5.4 Graviton template sample

The template sample (dataset number 145536) was generated by modifying the PYTHIA 6 source code[§]. The purpose of this sample is to provide high statistics in bins of $m_{\gamma\gamma}$. The

[§]Internal Reference:
https://twiki.cern.ch/twiki/bin/viewauth/AtlasProtected/GravitonTemplate

mass distribution is approximately flat in the true $m_{\gamma\gamma}$. This sample provides the possibility of smoothly varying the graviton's coupling and mass to arbitrary values without needing to re-do the expensive detector simulation. This makes the sample ideal for looking at trends of various detector effects such as efficiencies, which are considered in later chapters.

The template sample was made by applying ad-hoc corrections to PYTHIA 6. The Breit-Wigner term and modifications to the off-shell portion of the distribution are removed for both gg and $q\bar{q}$. Owing to the variation in branching fractions of the quark and gluon production mechanisms with respect to m_G, the shape of the mass distribution is affected by contribution of gg and $q\bar{q}$ which also varies with mass. This is taken into account with a scale factor. Incidentally, this is the main reason that the Parton Density Functions are the main contributor to systematic uncertainty in the Gravtion cross section (see section 9.2).

The following weight can be applied to an event with a given $m_{\gamma\gamma}$ in order to recover a graviton mass distribution with a chosen pole mass m_G and width Γ_G:

$$w\left(m_{\gamma\gamma}; m_G, \Gamma_G\right) = \underbrace{\frac{1}{\left(m_{\gamma\gamma}^2 - m_G^2\right)^2 + m_{\gamma\gamma}^2 \Gamma_G^2}}_{\text{Breit-Wigner}} \tag{5.1}$$

$$\times \underbrace{\left(\frac{m_{\gamma\gamma}}{m_G}\right)^4}_{\text{off-shell}} \tag{5.2}$$

$$\times \underbrace{A\left(m_{\gamma\gamma}\right) \exp\left(B\left(m_{\gamma\gamma}\right) m_{\gamma\gamma}\right)}_{\text{parton luminosity scale factor}} \tag{5.3}$$

where A and B are factors which were derived in order to flatten the distribution in the different regions. This weight recovers the graviton line shape; a further correction is necessary to recover the correct cross-section:

$$\frac{\sigma_{\text{resonance}}}{\sigma_{\text{template}}}\left(x \equiv \frac{k}{\overline{M_{\text{pl}}}}\right) \approx -0.00100207 + 0.155519x - 6.36193x^2 + 91.9095x^3 + 9855.22x^4$$

where $\sigma_{\text{resonance}}$ and σ_{template} are the cross-sections of the desired resonance and the template sample after being re-weighted with $w\left(m_{\gamma\gamma}; m_G, \Gamma_G\right)$. The cross-section factor was obtained by fitting the quartic polynomial to scale factors obtained from all available resonant samples. For a given resonant sample, the scale factor was obtained by integrating the weights in a bin $m_G - 5\Gamma_G < m_{\gamma\gamma} < m_G + 5\Gamma_G$ propagating the uncertainty with the weights taken into account. The resulting factor and its percentage uncertainty are shown in figure 5.2. The uncertainty grows large to small values of $k/\overline{M_{\text{pl}}}$ because the resonance gets very narrow. As a consequence of this narrowness, the weights of a small number of events grow large.

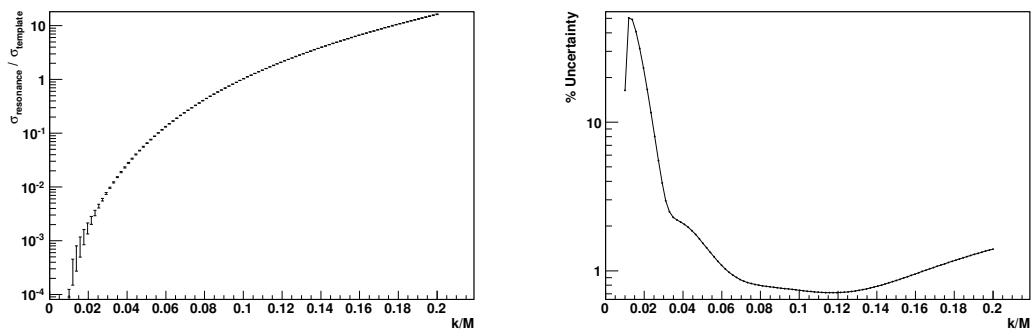

(a) (b)

Figure 5.2: (a) Factor applied to re-weight resonance as a function of k/M, (b) relative uncertainty quoted as a percentage

Chapter 6

Photon Reconstruction

A careful analysis of the process of observation in atomic physics has shown that the subatomic particles have no meaning as isolated entities, but can only be understood as interconnections between the preparation of an experiment and the subsequent measurement.

ERWIN SCHRÖDINGER

Physics reconstruction (hereafter just "*reconstruction*") is the process of taking detector data for one bunch crossing and inferring what happened. It is described in detail in [56]. Reconstruction involves taking the data from a number of detectors (discussed in detail in chapter 3), combining them into meaningful physics objects and associating those with the independent collisions (vertices) which occurred during the bunch crossing. The sensitivity of the search for gravitons is ultimately limited by the ability of the reconstruction to correctly identify true photons with high efficiency and to reject signals originating from non-photons, resulting in a sample with a high purity.

This chapter will focus on how a photon ends up in the "*photon container*", and ultimately the physics analysis.

6.1 Backgrounds to photon measurements

An important aspect of high-p_{T} ($\gtrsim 100\,\mathrm{GeV}$) photon reconstruction is to maximise the rejection of non-photon signals. The primary source of non-photons faking a photon signal are decays of π^0 and η particles to $\gamma\gamma$, which happen at a high rate at ATLAS. Figure 6.1 shows event displays taken from 2011 data, exhibiting a probable direct photon event and a meson decay.

The opening angle of $\pi^0 \to \gamma\gamma$ decay, α, peaks of at $\alpha_{\mathrm{min}} \propto m/E$, where α_{min} is the minimum opening angle and m and E are the mass and energy of the original particles respectively. For neutral particle decays with an $E \sim 1\,\mathrm{TeV}$ and $m \sim 100\,\mathrm{MeV}$, $\alpha_{\mathrm{min}} \sim \Delta\eta|_{\eta=0} \sim 10^{-4}\,\mathrm{rad}$, far below the granularity of the first layer of the EM calorimeter. Therefore these objects can appear in the reconstruction as a single object. Neutral mesons

are constituents of jets which are produced at a high rate at ATLAS, therefore they will be the focus of the discussion of the reconstruction during this chapter.

Electrons can also be misidentified as photons if their track is not reconstructed correctly. This has been measured to occur at a rate of approximately $2-7\%$ depending on location in the detector for single electrons studied under the Z^0 peak [57]. Since this must occur twice in coincidence to enter into this analysis, this effect will be neglected.

6.2 Reconstruction strategy

Photon reconstruction begins by looking for energy deposits in the electromagnetic calorimeter. Candidate photon objects are conceptually placed in the photon container for analysis downstream. Initially this container will necessarily contain many physics objects which are non-photons. This is due to the large number of events originating from jets, some of which produce photon-like objects. The relative cross-section for dijet and diphoton events with an invariant mass of 100 GeV is $\mathcal{O}\left(10^4\right)$ [58, 59]; therefore there is a requirement to use cuts which give a high efficiency for signal events and rejection factor for background events, which will be covered in section 6.3.

At the analysis stage, a pure sample of photons is selected by placing cuts on the discriminating variables, discussed in section 6.3. The definition of the discriminating variables and the cuts placed on them are tuned in the simulation, optimising for a reasonable trade-off between photon efficiency ("how many real photons are rejected from the analysis") and purity ("what fraction of the resulting photon sample came from non-photons").

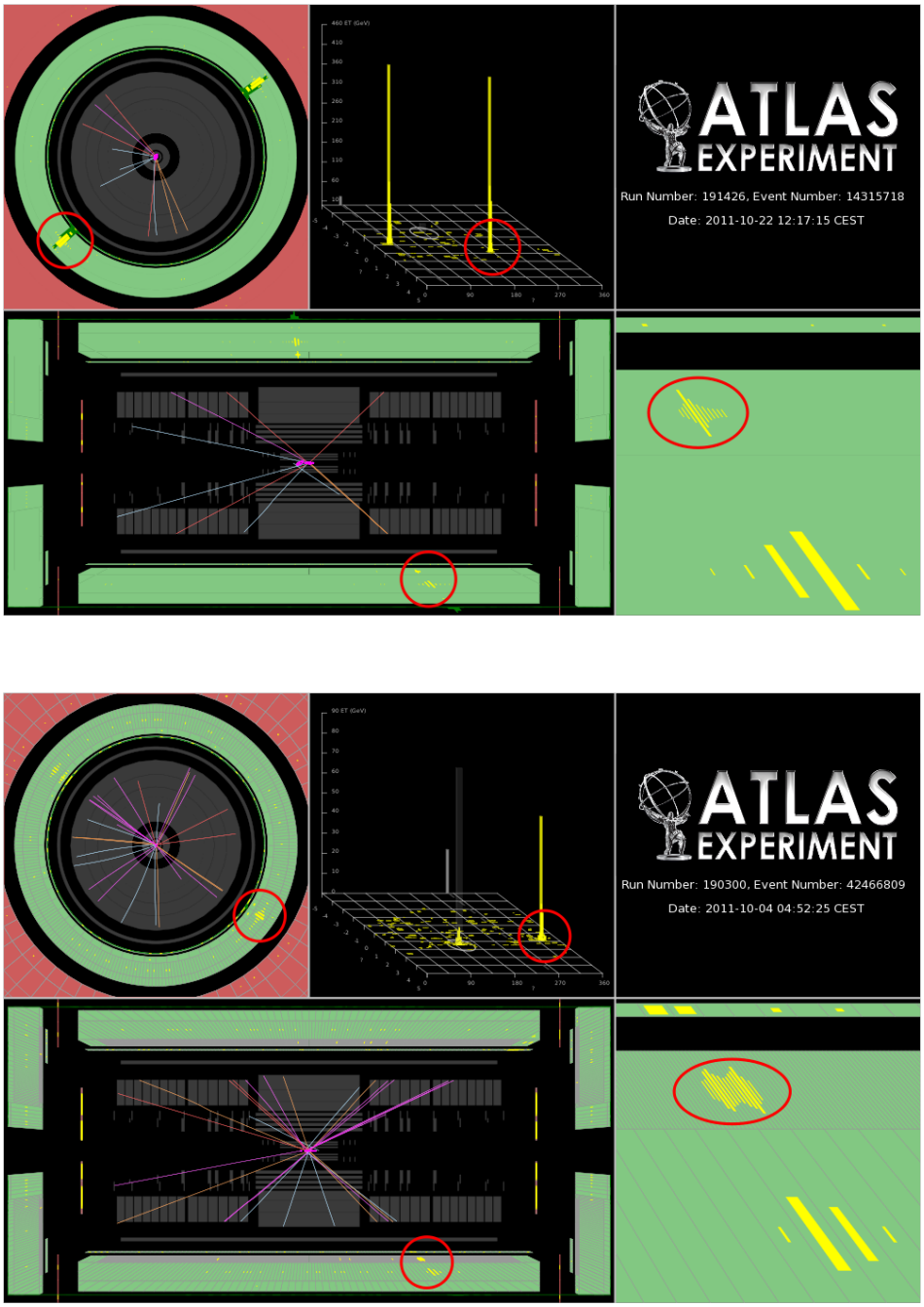

Figure 6.1: Event displays illustrating a probable photon (above) and π^0 decay (below) in the detector from 2011 data. The object of interest is circled in red. The display windows are (clockwise from top left) 1) An orthographic projection of the $r-\phi$ plane (*i.e*, looking down the beam-pipe), 2) a lego plot showing the energy depositions as a function of η and ϕ, 3) a window showing details which identify the event. 4 and 5 both show the $r-z$ plane with the 4th showing an enlarged portion of the 5th window, focussing on the object of interest. The two-photon separation of the π^0 decay can clearly be seen in the 4th figure.

Electron and photon reconstruction are similar processes, both of which are described in [60]. Towers of cells are constructed by summing energy across the three calorimeter layers in regions of size $\Delta\eta \times \Delta\phi = 0.025 \times 0.025$. A "sliding window" algorithm picks out clusters from the towers by placing a rectangle of 3×5 cells at each location where the total energy exceeds $E_{\mathrm{T}}^{\mathrm{thres}} = 2.5\,\mathrm{GeV}$. If seed clusters overlap with a barycentre (weighted according to energy) separation less than 2×2 in units of cell size, the cell with the smaller energy is removed.

The Inner Detector measures space points, from which tracks are reconstructed. The tracks are extrapolated from their last measured point into the second layer of the calorimeter [61]. If the η and ϕ co-ordinates of the extrapolation at the second layer are both approximately 0.1 units from the cluster, it is considered to have matched it. Tracks originating from the vertex are assumed to be electrons and are put into the "*electron container*". Other tracks with vertices originating from inside the Inner Detector volume potentially originate from photon conversions and are placed into the photon container. Figure 6.2 shows the probability that a photon will convert before a given radius as a function of radius.

Sometimes one of the electrons from a conversion is not reconstructed, especially at a high radius in the Inner Detector. These account for a significant number of conversions, see figure 6.3. To reduce the resulting loss in efficiency, ATLAS can reconstruct these as "*single track conversions*" by considering the shower shapes profiles to see if they fit the single electron reconstruction hypothesis. The total efficiency after recovering these photons as a function of radius is also shown in figure 6.3.

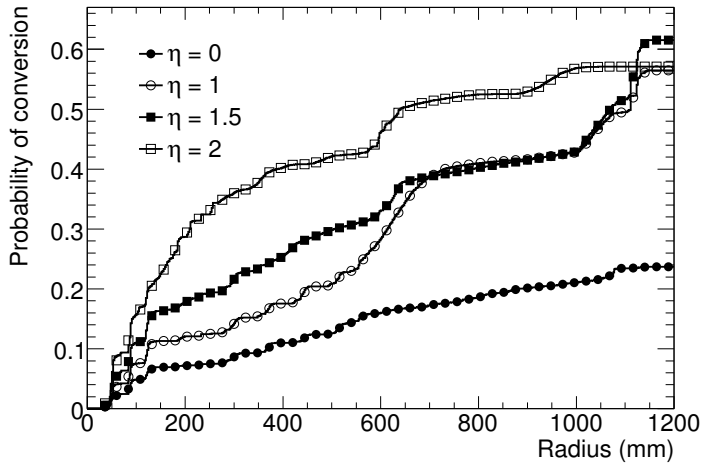

Figure 6.2: Probability that a photon converts before a given radius as function of radius, measured in the simulation. Shown at different values of $|\eta|$ and measured with simulated minimum bias photons with $p_{\mathrm{T}} > 1\,\mathrm{GeV}$ from [56]. The final conversion probability is approximately 60% for forward photons, decreasing to 20% in the central region.

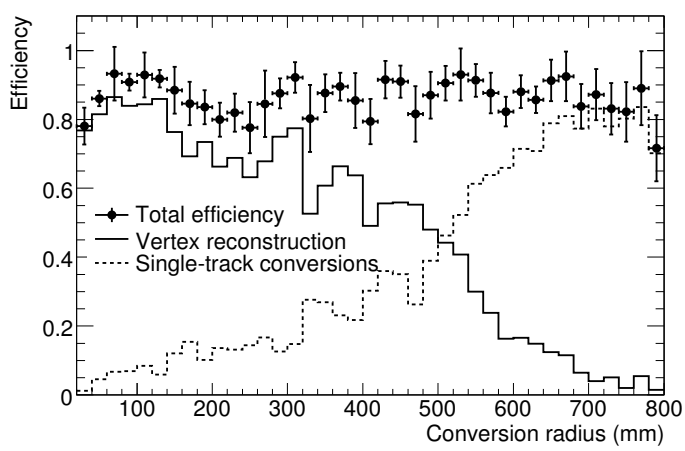

Figure 6.3: Photon reconstruction efficiency as a function of radius for single/double track conversions, measured in the simulation [56]. Reconstructing single track photons (dashed) allows the total efficiency for converted photons to be recovered at higher radius, despite the losses due to one of the tracks not being reconstructed.

6.3 Discriminating variables and photon identification

The following section describes a set of variables used to differentiate between "*true photons*" (those which occur at the interaction vertex) and other objects (such as π^0 decay) which occasionally end up in the photon container. This differentiation is imperfect due to limitations arising from the detector such as the spatial and energy resolution. These variables are widely used in the ATLAS collaboration and standard cuts have been defined against them which have been defined so as to optimize the efficiency and purity of the resulting photon sample [62]. These are colloquially referred to as "*object quality*" cuts.

These variables are defined in terms of the three layers of the calorimeter described in section 3.2.3. For this analysis, it is particularly important to discriminate against high p_{T} neutral mesons faking a photon signal. These particles are accompanied by a jet and therefore deposit a significant amount of energy into the hadronic calorimeter, unlike photons. This makes the ratio of energies deposited in the hadronic calorimeter to the EM calorimeter ("R_{had}") one of the stronger cuts against neutral mesons. After this, the coarse grained second layer of the EM calorimeter is used to measure the wider hadronic jets. The innermost EM calorimeter strips, mentioned in section 3.2.3, have the finest granularity. These are used to measure the profile of the shower which can be indicative of a two photon decay from a neutral meson.

Illustrative plots of the different shower shape variables are shown in figures 6.4, 6.5 and 6.6, derived from the sample with the short name "`DP500`" described in section 5.2. The figures show all photon objects with a reconstructed $p_{\mathrm{T}} \geq 500\,\mathrm{GeV}$ which were successfully matched to a truth object using backwards truth matching described in

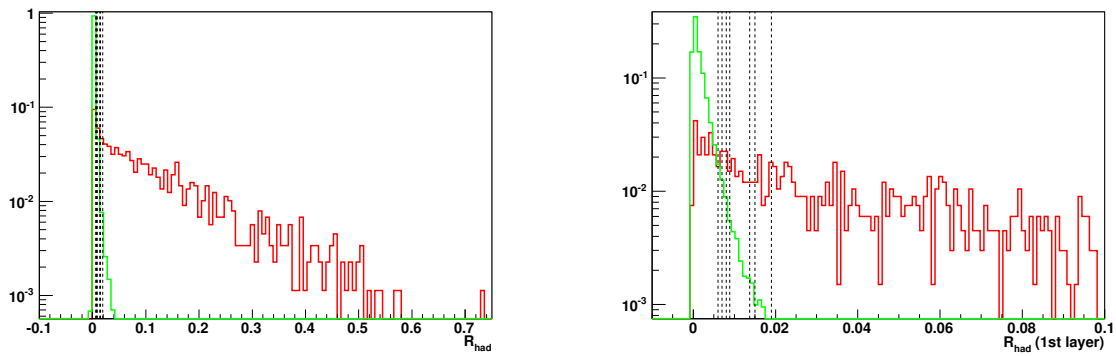

(a) R_{had} : Ratio of $E_{\text{T had}}$ to the transverse energy measured in the EM calorimeter

(b) R_{had1} : Ratio of $E_{\text{T had1}}$ to the transverse energy measured in the EM calorimeter

Figure 6.4: Illustrative shape comparison of hadronic calorimeter shower variables, individually normalized.
Key: (see text) Signal, Fakes. The plots are integrated over η; dashed lines, if present, indicate positions of cuts, one per η bin.

section 5.3. The object is classified as signal if the photon came from the hard process and fake otherwise. The distributions are independently normalized to highlight the shapes of the distributions without consideration of the rates of the signal and fake processes.

Cuts are applied in each of the discriminating variables, which are specialized in separate bins in η to optimize the efficiency. The cuts are, by section of the detector:

- Hadronic Calorimeter (figure 6.4)
  - A ratio of the amount of energy in the HCal to the amount in the ECal. There are two different variables used in different η regions, R_{had_1} is used for $|\eta| < 0.8$ and $|\eta| > 1.37$ and R_{had} is used over $0.8 < |\eta| < 1.37$. R_{had_1} is computed using only detector components in the first layer and is preferred where it is physically present. This is because there is a level of noise in the calorimeter;

since the majority of the energy is deposited in the first layer, summing across remaining layers worsens the resolution in R_{had}.

- Middle layer (figure 6.5)
  - R_η (loose) and R_ϕ (tight): Ratios between sums of energies over cells. R_η is a ratio of cell energies centred on the cluster $(\eta \times \phi)$ $\frac{3\times7}{7\times7}$ and R_ϕ is $\frac{3\times3}{3\times7}$.
  - Width of the shower in units of η in the η direction $w_{\eta 2}$ (tight).

- Strip layer (figure 6.6)
  - w_{s3}: The weighted shower width in units of number of strips for the strip with the maximum energy and its two neighbours, defined as:

$$w_{s3} = \sqrt{\frac{\sum_i \left(i - i_{\text{centre}}\right)^2 \times E_i}{\sum E_i}},$$

    where i is the index with of the cell and i_{centre} is the index of the cell with the maximum energy. The summation runs over 3 strips.
  - $w_{s\,\text{tot}}$: Total shower width, defined in the same way as w_{s3} except the summation runs over 20 strips ($\Delta\eta = 0.0625$).
  - f_{side} : Fraction of energy outside core of three central strips but within seven strips.
  - ΔE : Defined as $E_{\text{max}2} - E_{\text{min}1}$ where $E_{\text{max}2}$ is the energy of the cell with the second-highest energy and $E_{\text{min}1}$ is the cell with the minimum energy which

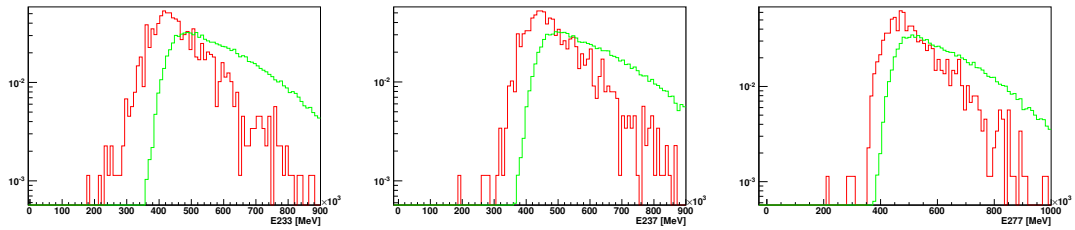

(a) E_{2XY}: Energy in a window of size $X \times Y$ in $\eta \times \phi$.

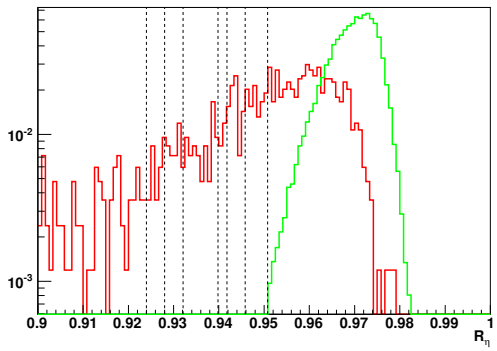

(b) R_η : Ratio of $\frac{E_{237}}{E_{277}}$.

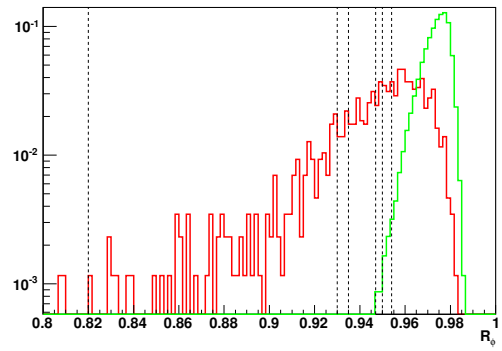

(c) R_ϕ : Ratio of $\frac{E_{233}}{E_{237}}$.

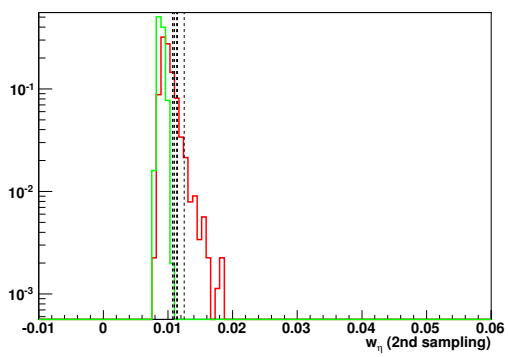

(d) $w_{\eta 2}$: Shower width in the η direction in units of η.

Figure 6.5: Illustrative shape comparison of middle layer EM calorimeter variables, individually normalized.
Key: (see text) Signal, Fakes. The plots are integrated over η; dashed lines, if present, indicate positions of cuts, one per η bin.

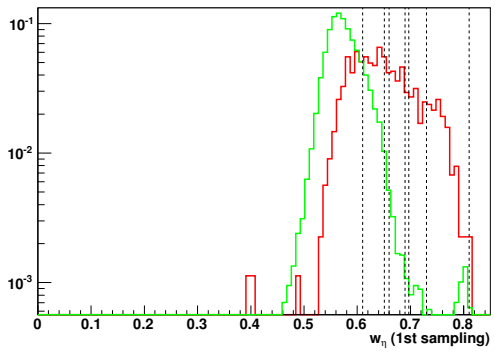

(a) w_s : measured in three strips around and including the maximum cell.

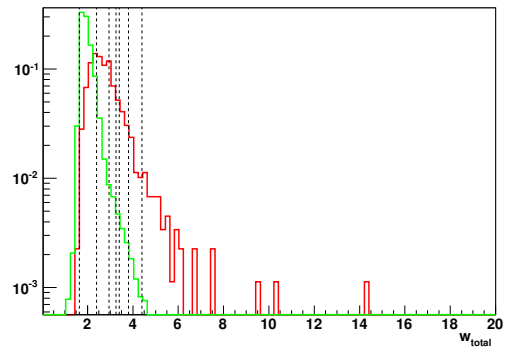

(b) $w_{s\,\mathrm{tot}}$: Total shower width.

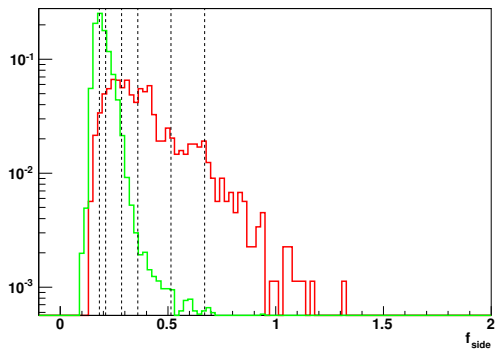

(c) f_{side}: Fraction of the total cluster energy which is not in the central three strips.

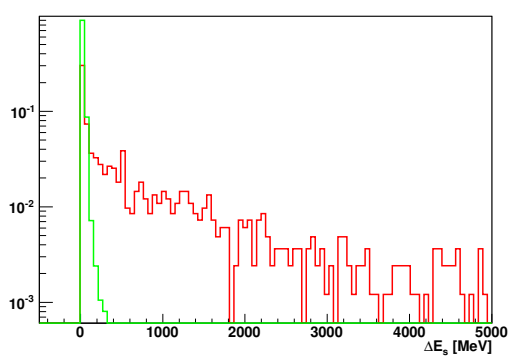

(d) ΔE_s : Difference in energy between the cell with the maximum energy and the cell with the minimum energy.

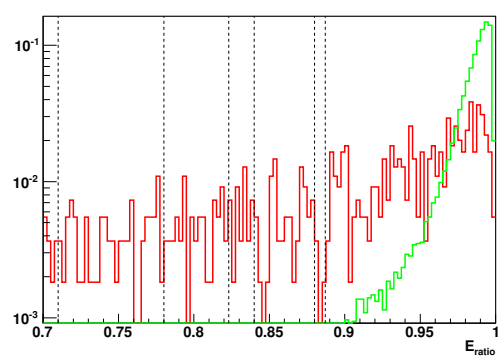

(e) E_{ratio} : Ratio between ΔE_s and the total energy in the cluster.

Figure 6.6: Illustrative shape comparison of strip layer variables, individually normalized. Key: (see text) Signal, Fakes. The plots are integrated over η; dashed lines, if present, indicate positions of cuts, one per η bin.

lies between the cells with the maximum and second-maximum energies. For objects which have two distinguishable peaks this is non-zero.

– E_{ratio} : Ratio of the energy difference between the largest cell and second largest over the sum. This is used to identify $\gamma\gamma$-like signals. If the two peaks have similar size, it is more likely to have come from a $\gamma\gamma$, otherwise one of them will just contain noise and the ratio will be large.

All of the above cuts are used for the "*tight*" selection in this analysis. It provides an efficiency for signal photons of approximately 85% and a background rejection factor around 5000 [63]. Some of these cuts are inverted in order to obtain background enriched samples used to obtain the background estimate in section 8.2.1. The top ten highest mass candidate diphoton events in 2011 are presented in appendix B showing their discriminating variables.

6.4 Isolation

In addition to the above discriminating variables, "*isolation*" is used as a powerful veto against jet-like objects. This is defined as the amount of energy surrounding the photon in a cone, minus the amount of energy belonging to the photon itself. Objects which fake photons are accompanied by many other objects which decay into a cone, elevating the level of energy in nearby cells. For this analysis, a cone of $\Delta R = 0.4$ is used with a cut of $E_{\text{T}}^{\text{iso}} < 5\,\text{GeV}$. The isolation is also used to estimate the amount of irreducible background present in the data in section 8.2.

6.5 Post-reconstruction corrections

In ATLAS there exist official software tools made by groups of specialists who focus on machine performance. The tools apply corrections to the data which improve agreement between the simulated samples and that which is measured by the detector. Such tools are applied after the physics reconstruction has taken place, during the final stage of the analysis. An example of such a tool is the pile-up re-weighting mentioned in section 5.2.1. As with the pile-up re-weighting there are other features of the simulation which were decided before the actual performance of the detector was known. Such features include things which affect the identification discussed previously in this chapter, the isolation, and the energy scale.

Given a sample of simulated events, the detector resolution can be trivially worsened by adding an additional term to the measured energy of a photon which is randomly distributed. Improving the resolution is harder, since it is impossible to do by considering one event at a time. Instead it would be necessary to re-weight events or perform some other operation which affects the whole distribution in order to get a measured mass distribution with an effective resolution which is narrower. Therefore, the resolution is modelled in such a way as to intentionally underestimate the Gaussian width of the resolution in the simulation; in order to get the correct resolution a smearing correction is applied. This correction is determined by comparing the reconstructed mass distribution of the Z^0 in data and simulation [61, 64]. The official `EnergyRescaler` tool* was used to apply the correction for this analysis. In addition to correcting the simulated energy,

*Internal Reference:
https://twiki.cern.ch/twiki/bin/viewauth/AtlasProtected/EnergyRescaler

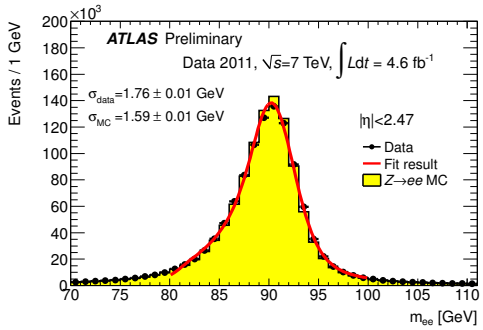

Figure 6.7: Reconstructed $Z \rightarrow e^+e^-$ peak in simulation and data after applying the `EnergyRescaler` tool.

the `EnergyRescaler` is also used to do a final stage scale calibration to the data which is tuned to give good agreement in the reconstructed $Z \rightarrow e^+e^-$ mass peak as shown in figure 6.7.

The discriminating variables which are used for photon identification (discussed in section 6.3) are imperfectly modelled in the simulation. The `FudgeMCTool` [†] is used to improve agreement between the data and simulation [62].

Isolation is corrected using the official `CaloIsolationCorrection`[‡] tool in both data and simulation to account for a dependence on the ambient energy density due to pile-up and the light leakage between cells in the calorimeter, which introduces a dependence on the energy of the photon [65].

[†]Internal Reference:
https://twiki.cern.ch/twiki/bin/viewauth/AtlasProtected/PhotonFudgeFactors

[‡]Internal Reference:
https://twiki.cern.ch/twiki/bin/viewauth/AtlasProtected/CaloIsolationCorrections

Chapter 7

Event Selection

Not everything that can be counted counts;

and not everything that counts can be counted.

ALBERT EINSTEIN

This chapter describes the selection used to choose events which enter into this analysis. The purpose of the event selection is to keep as many diphoton events from hypothetical graviton decay as possible, whilst rejecting background events.

7.1 Event selection criteria

As discussed in section 4.3, events in this analysis must first be present in the good run list*, to ensure that relevant pieces of the detector are at nominal running conditions. The online trigger (`EF_2g20_loose`) is used to require two photon-like objects, as determined through loose cuts on the discriminating variables (*c.f.* section 6.3). The turn on curve for this trigger is away from the region of interest for the analysis (*c.f.* figure 8.12). For an event to be considered, it must contain a vertex with at least 3 tracks in order to veto non-collision events originating from single particles which can potentially fake a two-track signal. Real proton collisions always contain more activity. In addition to the basic selection, Monte Carlo samples have additional corrections applied to improve agreement with the data. Kinematic cuts are applied on their true properties in order to eliminate sample overlap.

Once the above event selection is applied, the photon objects are individually inspected in more detail and removed from consideration from the event if they fail any part of the selection. If there remain two or more photons at the end of these selections, these are considered candidate events for the process $G \rightarrow \gamma\gamma$. The selection requirements for photons are:

*Internally named "`PHYS_CombinedPerf_Egamma_Eg_standard`".

- A corrected $p_{\mathrm{T}} > 25\,\mathrm{GeV}$, in order to get above the trigger efficiency turn-on curve, which is shown in figure 7.1.

- $\left|\eta\right| < 2.37$ as measured in the second sampling and not in the "*crack*" region $1.37 < \left|\eta\right| < 1.52$,

- As per the official recommendations, objects are removed which have a bad Liquid Argon Quality flag in conjunction with values of middle layer discriminating variables $R_\eta > 0.98$ and $R_\phi > 1$ and time measured in highest energy cell in second sampling layer associated with the e-gamma cluster $> 10\,\mathrm{ns}$. With the exception of the R_η and R_ϕ variables, these cuts are performed by selecting bits from a bitmap computed upstream[†].

- Tight cuts on the discriminating variables (see section 6.3)

- Isolation energy $< 5\,\mathrm{GeV}$ measured in a cone with solid angle 0.4 with corrections applied to account for pile-up and light leakage into adjacent calorimeter cells.

Events are removed from consideration if they are a dilepton candidate, as identified by {run, event number} provided to the author to remove $G \to e^+e^-$ candidates to avoid double counting in the combination analysis, using the selection described in [66]. This affects less than 0.05% of events and was performed to ensure that the two searches were orthogonal and allow a later combination of the searches.

The invariant mass $m_{\gamma\gamma}$ is reconstructed from the four-vectors of the top two photons in p_{T}. It is assumed that a the p_{T} of the third photon be too low to enter the selection.

[†]Internal Reference:
https://twiki.cern.ch/twiki/bin/viewauth/AtlasProtected/LArCleaningAndObjectQuality

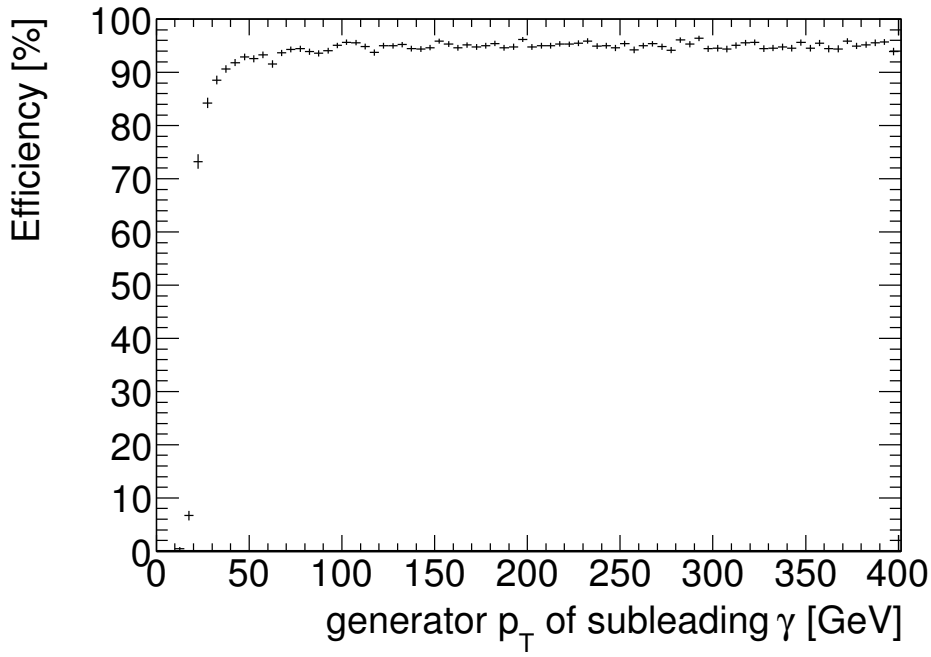

Figure 7.1: Trigger efficiency turn-on curve for the `EF_2g20_loose` trigger as a function of the true p_{T} of the sub-leading photon. There is a sharp rise at approximately 25 GeV and a plateau to an efficiency of approximately 95%. This curve is computed using forward truth matching (see section 5.3). To separate the effects of acceptence and the single photon trigger, events are considered in the denominator of the efficiency if the two generated photons are inside the fiducal volume of the inner detector $\left|\eta\right| < 2.5$ and the true leading photon has a $p_{\mathrm{T}} > 30\,\mathrm{GeV}$.

These four-vectors are corrected so that the η of each photon points back to the location of the interaction vertex of the event along the longitudinal axis, rather than the centre of the detector.

Chapter 8

Background Determination and Signal Modelling

The event selection discussed in the previous chapter determines the set of events which will be fed into the limit setting procedure. Before limit setting can proceed, it is necessary to determine the quantity of background events in the region of interest and its shape in the invariant mass distribution, so that they can be correctly accounted for in the limit. Section 8.1 introduces the different classes of background. In section 8.2 the composition of the background is determined from data. Section 8.3 determines the shapes of the different classes of background, which are then added together according to the background composition determined from data.

8.1 Background composition

As discussed previously, the primary background to prompt diphoton production comes from events where one or more jets (j) have a signal in the detector which is indistinguishable from that of a true photon (γ). These are referred to as "*fake photons*". The measured diphoton spectrum is therefore composed of four categories of event labelled $\gamma\gamma$, γj, $j\gamma$ and jj where the first symbol represents the highest p_{T} object and the latter represents the second highest. The $\gamma\gamma$ component is called the irreducible background (see section 8.1.1), as there exists no physical measurement which can differentiate it from signal. The other three categories of event are referred to as the reducible background (discussed in section 8.1.2) and have one or more jets which are misidentified as a photon. These events may or may not be distinguishable from $\gamma\gamma$ using cuts on the physical properties of the events.

The relative rates of each of the four components is unknown *a priori*. Estimates from

simulation are difficult to obtain because the fake rate is low but the absolute rate of jet events is high. In addition it is known that the simulation is poor at estimating the cross-section for such events. Therefore, it is necessary to estimate it from the data. The fraction of $\gamma\gamma$ events out of the total passing the selection cuts is called the purity.

Non-collision backgrounds such as events arising from beam-halo interactions and cosmic rays are negligible due to the requirement that the event have a primary vertex near the beam spot with three or more tracks.

8.1.1 Irreducible background

The irreducible component, $\gamma\gamma$, is simulated using PYTHIA 6 and run through the full detector simulation as discussed in chapter 5. It is re-weighted so that the shape of the true $m_{\gamma\gamma}$ distribution agrees with the distribution predicted by the DIPHOX next-to-leading order generator. Parton density functions were chosen according to the recommendations in [67], using the `MSTW2008NLO` PDF set primarily and using the `CTEQ6.6` and `MRST2007LOMOD` sets to derive a systematic uncertainty. The weights applied vary as a function of mass. Due to low statistics in the distributions used to compute the weight at high mass, the weight is set to 1 above 1.3 TeV. In order to take into account the systematic uncertainty arising from the choice of PDF sets and isolation cuts, DIPHOX was re-run in multiple configurations. The resulting weight (the so-called "k-factor") and its uncertainty is summarised as shown in figure 8.1.

In order to have sufficient statistics in the tail of the $m_{\gamma\gamma}$ distribution, the channel is generated in four separate samples corresponding to different mass regions, shown in table 5.1. A cut is applied on the generated mass so that the samples do not overlap. The

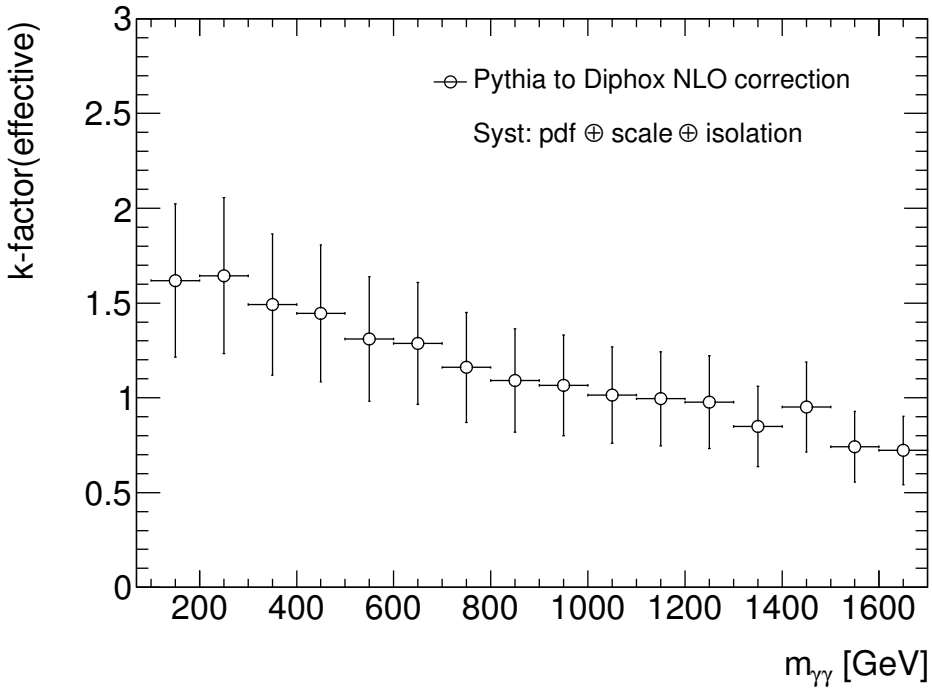

Figure 8.1: k-factor applied to the PYTHIA 6 simulated irreducible background in order to reproduce the invariant mass distribution predicted by DIPHOX [68]. The uncertainties shown take into account changes in the distribution by varying the isolation cut, varying the PDF eigenvectors used and by varying non-physical scale factors, see section 9.1.1 for more detail.

samples are weighted according to their relative cross-sections and then to the luminosity in the data to give a continuous distribution in the true $m_{\gamma\gamma}$.

8.1.2 Reducible background

The reducible background comes from events where one or more of the measured photon objects have arisen from a physics jet, and consists of three components: γj, $j\gamma$ and jj. This background is heavily selected against by the photon identification discussed

in chapter 6. However, the tight selection still contains an unknown number of events originating from the reducible background. Their effect on the $m_{\gamma\gamma}$ distribution and its uncertainty must be measured from the data. In order that this can be properly taken into account by the limit setting procedure, it is necessary to extract an estimate of the $m_{\gamma\gamma}$ distribution for the reducible background. This process requires a measurement of the shape of the distribution of each of the separate irreducible components (γj, $j\gamma$ and jj) along with their relative yields.

8.2 Yield estimation

To obtain an estimate of the reducible background present in the "tight and isolated" selection a so-called "*template fitting*" procedure is used. This proceeds by estimating the probability density functions (in this section referred to as PDFs, not to be confused with parton density functions) for the photon and jet calorimetric isolation ($P_\gamma\left(E_{\text{iso}}\right)$ and $P_j\left(E_{\text{iso}}\right)$ respectively) from the data using a sample of events independent from the final selection. The leading and sub-leading (in p_{T}) photon object PDFs are treated independently and are therefore labelled P_X^1 and P_X^2 respectively, where X is γ or j. The PDF estimation will be described in the subsequent section.

Given these PDFs a 2-dimensional fit in the leading and sub-leading photon object's isolation (E_{iso}^1 and E_{iso}^2 respectively) is performed against the number of events measured in the tight selection $\left(N_{\text{total}}\left(E_{\text{iso}}^1, E_{\text{iso}}^2\right)\right)$ to extract the yields $N_{\gamma\gamma}$, $N_{\gamma j}$, $N_{j\gamma}$ and N_{jj}:

$$
\begin{aligned}
N_{\text{total}}\left(E^1_{\text{iso}}, E^2_{\text{iso}}\right) &= N_{\gamma\gamma} \cdot P^1_\gamma\left(E^1_{\text{iso}}\right) P^2_\gamma\left(E^2_{\text{iso}}\right) \\
&+ N_{\gamma j} \cdot P^1_\gamma\left(E^1_{\text{iso}}\right) P^2_j\left(E^2_{\text{iso}}\right) \\
&+ N_{j\gamma} \cdot P^1_j\left(E^1_{\text{iso}}\right) P^2_\gamma\left(E^2_{\text{iso}}\right) \\
&+ N_{jj} \cdot P_{jj}\left(E^1_{\text{iso}}, E^2_{\text{iso}}\right). \qquad (8.1)
\end{aligned}
$$

To cope with correlation between the jet-jet background, the P_{jj} template is taken directly from the data and interpolated using a `RooKeysPDF` which is described in [69].

8.2.1 Background and signal PDF estimation

The jet isolation distribution $P_j\left(E_{\text{iso}}\right)$ is estimated by obtaining a sample of background-enriched events referred to as the "*anti-tight*" selection. Some of the identification cuts discussed in section 6.3 are inverted in order to obtain a sample of physics objects which fail the tight selection but are otherwise similar to a true photon signal. At this stage the leading and sub-leading photons are treated independently with no requirement on the other photon of the pair; this is done to maximize the statistics.

The selections which are inverted are shown in table 8.1. This anti-tight sample is dominated by background events with "signal-like" properties. The isolation distribution for these events is shown in figure 8.2. The isolation distribution for the anti-tight objects are fitted using RooFit [70] with a Novosibirsk function* to obtain an approximate

*"The Novosibirsk function is usually defined by:

$$f(x) = A_S \exp(-0.5 \times \left(\ln^2[1 + \Lambda\tau \cdot (x - x_0)]/\tau^2 + \tau^2\right)),$$

N	Inverted cuts
2	w_{s3}, F_{side}
3	w_{s3}, F_{side}, ΔE
(nominal selection) 4	w_{s3}, F_{side}, ΔE, E_{ratio}
5	w_{s3}, F_{side}, ΔE, E_{ratio}, ΔE_{max2}

Table 8.1: Definition of the anti-tight cuts and their systematic variations. The nominal anti-tight selection uses 4 reversed cuts. The other inverted cuts are used to evaluate the systematic uncertainty of the method.

analytic PDF for $P_j\left(E_{\text{iso}}\right)$ of background-like objects, which is is overlaid in figure 8.2.

The signal PDFs P_γ^1 and P_γ^2 are obtained by subtracting an estimate of the background from the tight photon's distribution. The background is determined by scaling P_j obtained from the Novosibirsk fit to match the number of events in the tail of the tight isolation distribution where it is known to be dominated by background. The resulting values are then fitted with a Crystal Ball function [72] to obtain P_γ, which is shown in figure 8.3.

These distributions are then used as input to an extended maximum likelihood fit to the two dimensional calorimetric distribution of the final selection in 8.1.

8.2.2 Results of yield estimation

The photon and jet PDFs (determined in section 8.3) are used to determine the relative fractions of the four background components in the signal (isolated) region. Figure 8.4 shows the projections of the the four components coming from the 2D fit along with the total. Table 8.2 shows the relative number of events of each type present in the signal region by integrating over signal region of the two-dimensional templates. The measured

where $\Lambda = \sinh(\tau\sqrt{\ln 4})/(\sigma\tau\sqrt{\ln 4})$, the peak position is x_0, the width is σ, and τ is the tail parameter." [71].

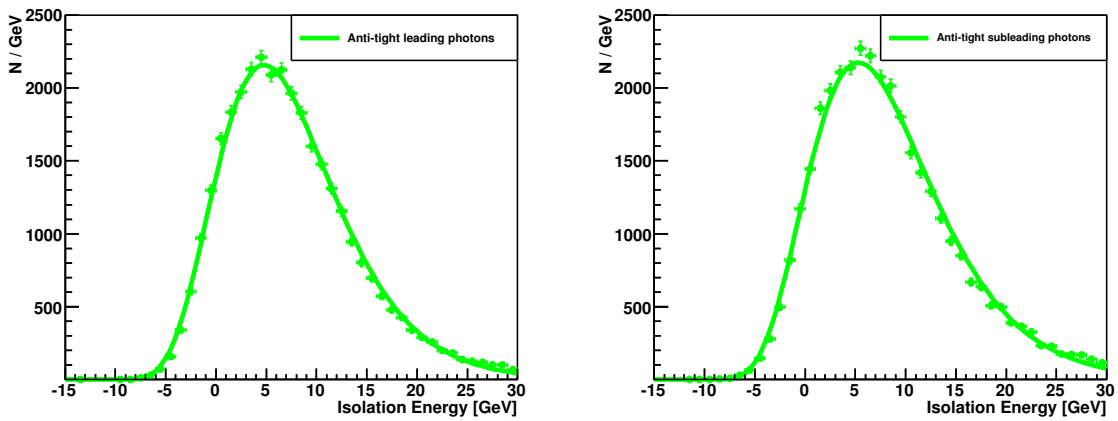

Figure 8.2: Isolation for the leading (left) and sub-leading (right) objects in the photon container which have failed the tight selection but pass the anti-tight selection. The continuous PDF is obtained by fitting a Novosibirsk function with RooFit. The isolation is a sum of energies over cells, each of which have an amount of noise present in them. Since the measured energy is corrected by subtracting the mean amount of noise in that cell, the energies can be negative.

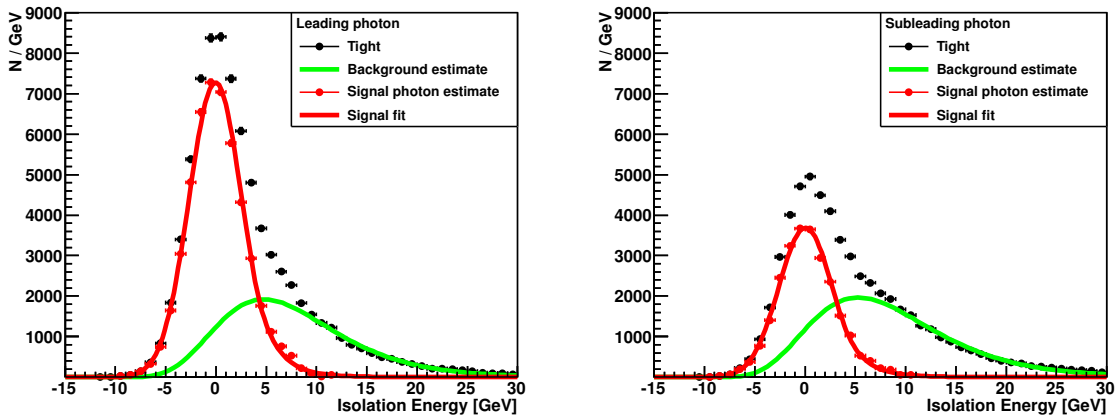

Figure 8.3: Extraction of the signal isolation PDF and the resulting fit to a crystal ball function.

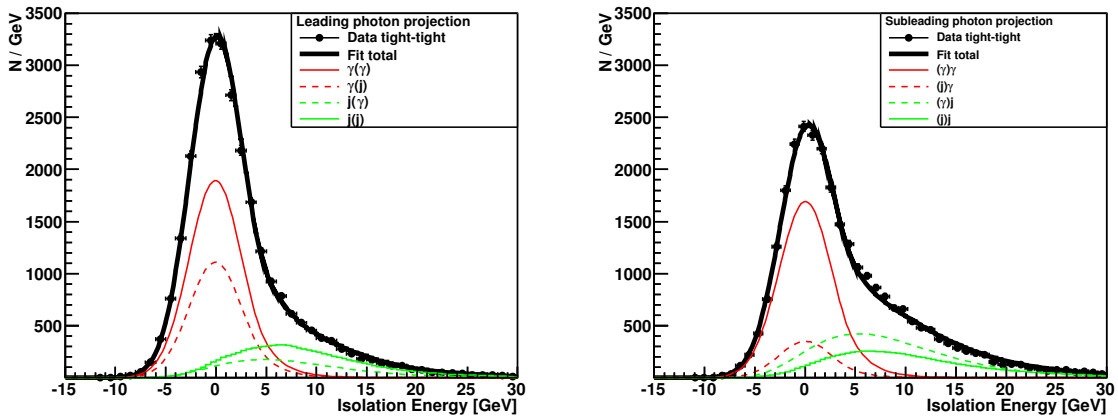

Figure 8.4: Projections of the 2D template fit onto the isolation of the leading and subleading photon object.

N Cuts	$\%_{\gamma\gamma}$	$\%_{\gamma j}$	$\%_{j\gamma}$	$\%_{jj}$
2	66.3 ± 0.4	20.9 ± 0.3	8.7 ± 0.3	4.1 ± 0.2
3	70.2 ± 0.4	18.6 ± 0.3	7.4 ± 0.2	3.8 ± 0.2
4 (Nominal)	73.4 ± 0.3	16.5 ± 0.3	6.5 ± 0.2	3.7 ± 0.2
5	77.5 ± 0.3	13.8 ± 0.2	5.2 ± 0.2	3.5 ± 0.2

Table 8.2: Results of the 2D template fitting procedure, showing the relative fractions of each component of the background as a percentage for four variations of the definition of the anti-tight selection.

purity of the nominal cuts is $(73.4 \pm 0.3)\%$. In order to evaluate the uncertainty on the method due to the arbitrary choice of which cuts are reversed, three other sets of cuts are tried. The systematic uncertainty on the purity is taken to be one half of the extent of the measured purities over the different choice of cuts: $77.5\% - 66.3\%$, which is approximately 5%, *i.e*, the purity is approximately $\left(73.4 \pm 0.3\ (\text{stat}) \pm 5\ \left(\text{syst}\right)\right)\%$. The systematic impact of this on the total background estimate is discussed in section 9.1.

8.3 Background modelling

The shapes of the three reducible components of the background are each independently extracted by fitting them with a power law distribution:

$$\frac{\mathrm{d}N}{\mathrm{d}m_{\gamma\gamma}}\left(m_{\gamma\gamma}\right) = m_{\gamma\gamma}^{\left(k_1 + k_2 \ln m_{\gamma\gamma}\right)},$$

which provides a reasonable modelling of the shape as predicted by DIPHOX and is motivated by the fact that propagators are power law distributions. The result of these fits is shown in figure 8.5. These three are then summed along with the irreducible component described in section 8.1.1 in proportion to the yields obtained in section 8.2.2 to give an estimate of the background distribution. This is scaled to the data in the control region $140 < m_{\gamma\gamma}/\mathrm{GeV} < 400$. The resulting total background estimate is shown in figure 8.6. The total uncertainty shown in this figure takes into account the systematic uncertainty on the irreducible background, correlations between the fitted yields from section 8.2.2, as well as the uncertainty bands on the fitted reducible background estimate. The background estimate in the signal region is shown with the distribution obtained from data in figure 8.7 on a linear scale. Figure 8.8 shows several resonances with varying m_G superimposed on the background distribution, along with the data; figure 8.9 shows the same but with varying $k/\overline{M_{\mathrm{pl}}}$.

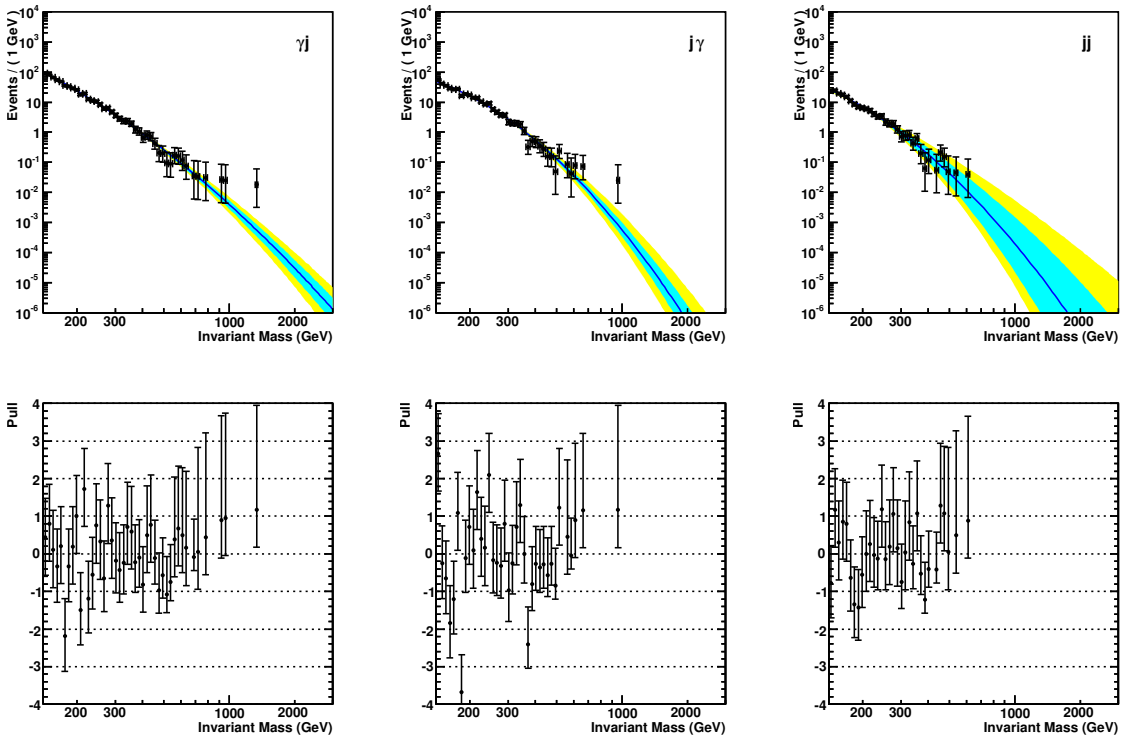

Figure 8.5: (Above) Fits to the different components of the irreducible background, showing the $\pm 1\sigma$ and $\pm 2\sigma$ uncertainty bands, taking into account the correlations between the fit parameters. (Below) Pull values to the fit respectively.

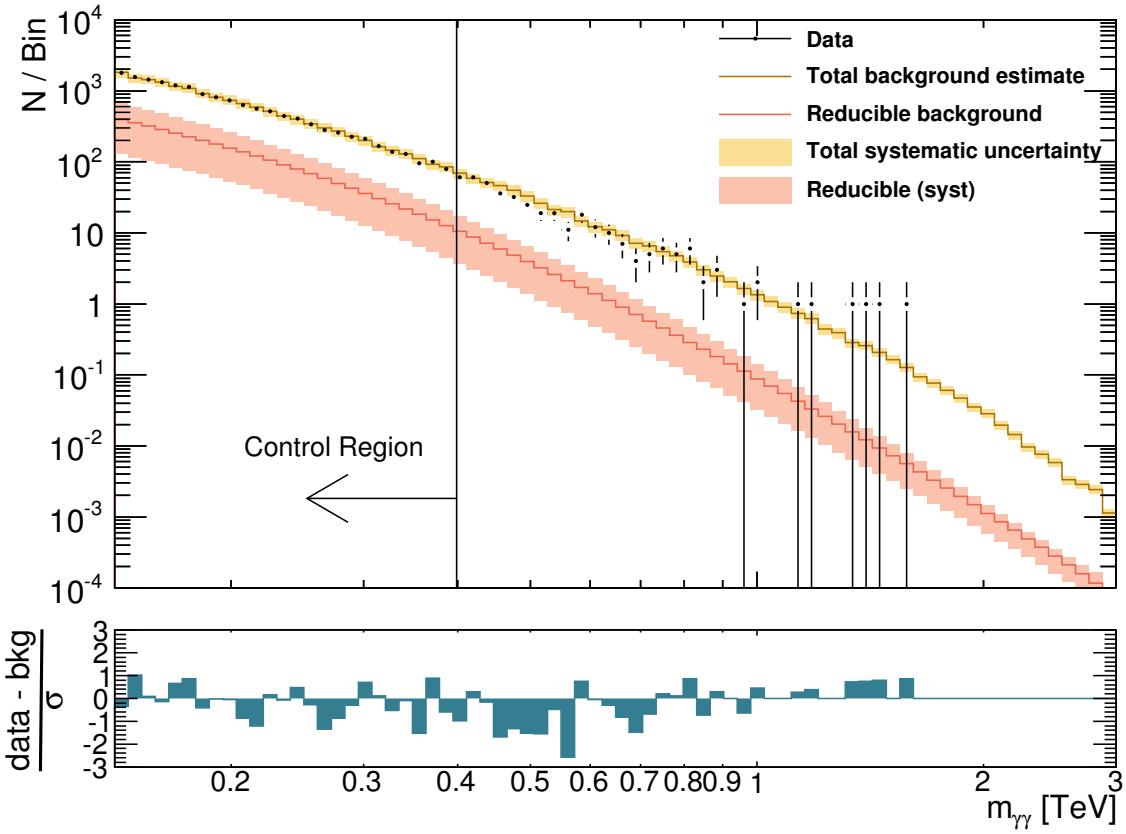

Figure 8.6: Total background estimate of the mass distribution, which is the sum of the reducible and irreducible backgrounds, overlaid by the data. The lower plot shows the significance, defined as the magnitude of the difference between the prediction and the data in units of the $\sqrt{N}$ on the data. The true significance is reduced as there is a non-negligible systematic uncertainty on the total estimate.

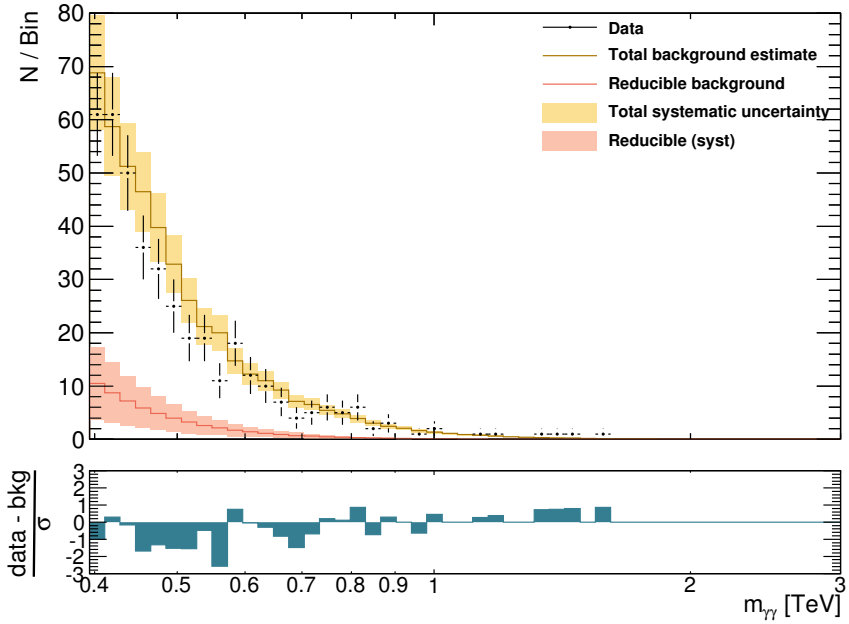

Figure 8.7: Background estimate in the signal region on a linear scale.

8.4 Signal modelling

The signal templates used for the limit setting in the following chapter are derived from the graviton template sample described in section 5.4. Two-hundred templates are used which are spaced logarithmically in m_{G} between 400 GeV and 3 TeV. Example templates are shown for gravitons with a $k/\overline{M}_{\mathrm{pl}} = 0.1$ at masses of 0.8, 1, 1.25, 1.5 and 2.2 TeV normalized to the PYTHIA 8 cross-sections obtained in section 2.5.

8.4.1 Invariant mass resolution

Figure 8.10a shows the evolution of the detector resolution of $m_{\gamma\gamma}$ with $m_{\gamma\gamma}$, which tends towards approximately 1% of $m_{\gamma\gamma}$ at high mass. The Gaussian resolution is measured

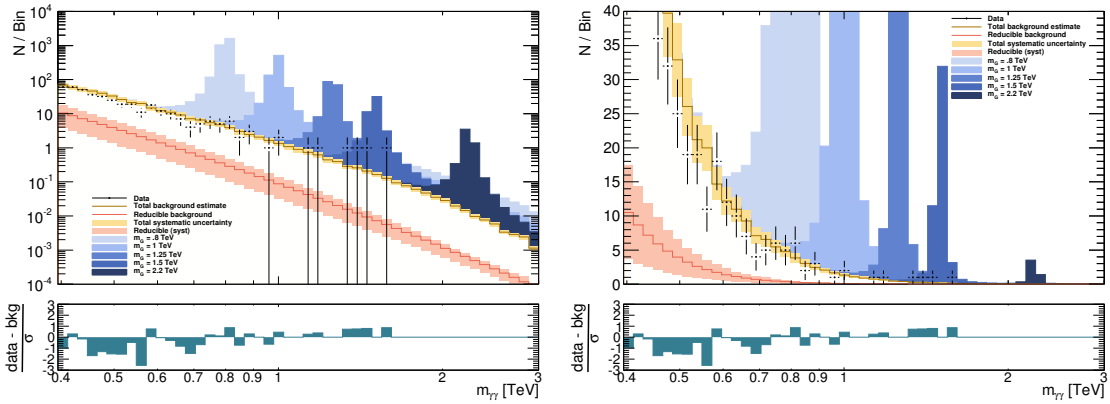

Figure 8.8: Signal region of the $m_{\gamma\gamma}$ distribution showing multiple example resonances at different masses with $k/\overline{M}_{\mathrm{pl}} = 0.1$. Superimposed are the reducible background prediction, total background prediction and the measured data. Both plots show the same information, the left plot is on a logarithmic scale.

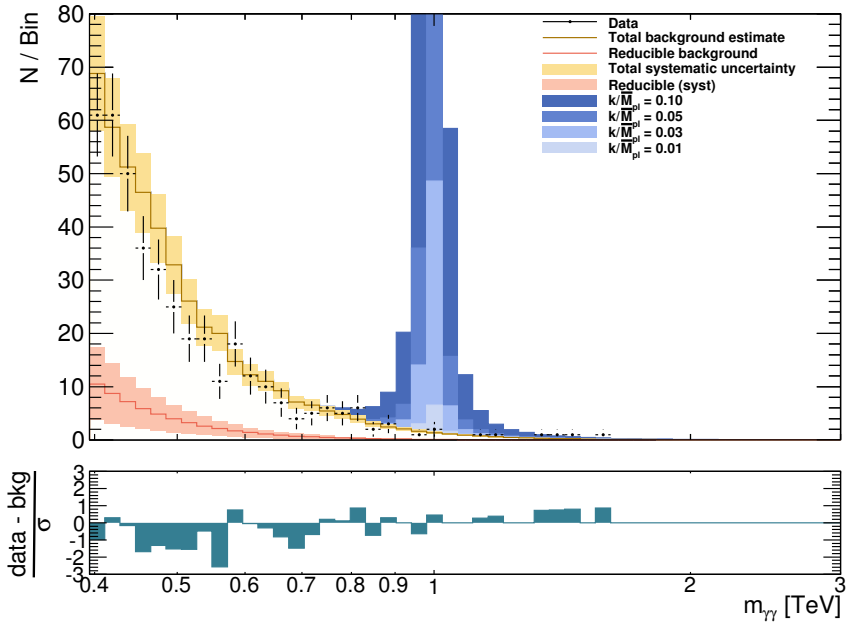

Figure 8.9: Similar in spirit to figure 8.8, this plot shows the evolution of the width and cross-section of resonances with an $m_{\mathrm{G}} = 1\,\mathrm{TeV}$ and $k/\overline{M}_{\mathrm{pl}} = \{.1, .05, .03\,.01\}$.

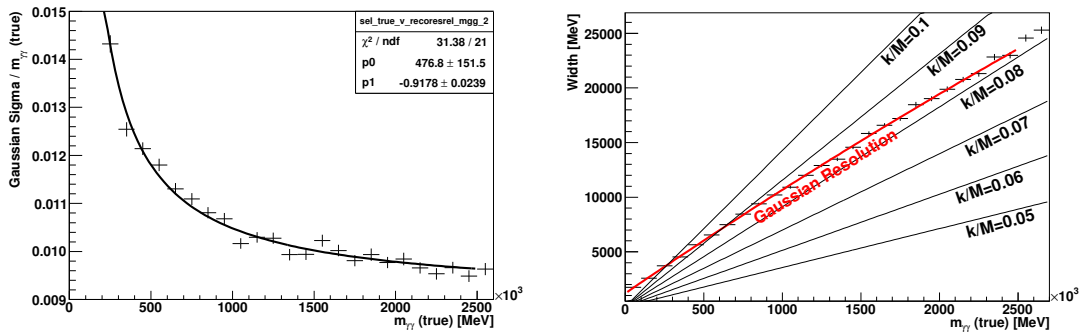

(a) (b)

Figure 8.10: Comparing the detector resolution to the resonance widths. (a) Shows the fractional Gaussian resolution of the $m_{\gamma\gamma}$ reconstruction determined from the template graviton sample discussed in section 5.4. (b) Compares the Gaussian detector resolution against the widths of gravitons with various values of $k/\overline{M_{\mathrm{pl}}}$. The line marked "Gaussian Resolution" effectively shows the minimum width of a reconstructed resonance.

by fitting the reconstructed mass minus the true mass in the graviton template sample with a Voigt profile [73]. The Voigt profile represents the convolution of a Breit Wigner distribution with a Gaussian distribution. The Gaussian term from the Voigt fit on the resolution is compared with the Breit-Wigner width of gravitons with different values of the coupling parameter $k/\overline{M_{\mathrm{pl}}}$ in figure 8.10b. It can be seen that the width of measured resonances will be dominated by the detector resolution for most of the m_G-$k/\overline{M_{\mathrm{pl}}}$ limit plane. This is summarised in figure 8.11.

8.4.2 Signal efficiency

The signal efficiency was evaluated with the graviton template sample (see section 5.4) using forward truth matching as described in section 5.3. The trigger efficiency (for `EF_2g20_loose`) as a function of the true graviton mass is shown in figure 8.12, which is

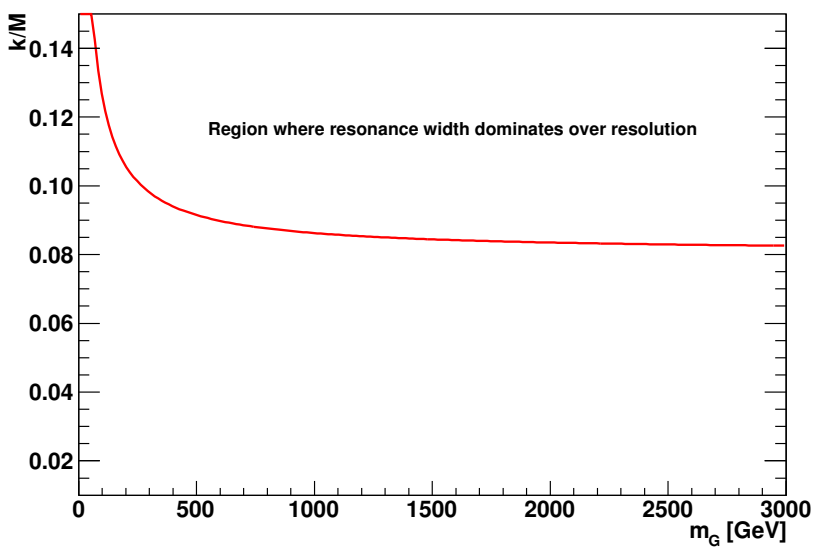

Figure 8.11: Summary of the region of the $m_{\mathrm{G}} - k/\overline{M_{\mathrm{pl}}}$ plane where the contribution to the measured width of the resonance from the resonance width is larger than that from the detector resolution.

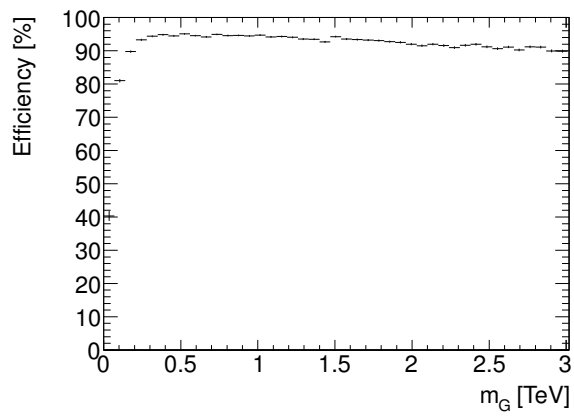

Figure 8.12: Trigger efficiency (for `EF_2g20_loose`) as a function of the true graviton mass, m_G, computed with the same fiducial requirements as figure 7.1.

computed in such a way as to eliminate the effects of the single photon trigger efficiency and acceptance of the detector. It rises sharply at approximately $m_G > 100\,\text{GeV}$ and plateaus at an efficiency of approximately 95%. There is a slight drop in the efficiency to very high masses owing to the fact that photons with very high transverse energy will potentially punch through the electromagnetic calorimeter and fail the hadronic energy ratio cut on R_{had}.

The total efficiency is shown as a function of m_G in figure 8.13. The numerator considers gravitons whose decay products are reconstructed and pass all of the selection criteria discussed in section 7.1. The denominator is all graviton events generated by the physics simulation, including those which are not in the acceptance of the detector. To parametrize the signal efficiency, it is fitted over the range $400 < m_{\gamma\gamma}/\text{GeV} < 4000$ with a 6th-order polynomial, whose coefficients are also shown in figure 8.13. This parametrization is used in section 11.2 to determine the cross-section limit.

Differences between data and simulation will be described in Chapter 9.

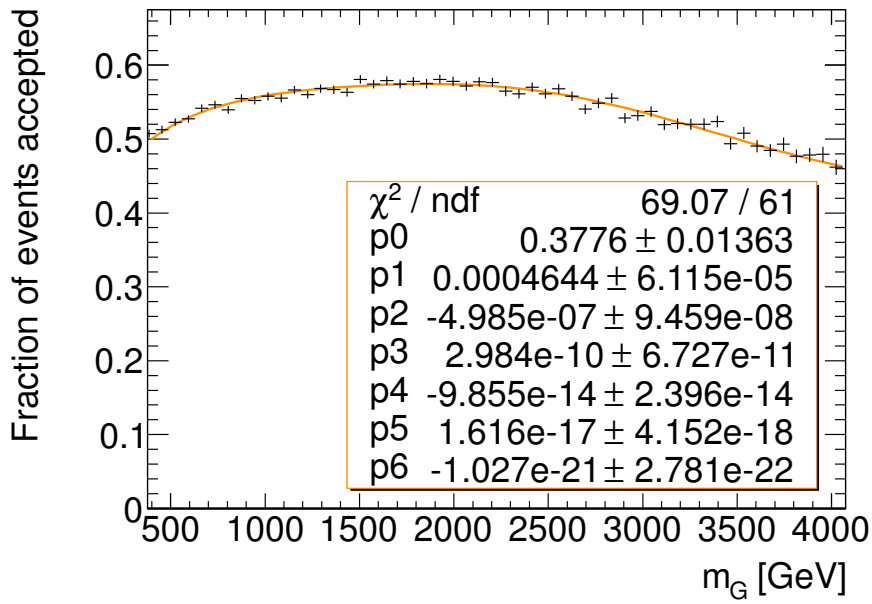

Figure 8.13: Measured signal efficiency times acceptance as a function of m_G with 6-order polynomial fitted using a least-squares fit. The coefficients of the polynomial obtained from the fit are shown on the plot along with the χ^2 per degree of freedom. The numerator counts all events where the graviton is correctly reconstructed and passes all analysis cuts and the denominator counts all graviton events generated, even those outside the detector acceptance.

Chapter 9

Systematic Effects

Before a measurement can be quoted, it is necessary to take into account any effects which may have an impact on the final result. Such effects might be due to imperfect knowledge of the detector, or arise from assumptions made about how the physics or detector behave. These are referred to as systematic uncertainties, as the uncertainties arising from these effects are not independent between events, potentially leading to a systematic bias.

The systematic uncertainties that need to be considered are those which affect the expected background or those which have an impact on the signal. The former will affect the measured limit in terms of numbers of events; the latter will impact how this limit translates a constraint on the theoretical model.

9.1 Background estimate

This section discusses an estimate of the systematic uncertainty on the total background estimate and how it is derived for the reducible and irreducible backgrounds. The contribution to the background from non-collision sources such as beam halo and cosmic rays are believed to be entirely suppressed by the coincidence in timing required during data acquisition and the requirement that the event have a suitable primary vertex and are therefore neglected.

9.1.1 Irreducible background estimate

The most significant systematic uncertainty on the total background comes from the irreducible template derived from the PYTHIA sample which is re-weighted to the DIPHOX

prediction, as discussed in section 8.1.1.

The uncertainty coming from the DIPHOX shape prediction is estimated by comparing the $m_{\gamma\gamma}$ distribution in different scenarios (for example, varying the scale or the PDF sets used) and in each case normalizing the templates to the unmodified distribution in the region $140 - 3000\,\text{GeV}$ and taking the absolute value of the difference in each bin. The following four assumptions which impact the $m_{\gamma\gamma}$ distribution are varied to obtain these differences, which are added in quadrature to obtain the total uncertainty:

Scale

There are three non-physical scales in the DIPHOX simulation which affect the cross-section through their impact on α_s: The re-normalization scale, the initial factorization scale and the final factorization scale. It is desirable to choose values of these scales where the cross-section's dependence on them is minimizedand therefore these scales are set to $m_{\gamma\gamma}$. To compute the uncertainty each scale is varied by a factor of two. In addition, sensitivity to these parameters was checked by coherently varying all possible pairs of parameters whilst holding the other parameter in the triplet constant.

Isolation

In the Diphox generation, an isolation of $E_{\mathrm{T}}^{\mathrm{iso}} > 7\,\text{GeV}$ is used. To demonstrate that this choice does not have a significant impact on the result, the isolation cut is moved down by $2\,\text{GeV}$ and up by $8\,\text{GeV}$.

MCFM

An alternative generator to DIPHOX, MCFM [74, 75] is a parton-level NLO Monte

Carlo generator. The main difference between DIPHOX and MCFM is that the box diagram (figure 2.8) is also included at NNLO in MCFM. Good agreement was observed with the DIPHOX predictions.

PDF sets

Alternative PDF sets are substituted as discussed in section 8.1.1.

Figure 9.1 shows the estimated fractional systematic uncertainty on the shape of irreducible background as a function of $m_{\gamma\gamma}$. The dominant component of the uncertainty on the irreducible background comes from the variation in the choice of PDF sets used, which has an uncertainty of 5% at 500 GeV increasing to 28% at 3 TeV. The other systematic uncertainties rise in the normalization region and flatten out at a value of up to 5%. The total uncertainty on the irreducible background varies from 10% at 500 GeV increasing to 30% at 3 TeV.

9.1.2 Reducible background estimate

The uncertainty from the reducible background estimate is obtained by considering the uncertainties on the yield estimates for the three components of the reducible background along with the fit uncertainty arising from the $m_{\gamma\gamma}$ fit to the power law distribution described in section 8.3. The error bands in figure 8.5, which propagated into the total reducible background estimate, are computed using ROOFIT [70] and take into account the correlations between the fit parameters.

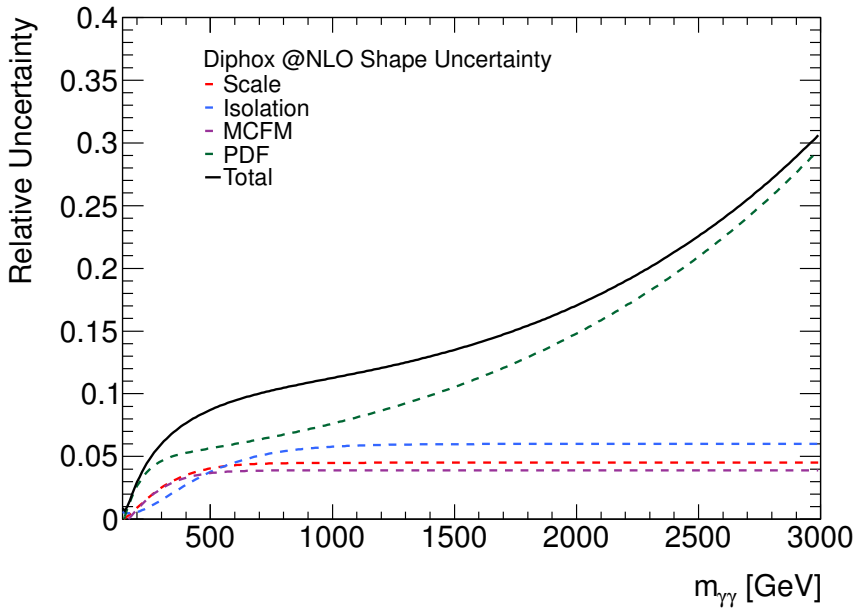

Figure 9.1: Systematic uncertainty estimate on the irreducible background, showing the four components (Scale, Isolation, MCFM and PDF) contributing the the total systematic uncertainty which is the sum in quadrature of the individual components [68].

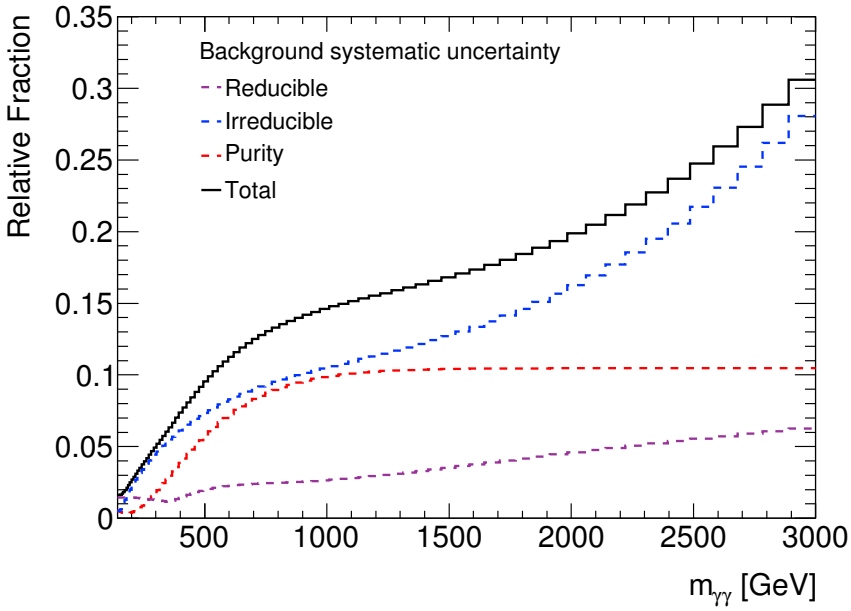

Figure 9.2: Total background systematic uncertainty estimate [76], showing the origin of the individual components contributing to the total.

9.1.3 Total background estimate

The systematic uncertainty on the total background is shown as a fraction of the total background estimate in figure 9.2. It varies from approximately 1% at low masses up to 30% at 3 TeV. The dominant uncertainty comes from the irreducible background as it is the most significant contributor to the total $m_{\gamma\gamma}$ distribution. In addition to the uncertainties derived from the reducible and irreducible background components, the uncertainty labelled "purity" in figure 9.2 comes from the variation of the yield estimation method by using alternative cuts as described in section 8.2.2.

9.2 Uncertainties on the signal

To estimate the effect on the model limits of systematic uncertainties on the signal it is necessary to consider matters which may affect a) the efficiency of recording signal events b) the theoretically predicted number of events (through the cross-section) and c) the luminosity. All of which are propagated into the final uncertainty on the limit through the effective uncertainty on the signal efficiency. The systematic effects considered to impact the effective signal efficiency are:

Pile-up

The impact of the pile-up on the systematic uncertainty of the efficiency was estimated in simulation by measuring the difference in efficiency as a function of $\langle\mu\rangle$ and was found to be negligible.

Integrated Luminosity

The integrated luminosity was determined to be $4.91\,\text{fb}^{-1} \pm 1.8\%$ as described in [33].

Photon Trigger

The systematic uncertainty arising from the trigger efficiency is the difference between the efficiency as estimated in the simulation and the data for events passing the analysis selection. The efficiency in the data is estimated using a "*bootstrap*" technique to measure the single-photon trigger efficiency which is then squared to obtain the two-photon trigger efficiency. The single-photon trigger efficiency is computed as the product of the efficiencies in the trigger chain, which are estimated with respect to tight+isolated photons in the minimum bias stream. The difference between simulation and data is found to be on the order of 2%.

Photon Efficiency and Identification

The systematic uncertainty on the identification efficiency was estimated by using three independent data driven methods and comparing the results. These methods include using photons from radiative $Z \rightarrow 2$ lepton decays, extrapolating the shower shape variables from $Z \rightarrow e^+e^-$ decays, and a matrix method using different parts of the EM calorimeter and relaxed tight cuts akin to those used to obtain the reducible background estimate in chapter 8.2.1. These methods are described in more detail in [77, 62]. It was found that the efficiency agreed with the simulation to within 5%, and this value is used as the systematic uncertainty.

PDF Uncertainty

Using the `MSTW2008lo90cl` PDF set, each of 20 eigenvalues were varied by $\pm 1\sigma$ and the total uncertainty was obtained by taking the sum in quadrature of the negative and positive variations separately. The uncertainty was found to vary from $\sim 5\%$ at 300 GeV up to 10% at 500 GeV. To be conservative the value of 10% is used across the whole range [76].

***k*-factor**

An NLO k-factor of 1.75 ± 0.1 [76] is provided by the authors of [18].

These uncertainties are summarised in table 9.1. It is assumed that they are uncorrelated and all are summed in quadrature to provide a final estimate of the systematic uncertainty of 13%.

Effect	Estimated magnitude of effect (%)
Integrated Luminosity	1.8 [33]
Photon Trigger	2.0
Isolation	2.0 [62]
Photon Efficiency and ID	5 [62]
k-factor	5.7
PDF	10 [76]
Total	13

Table 9.1: Estimate of systematic uncertainties on the signal. The total is the sum in quadrature of the individual components.

Chapter 10

Statistical Procedures and Limit Setting

If the matter is one that can be settled by observation, make the observation yourself. Aristotle could have avoided the mistake of thinking that women have fewer teeth than men, by the simple device of asking Mrs. Aristotle to keep her mouth open while he counted.

BERTRAND RUSSELL

This chapter covers the derivation of the main result of this thesis, which is presented as a 95% upper limit on the cross-section times branching ratio (σB) for $G \rightarrow \gamma\gamma$ as a function of mass. The background and signal templates obtained in chapter 8 are used for this measurement. Initially, the measurement will be done in terms of the number of signal events N_{signal}, multiplied by the signal template present in the data distribution. Later, this will be scaled according to the luminosity and efficiency to restate the result in terms of cross-section times branching ratio (σB).

Before limit setting is discussed in section 10.2, a model-independent scan of the mass distribution in data was done in section 10.1 to search for any significant excess above the expected background in a model independent way.

10.1 Searching for a signal with BumpHunter

Searching for a possible, but unlikely signal in the data is fraught with the problem that an experimenter can choose many different ways of defining their search. For example, if the search is split into different bins or channels, the choice of bins and number of channels can affect the outcome of the search. If the number of bins or channels is large, it becomes likely that a locally significant excess occurs due to statistical fluctuations. This phenomena is known as the "*look elsewhere effect*" [78].

The "*global*" significance must therefore be the proper figure of merit used to evaluate any candidate excess. To calculate the global significance it is necessary to reduce the measured significance according to a "*trials factor*", the number of effective trials which have taken place. It is one of the reasons that in high energy physics the required local

significance of a signal before it will be accepted by the community as a discovery is as high as 5σ.

The BUMPHUNTER [79] is a statistical method for searching for significant excesses which takes into account the trials factor by construction. The BUMPHUNTER paper shows that the algorithm gives a correct significance using toy Monte Carlo experiments. For a given measured and predicted distribution, it defines a single numeric test statistic. The more significant an excess is present in the data, the larger the value of the statistic. The distribution of this test statistic across experiments is estimated by performing many pseudo-experiments where the background distribution fluctuates in each experiment according to Poisson statistics. The p-value of the BUMPHUNTER test statistic is then the percentage of pseudo-experiments which has a test statistic greater than the value measured in data. If this p-value is less than 0.05, then the data would be thought to contain a significant excess, otherwise we must accept the null hypothesis.

The BUMPHUNTER test statistic is itself derived from a p-value, not to be confused with "the p-value *of* the BUMPHUNTER test statistic". It is the negative logarithm of the p-value of the most significant excess present in the data. This is determined by comparing numbers of data events summed across adjacent bins (a "*window*") with those from the predicted background. In principle, this window is varied in size and placed at all possible locations in the data. In practice it is not necessary to try all locations and sizes. Instead the window size is varied from a single bin up to the half of the width of the data. In addition, not all window positions are tested. This is not necessary as it would entail testing very similar bumps at the expense of unnecessary time and CPU cycles [79]. Instead, adjacent windows are separated by half of the bin-width.

The p-value for a given window is defined as:

$$p = P\left(N_{\text{data}} \geq N_{\text{predicted}}\right) = 1 - \text{PoissonCDF}\left(N_{\text{data}} - 1, N_{\text{predicted}}\right),$$

where N_{data} and $N_{\text{predicted}}$ are the number of events inside the window measured in the data and predicted distributions respectively, $P\left(N_{\text{data}} \geq N_{\text{predicted}}\right)$ is the probability of obtaining a measured number of events N_{data} greater than $N_{\text{predicted}}$ when sampling from a Poisson distribution with a mean of $N_{\text{predicted}}$. PoissonCDF is known analytically and is the Poisson Cumulative Density Function with a mean of $N_{\text{predicted}}$. Finally, the BumpHunter test statistic is defined as the minimum of all of these p-values. The result of running the BumpHunter algorithm is presented in section 11.1 and the implementation used is provided in appendix A.

10.2 Limit definition

Given the absence of a signal, an upper limit measurement on $\sigma B\left(G \to \gamma\gamma\right)$ is performed as a function of the graviton mass m_G. The following description explains how the limit is computed for a single mass point. To measure the evolution of the limit with mass it is repeated with separate signal templates, $T_{i\left(\text{signal}\right)}$, at different mass points.

This analysis uses Bayesian statistics to determine an upper limit. The method was chosen so that the result would be compatible between experiments and search channels to enable a later combination of the results, increasing the sensitivity. The limit is first defined in terms of the number of signal events N_{signal} and later cast in terms of σB using the luminosity from section 5.1, signal efficiency from section 8.4.2 and Pythia 8

cross-sections discussed in section 2.5.

Neglecting systematic errors for the moment, the number of events measured in a single bin N is distributed over repeated trials according to the Poisson distribution:

$$P(N|\nu) = \frac{\nu^N}{N!}e^{-\nu} \qquad (\equiv \mathscr{L}(\nu; N)), \tag{10.1}$$

where N is the number of events measured in a given experiment and ν is the Poisson mean: the expected number of events in the bin. This can be thought of as "the probability to obtain the N from an experiment for a given ν". When this function is considered for a fixed value of the data, N, it is known as the likelihood, $\mathscr{L}(\nu; N)$.

For this analysis, there are two components to the Poisson mean ν:

$$\nu = \nu_{\text{background}} + \nu_{\text{signal}},$$

where ν_{signal} and $\nu_{\text{background}}$ are the expectation values coming from the signal and background templates respectively. $\nu_{\text{background}}$ is in principle fixed according to the background estimate and ν_{signal} is a floating parameter to be estimated.

Bayes' theorem can be used to determine the reverse of (10.1), $P(\nu|N)$, *i.e*, an estimate of the distribution of ν given N measured from the data:

$$P(\nu|N) = \frac{P(N|\nu)P(\nu)}{\int P(N|\nu)\,\mathrm{d}\nu}, \tag{10.2}$$

where $P(\nu)$ is called the prior probability distribution and $P(\nu|N)$ is the posterior distri-

bution. The 95% upper limit on ν_{signal} is then defined as $\nu_{\text{signal}}^{.95}$ where:

$$P\left(\nu \leq \nu_{\text{signal}}^{.95} | N\right) = \frac{\int^{\nu_{\text{signal}}^{.95}} P(\nu | N)\, \mathrm{d}\nu}{\int P(\nu | N)\, \mathrm{d}\nu} = 0.95.$$

The prior probability distribution $P(\nu)$ is chosen to be flat in the expected number of events up to an arbitrarily chosen maximum which is a large multiple of the expected background. It is not possible to compute (10.2) analytically, so it is computed numerically as discussed in section 10.3.

For multiple bins the same logic holds, except that $\mathscr{L}(\nu; N)$ is instead $\mathscr{L}(\boldsymbol{\nu}; \boldsymbol{N}) = \Pi_i^{N_{\text{bins}}} P\left(N_i | \nu_i\right)$ where N_i and ν_i are the number of data events and Poisson expectation respectively in the bin with index i. The Poisson mean of the signal component of ν_i is given by:

$$\nu_{i\,(\text{signal})} = N_{\text{signal}} \times T_{i\,(\text{signal})}, \tag{10.3}$$

where $T_{i\,(\text{signal})}$ is the bin value of the normalized signal template; similarly for the Poisson mean of the background component. Finally, N_{signal} is then the floating parameter with which the 95% upper limit is calculated as discussed in section 10.3.

10.2.1 Nuisance parameters and systematic uncertainty

To account for systematic uncertainties on the templates, the likelihood (10.1) is modified to introduce N_{syst} Gaussian distributed nuisance parameters $\boldsymbol{\theta}$, whose values are unknown:

$$\mathscr{L}'(\boldsymbol{\nu}; \boldsymbol{N}; \boldsymbol{\theta}) = \prod_{i=1}^{N_{\text{bins}}} P\left(N_i | \nu_i'\right) \prod_{j=1}^{N_{\text{syst}}} G\left(\theta_j\right), \tag{10.4}$$

where ν is modified to introduce an "efficiency" term ϵ whose magnitude propagates into the Poisson mean according on the nuisance parameters:

$$\nu_i' = \sum_c N_c T_{ci} \left(1 + \sum_j \theta_j \epsilon_{cij} \right), \text{ with c} \in \{\text{signal; background}\},$$

$G(\theta)$ is the probability of sampling θ from a Gaussian distribution with width 1 and mean 0; ϵ_{ij} is the fractional magnitude of the systematic uncertainty j in the bin i. This arrangement treats the systematic uncertainties as Gaussian distributed quantities in the prior distribution. In addition, $N_{\text{background}}$ is also a nuisance parameter in the prior, taken to be distributed as a Gaussian with a mean value equal to the number of background events from the background estimate in chapter 8 and width $\sqrt{N}$.

10.3 Bayesian Analysis Toolkit

As mentioned in the previous section, the likelihood distribution (10.2) must be computed numerically. The BAYESIAN ANALYSIS TOOLKIT (BAT) [80] is used to determine the posterior distribution, making use of a feature called the Multi Template Fitter (known as `BCMTF`) [81]. The `BCMTF` is a tool used for computing likelihoods in the presence of multiple channels, templates and systematic uncertainties. In this case, the `BCMTF` is used with one process, one channel and two templates: signal and background.

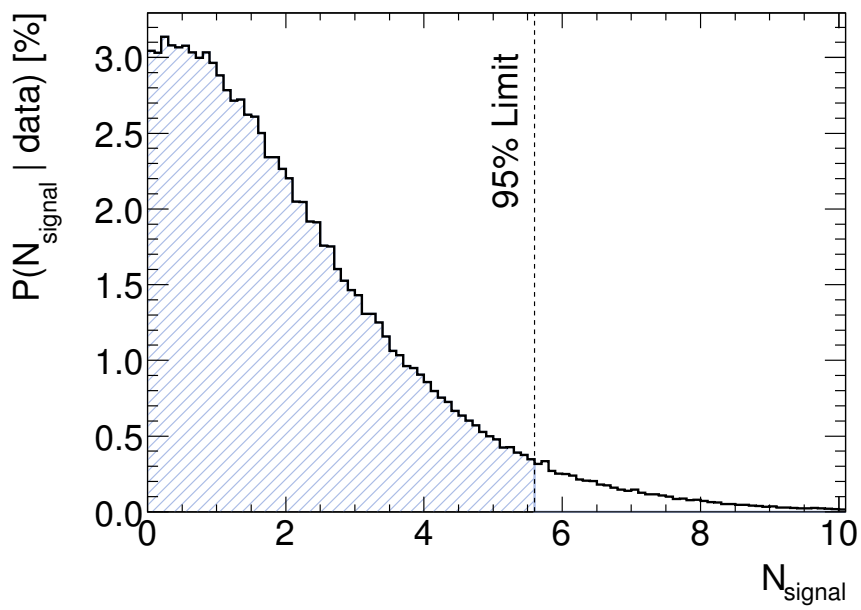

Figure 10.1: Posterior probability distribution in the number of signal events N_{signal}, not corrected for the efficiency, for a graviton template with $m_{\gamma\gamma} = 1\,\text{TeV}$, $k/\overline{M_{\text{pl}}} = 0.1$, given the background and data distributions shown in figure 8.6. The 95% limit is defined as the 95th quantile of this distribution, which is shown hatched.

BAT integrates the likelihood 10.4 through Markov Chain Monte Carlo [80] to reduce it to the marginal distribution in the variable of interest, N_{signal}, removing the dependence on the nuisance parameters $\boldsymbol{\theta}$:

$$\mathscr{L}\left(\boldsymbol{\nu}\left(N_{\text{signal}}\right); \boldsymbol{N}\right) = \int \mathscr{L}'(\boldsymbol{\nu}; \boldsymbol{N}; \boldsymbol{\theta})\,\mathrm{d}\boldsymbol{\theta}.$$

In addition, it computes the posterior distribution as a function of N_{signal} through the relationships in (10.2) and (10.3). Figure 10.1 shows an example of the marginalized posterior distribution for the given the data, the background estimate, and a 1 TeV graviton template.

10.4 Expected limit and limit uncertainty

To determine the expected limit and its uncertainty, $10,000$ background-only toy experiments are performed for each mass point. These toy experiments are generated using the `BCMTFAnalysisFacility` feature [82] of the BAT. Each toy experiment is generated by allowing the background template to fluctuate in each bin according to Poisson statistics. The 95% limit as defined in section 10.2 is measured for each experiment to obtain the distribution of the measure over experiments, which is shown in figure 10.2. For a given mass point, this distribution determines the expected limit and its uncertainty through the median value and the quantiles corresponding to the one and two-sigma intervals.

10.5 Summary

The BUMPHUNTER algorithm provides a mechanism to search for excesses above the expected background in a model independent manner which takes into account the "look elsewhere effect". BAT is then used to measure the 95% upper limit on the cross-section. The next section will present the outcome of measuring the BUMPHUNTER statistic using ATLAS data followed by the measured limit as a function of m_G.

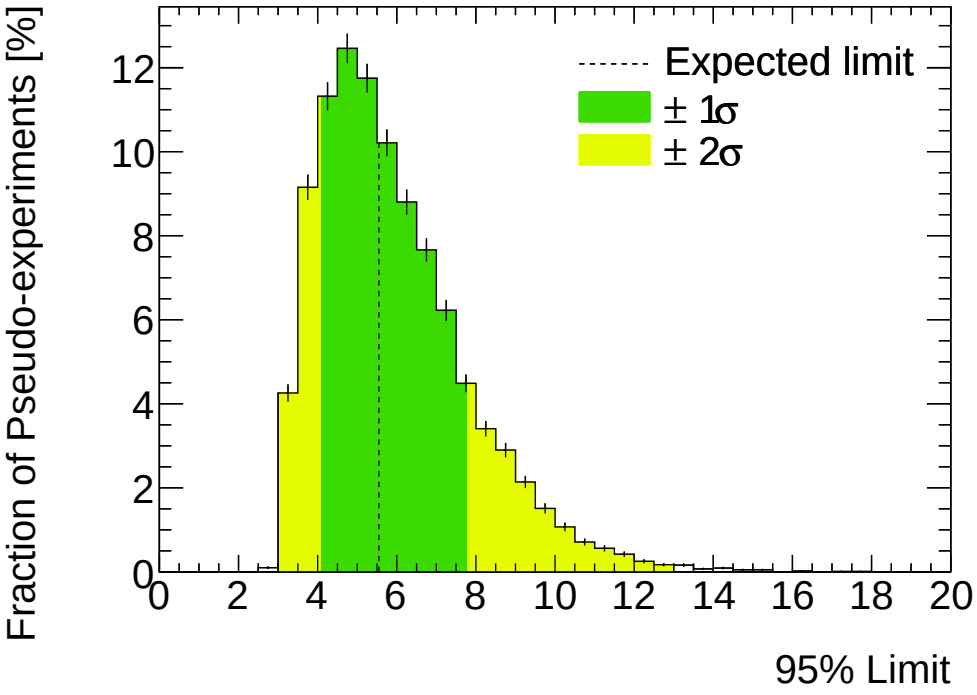

Figure 10.2: Distribution of the limit over background only pseudo-experiments, for a graviton with $k/\overline{M}_{\mathrm{pl}} = 0.1$ and $m_G = 1\,\mathrm{TeV}$, showing the central value as well as the 68.5% and 99.1% intervals which are used as the error on the limit.

Chapter 11

Results

An experiment is a question which science poses to Nature, and a measurement is the recording of Nature's answer.

MAX PLANCK

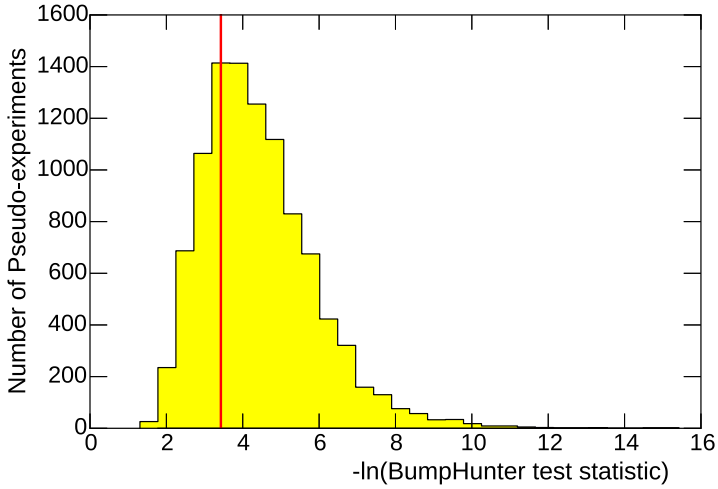

Figure 11.1: Distribution of the negative logarithm of the BUMPHUNTER test statistic over 10,000 pseudo-experiments. The value measured in the data is shown with a red vertical line. Larger values indicate that there exists a region in the data with a significant excess of events over that expected with only the background prediction.

11.1 Measured BumpHunter p-value

The BUMPHUNTER algorithm described in section 10.1 is run with the background estimate obtained in section 8.3. The measured distribution of the BUMPHUNTER test statistic over pseudo-experiments is shown in figure 11.1, along with the BUMPHUNTER test statistic measured in data. The measured p-value of the BUMPHUNTER test statistic is 0.734 ± 0.004, which is consistent with the null hypothesis. The implementation used to calculate this value can be found in appendix A.

11.2 Measured limit

Following the procedures outlined in sections 10.3 and 10.4 and treating all of the systematic effects in chapter 9 as affecting the Poisson mean on the background estimate, the measured N_{signal} limit is shown in figure 11.2. Owing to the small value of the Poisson mean, the systematic uncertainties have an small effect on the expected limit of the order $5 - 10\%$, which decreases at higher masses. The expected limit varies smoothly as a function of m_{G} and therefore is not sampled as frequently as the measured limit. Note that adjacent points in the limit are heavily correlated. The measured limit shows good agreement with the expected limit. The expected limit is approximately 30^{+15}_{-10} at $m_G = 400\,\text{GeV}$ and 3 at high mass where the sensitivity of the experiment runs out, which is consistent with the frequentist expectation.

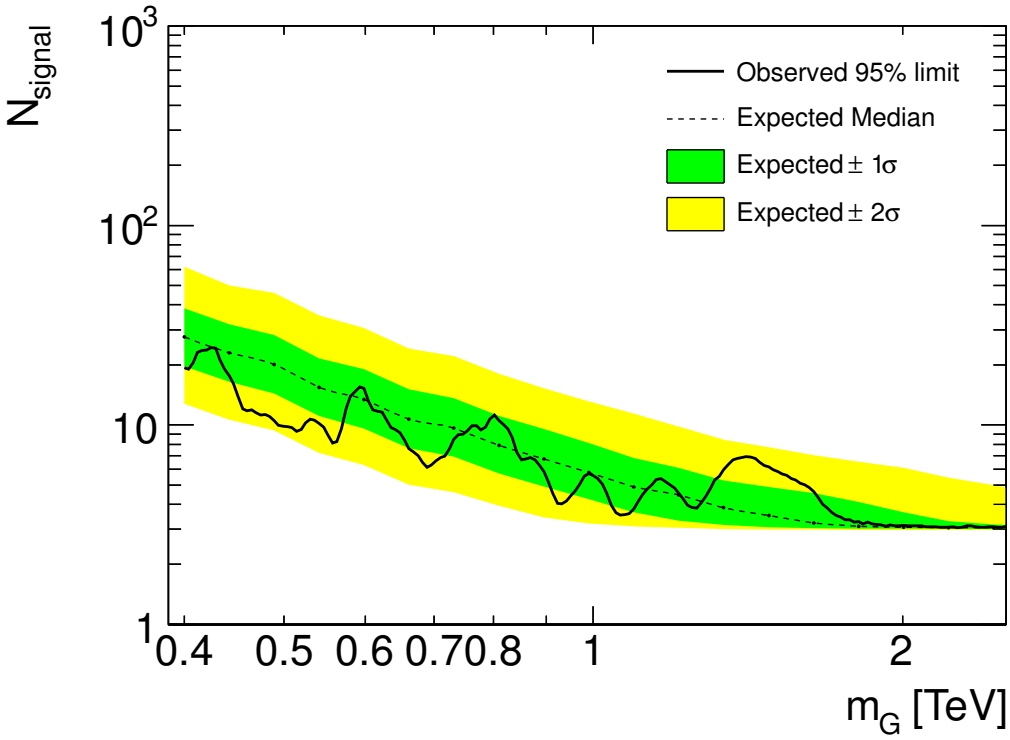

Figure 11.2: Measured and expected limit on N_{signal} as a function of m_G with $\pm 1\sigma$ and $\pm 2\sigma$ uncertainty bands.

11.3 Cross-section limits and interpretation in terms of the Randall Sundrum Model

Figure 11.3 shows the expected and measured cross-section limits as a function of mass, along with the cross-section for the RS model for different values of $k/\overline{M_{\mathrm{pl}}}$. The theory curves shown are those determined in section 2.5. This plot is similar to figure 11.2 except that it is scaled according to:

$$\sigma \mathrm{Br}\left(G \rightarrow \gamma\gamma\right) = \frac{N_{\mathrm{signal}}}{\epsilon \times L},$$

where ϵ is the detector efficiency times acceptance as shown in figure 8.13, and L is the integrated luminosity of the data. The point at which a theory curve intersects the measured limit is where that theory curve is said to be excluded.

Figure 11.4 shows the cross-section limits cast in terms of parameters in the RS model. Points on this plot are derived by interpolating the measured and expected cross-section limits along with their uncertainty bands shown in figure 11.3 with a quintic spline and finding the point at which the theoretical curve intersects the spline as a function of mass and $k/\overline{M_{\mathrm{pl}}}$. It is found that the RS model is excluded up to to 1 TeV at $k/\overline{M_{\mathrm{pl}}} = 0.01$ and approximately 2 TeV at a value of $k/\overline{M_{\mathrm{pl}}} = 0.1$.

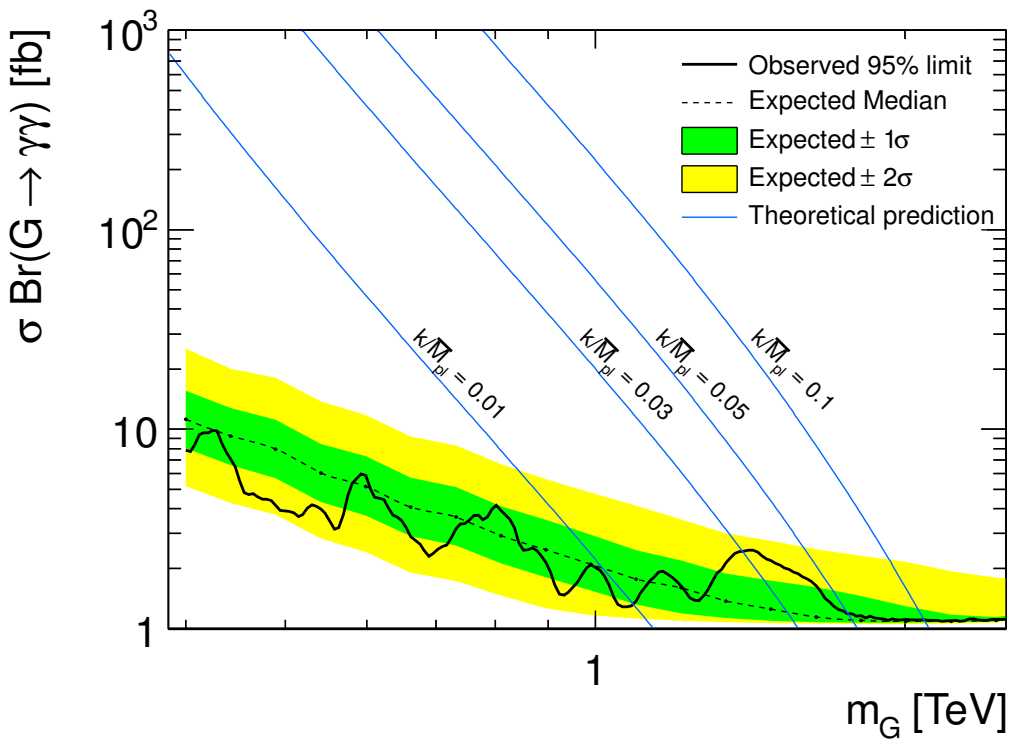

Figure 11.3: Upper limit on the cross-section times branching ratio.

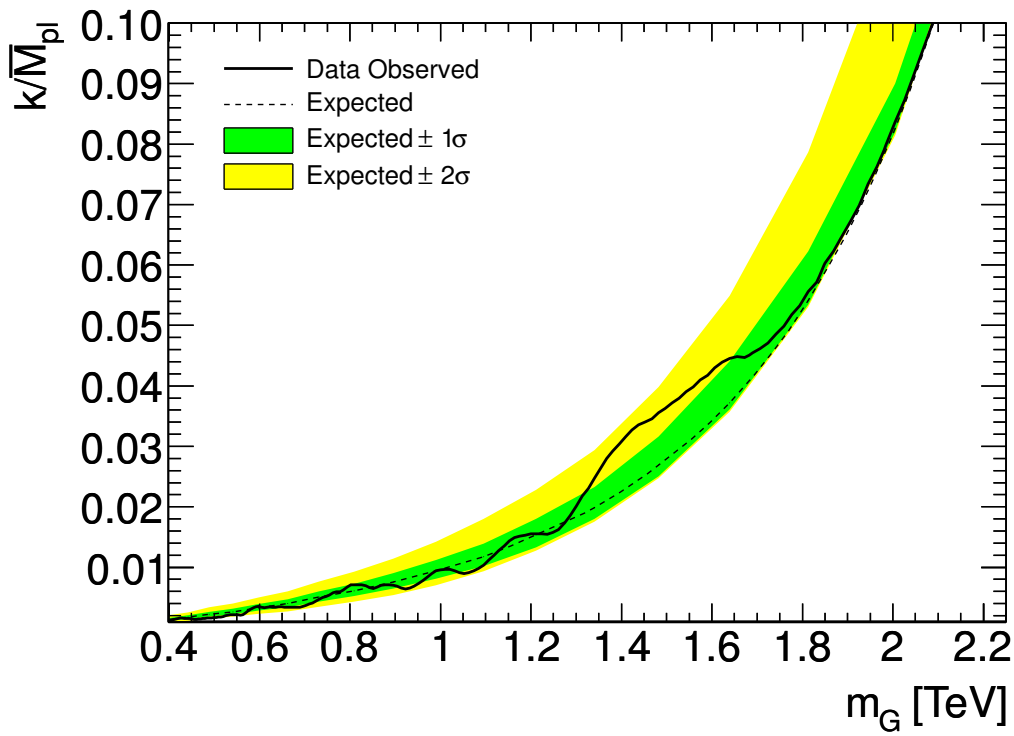

Figure 11.4: The excluded region in the RS model parameter space is shown to the top left of the plot. It shows that the RS model is excluded up to 1 TeV at $k/\overline{M_{\mathrm{pl}}} = 0.01$ and approximately 2 TeV at a value of $k/\overline{M_{\mathrm{pl}}} = 0.1$.

Chapter 12

Summary and Outlook

One never notices what has been done;

one can only see what remains to be done.

MARIE CURIE

This thesis presents a search for narrow resonances with data obtained at ATLAS during $\sqrt{s} = 7\,\text{TeV}$ running during 2011. The diphoton $m_{\gamma\gamma}$ distribution in the ATLAS detector's acceptance is measured in data from 140 GeV to 3 TeV. The relative yields of the four components ($\gamma\gamma$, γj, $j\gamma$, jj) of the background distribution are determined by performing a template fit to the 2-dimensional (tight and isolated) photon isolation distribution using a control region of $140\,\text{GeV} < m_{\gamma\gamma} < 400\,\text{GeV}$. The isolation templates used for the template fit are acquired by using background enhanced samples of photons obtained by reversing some of the cuts used in the photon identification. In a similar manner as the templates of the isolation are obtained, templates of the $m_{\gamma\gamma}$ distribution for the three reducible components (γj, $j\gamma$ and jj) are derived with the same reversed identification cuts. The irreducible $m_{\gamma\gamma}$ template shape is attained by re-weighting the PYTHIA 6 Standard Model direct diphoton simulation including the full ATLAS detector simulation in such a way as to reproduce the generated $m_{\gamma\gamma}$ distribution from DIPHOX. All four components of the $m_{\gamma\gamma}$ background are summed in proportion to the yields obtained from the isolation template fit to obtain a total background shape template. The predicted total background shape template is then normalized to the data in the control region to obtain the background estimate.

The BUMPHUNTER algorithm is run using the background estimate and the data to test for the presence of a significant excess in the data. No such excess is found with a p-value of 0.734 ± 0.004.

Signal templates of $G \to \gamma\gamma$ resonances were obtained for many mass points through a specially prepared simulation sample (including the full detector simulation) where PYTHIA 6 is modified in order to remove the resonant term from the $m_{\gamma\gamma}$, producing a

high-statistics sample with a flat mass distribution. Resonance templates were produced from this sample by repeatedly re-weighting it with the resonance term removed by the procedure used to generate the flat $m_{\gamma\gamma}$ distribution. As the width of the measured graviton resonance is dominated by the detector resolution, the graviton templates are given a $k/\overline{M_{\mathrm{pl}}} = 0.1$, which corresponds to a relativistic Breit-Wigner width slightly larger than the Gaussian detector resolution of $m_{\gamma\gamma}$.

The BAYESIAN ANALYSIS TOOLKIT is used to measure a Bayesian 95% upper limit limit on the number of signal events N_{signal} present in the data according to the total background estimate and signal templates obtained from the graviton template sample. In addition, toy experiments were performed to measure the distribution of this limit over experiments, which is used as the uncertainty band.

For each mass point, the limit on N_{signal} is recast as a limit on $\sigma \times \mathrm{Br}\left(G \to \gamma\gamma\right)$ through the luminosity and the detector acceptance. The m_G-$k/\overline{M_{\mathrm{pl}}}$ exclusion plane is obtained by re-casting the upper limit on $\sigma \times \mathrm{Br}\left(\mathrm{G} \to \gamma\gamma\right)$, which is a function m_G, as an upper limit on the $k/\overline{M_{\mathrm{pl}}}$ for a given m_G through the theoretical cross-section at different values of $k/\overline{M_{\mathrm{pl}}}$ obtained from PYTHIA 8. Randall Sundrum gravitons are excluded in ATLAS 2011 data with a $m_G < 1\,\mathrm{TeV}$ for a $k/\overline{M_{\mathrm{pl}}} = 0.01$ and $m_G < 2\,\mathrm{TeV}$ for $k/\overline{M_{\mathrm{pl}}} = 0.1$.

The recent discovery of the Higgs particle [83, 84] has reaffirmed the Standard Model as a reasonable model of this universe given all of the available experimental data. This has lead to the graviton model being relatively more disfavoured in the theoretical physics community. However, it is not inconceivable that more particles could be theorised. For high mass $\gamma\gamma$ resonances the Randall Sundrum model makes a good standard candle and so an observed limit in this channel may yet be useful to a future theorist.

The ATLAS detector took more data in 2012, approximately $20\,\mathrm{fb}^{-1}$ at a collision energy of $\sqrt{s} = 8\,\mathrm{TeV}$. A similar study as the one presented in this thesis has been repeated and also sets a limit which will be published in the near future. At the time of writing further constraints on the m_G-$k/\overline{M_{\mathrm{pl}}}$ plane have been published in the dilepton channel by ATLAS [85]. The latest results now place the exclusion boundary of $m_G \gtrsim 1.2\,\mathrm{TeV}$ at $k/\overline{M_{\mathrm{pl}}} = 0.01$ and $m_G \gtrsim 2.5\,\mathrm{TeV}$ at $k/\overline{M_{\mathrm{pl}}} = 0.1$. This leaves a tiny amount of parameter space which extends out to 3.5 TeV in the m_G-$k/\overline{M_{\mathrm{pl}}}$ plane. With the resumption of the LHC at 13 TeV in 2015, there is an ever decreasing amount of Randall-Sundrum parameter space left. However, whatever is accessible to experiment should be measured as the universe could have as-yet unimagined behaviour.

Acknowledgements

If at first you don't succeed, try, try, try again.

WHAT I NEEDED TO BE TOLD A MILLION TIMES

Thanks to everyone who got me here. First and foremost to Ona, who put up with many a stressful night; I don't know where I would be without you. My supervisors, Helen and Steve, thanks for seeing me through to the end of this thing and pushing me over the final bump. Johannes, thanks for keeping me sane. Your friendship and wisdom have been amazing, it has been great working with you. To my parents, thanks for your lifelong support and facilitating my interests in interesting things. Richard, thanks for the encouragement. Noel, thanks for getting a great group of developers to rally around that project and thanks for your time in general, I'm really pleased we met. Thanks to Lindsey Grey and Peter Loscutoff for the great chilli evenings.

Xabier Anduaga and Quentin Buat (among many others) deserve a lot of credit for bringing together the analysis notes and organizing the group in general. Thanks to Peter Onyisi for his DQ efforts and giving me interesting things to work on. Dan Hayden and Mike Hance for their input and inspiration on gravitons and photons, along with Will Buttinger and Georgios Choudalakis for their input on statistical magic.

A shout out to my colleagues and fellow students at Liverpool; Matt, Graham, Joe, Yan-Jie, Dean, Ben, Miffy, Oliver and too many other people to list, for great beer, great coffee and great raving about the world. Thanks to the sys-admins Rob and John who dealt with my crazy requests with incredible punctuality, you guys are an undervalued asset. And to anyone else who made the ATLAS experiment possible: the designers, builders, studiers, administrators, organizers and facilitators who all made it possible.

I'd like to mention my old teachers who gave me an interest in physics the tools to have a crack at it: Stefan Söldner-Rembold and Terry Wyatt at Manchester University for giving me interesting opportunities in particle physics, Steve Preston, the A-level teacher who made physics cool and inspired me greatly; and my aunt Sue, who gave some of her spare time to train me to actually *think* about mathematics.

This work was funded by the Science & Technology Facilities Council.

Author's Contributions

This work builds upon the work of thousands of others in the ATLAS collaboration, to whom the ATLAS experiment and this document owe their existence. In particular:

- The ATLAS software infrastructure [51] was used
- The description of the detector is based on those found in [29, 56]
- Corrections were chosen to be compatible with the official recommendations of the $e\gamma$ and $G \to \gamma\gamma$ working groups
- Many techniques used in this analysis are based on existing techniques

the main items derived from ATLAS data which are distinct in this thesis include:

- The background estimate, BumpHunter and limit measurement
- The analysis code used to derive the results in this thesis
- The usage of Pythia 8 cross-sections and the usage of the graviton template samples

Contribution to the Data Quality infrastructure of ATLAS

I was part of the team which undertook the design and implementation of the defects database and wrote the first implementation of the DQDefects [86] package, which is the primary mechanism for storing, retrieving and computing information regarding defects. In addition, I wrote a program which can generate the visualisation of the relationship between defects using Graphviz [87] (Figures 4.1 and 4.2). The DCSCalculator [44] was updated so that it could automatically insert defects into the database. A library called DQUtils [88] was written which implements an efficient and easy to use algorithm (under the name '`process_iovs`') for manipulating interval-of-validity based data from Cool. The existence of this library allowed the rapid implementation of DQDefects and other tools. Further information including dependency visualisations for other defects can be found linked from the DQDefects ATLAS TWiki page [86].

Other contributions

Over the course of writing my thesis, in collaboration with others, I also wrote a number of small bits of software of interest to the community. MCViz [23] is a general software package for visualizing simulated physics events (figure 2.9). A4 [89] is an experimental file format which is thread-safe by design and showed a factor of four speed improvement over existing methods, along with several other interesting properties. Rootpy [90] is a python package which aims to provide a consistent python interface to Root, to make it more robust against user error. It was presented at the Root users' workshop 2013 [91].

Bibliography

[1] T. Rothman and S. Boughn. Can gravitons be detected? *Foundations of Physics*, 36(12):1801–1825, November 2006. arXiv:gr-qc/0601043, doi:10.1007/s10701-006-9081-9. 2

[2] S. Glashow. Partial symmetries of weak interactions. *Nucl.Phys.*, 22:579–588, 1961. doi:10.1016/0029-5582(61)90469-2. 6

[3] S. Weinberg. A model of leptons. *Phys. Rev. Lett.*, 19:1264–1266, November 1967. doi:10.1103/PhysRevLett.19.1264. 6

[4] Wikipedia. Standard Model of Elementary Particles.svg — Wikipedia, the free encyclopedia, 2013. [Creative Commons Attribution 3.0 unported license by Wikipedia user MissMJ. Online; accessed April 2013]. URL: http://en.wikipedia.org/wiki/File:Standard_Model_of_Elementary_Particles.svg. 7

[5] S. Chekanov et al. Measurement of the neutral current cross-section and F(2) structure function for deep inelastic e + p scattering at HERA. *Eur.Phys.J.*, C21:443–471, 2001. arXiv:hep-ex/0105090, doi:10.1007/s100520100749. 9

[6] S. Chekanov et al. Measurement of high Q^2 charged current cross-sections in e+p deep inelastic scattering at HERA. *Eur.Phys.J.*, C32:1–16, 2003. arXiv:hep-ex/0307043, doi:10.1140/epjc/s2003-01363-5. 9

[7] P. M. Nadolsky, H. L. Lai, Q. H. Cao, et al. Implications of CTEQ global analysis for collider observables. *Physical Review D*, 78(1):013004, July 2008. arXiv:0802.0007, doi:10.1103/PhysRevD.78.013004. 9

[8] A. Sherstnev and R. Thorne. Different PDF approximations useful for LO Monte-Carlo generators. page 149, 2008. arXiv:0807.2132, doi:10.3360/dis.2008.149. 9, 59

[9] A. Martin, W. Stirling, R. Thorne, and G. Watt. Parton distributions for the LHC. *The European Physical Journal C*, 63(2):189–285, 2009. doi:10.1140/epjc/s10052-009-1072-5. 9

[10] Durham HepData Project. On-line unpolarized parton distribution calculator with graphical display, 2013. [Online; accessed April 2013]. URL: http://hepdata.cedar.ac.uk/pdfs. 9

[11] N. Arkani-Hamed, S. Dimopoulos, and G. Dvali. The hierarchy problem and new dimensions at a millimeter. *Physics Letters B*, 429:263–272, June 1998. arXiv:arXiv:hep-ph/9803315, doi:10.1016/S0370-2693(98)00466-3. 11, 16

[12] L. Randall and R. Sundrum. An alternative to compactification. *Phys. Rev. Lett.*, 83:4690–4693, 1999. arXiv:hep-th/9906064. 13

[13] H. Davoudiasl, J. L. Hewett, and T. G. Rizzo. Experimental probes of localized gravity: on and off the wall. *Phys. Rev.*, D63:075004, 2001. arXiv:hep-ph/0006041. 13, 26

[14] L. Randall. Large Mass Hierarchy from a Small Extra Dimension. *Physical Review Letters*, 83(17):3370–3373, 1999. URL: http://arxiv.org/abs/hep-ph/9905221, arXiv:9905221, doi:10.1103/PhysRevLett.83.3370. 15

[15] C. Macesanu, C. McMullen, and S. Nandi. New signal for universal extra dimensions. *Phys.Lett.*, B546:253–260, 2002. arXiv:hep-ph/0207269, doi:10.1016/S0370-2693(02)02694-1. 16

[16] T. G. Rizzo. Z' Phenomenology and the LHC. *ArXiv High Energy Physics - Phenomenology e-prints*, October 2006. arXiv:arXiv:hep-ph/0610104. 17

[17] T. Sjöstrand, S. Mrenna, and P. Skands. A brief introduction to PYTHIA 8.1. *Computer Physics Communications*, 178:852–867, June 2008. arXiv:0710.3820, doi:10.1016/j.cpc.2008.01.036. 17

[18] M. C. Kumar, P. Mathews, V. Ravindran, and A. Tripathi. Direct photon pair production at the LHC to O(α) in TeV scale gravity models. *Nuclear Physics B*, 818:28–51, 2009. arXiv:0902.4894, doi:10.1016/j.nuclphysb.2009.03.022. 17, 110

[19] B. C. Allanach, K. Odagiri, M. J. Palmer, et al. Exploring Small Extra Dimensions at the Large Hadron Collider. *Journal of High Energy Physics*, 12:39, December 2002. arXiv:arXiv:hep-ph/0211205, doi:10.1088/1126-6708/2002/12/039. 17

[20] J. Ellis, R. Fok, D. S. Hwang, V. Sanz, and T. You. Distinguishing 'Higgs' spin hypotheses using gamma gamma and WW^* decays. *ArXiv e-prints*, 2012. arXiv:1210.5229. 21

[21] T. Binoth, J. Guillet, E. Pilon, and M. Werlen. A full next-to-leading order study of direct photon pair production in hadronic collisions. *The European Physical Journal C - Particles and Fields*, 16:311–330, 2000. arXiv:hep-ph/9911340v3, doi:10.1007/s100520050024. 22

[22] G. Aad et al. Measurement of isolated-photon pair production in pp collisions at $\sqrt{s} = 7$ TeV with the ATLAS detector. *JHEP*, 1301:086, 2013. arXiv:1211.1913, doi:10.1007/JHEP01(2013)086. 24

[23] J. Ebke, P. Waller, T. Brooks, et al. MCViz - high energy physics Monte-Carlo event visualizer, 2013. [Online; accessed June 2013]. URL: http://mcviz.net,http://github.com/mcviz/mcviz. 25, 136

[24] T. G. Rizzo. Pedagogical introduction to extra dimensions. *ArXiv High Energy Physics - Phenomenology e-prints*, 2004. arXiv:arXiv:hep-ph/0409309. 26

[25] DØ collaboration. Search for Randall-Sundrum gravitons in the dielectron and diphoton final states with 5.4 fb^{-1} of data from $p\overline{p}$ collisions at $\sqrt{s} = 1.96$ TeV. *Phys. Rev. Lett.*, 104:241802, June 2010. doi:10.1103/PhysRevLett.104.241802. 26

[26] CDF collaboration. Search for new dielectron resonances and randall-sundrum gravitons at the collider detector at fermilab. *Phys. Rev. Lett.*, 107:051801, July 2011. doi:10.1103/PhysRevLett.107.051801. 26

[27] ATLAS collaboration. Dilepton resonances at high mass. Technical Report ATL-PHYS-PUB-2009-070. ATL-COM-PHYS-2009-093, CERN, Geneva, March 2009. 1st of the 5 Exotics CSC notes. URL: http://cdsweb.cern.ch/record/1166294. 27

[28] L. Evans. LHC Machine. *Journal of Instrumentation*, 3(08):S08001–S08001, August 2008. doi:10.1088/1748-0221/3/08/S08001. 29

[29] ATLAS collaboration. The ATLAS experiment at the CERN Large Hadron Collider. *Journal of Instrumentation*, 3(08):S08003–S08003, August 2008. doi:10.1088/1748-0221/3/08/S08003. 30, 32, 33, 34, 35, 36, 39, 41, 43, 44, 45, 135

[30] ALICE collaboration. The ALICE experiment at the CERN LHC. *Journal of Instrumentation*, 3(08):S08002, 2008. doi:10.1088/1748-0221/3/08/S08002. 30

[31] CMS collaboration. The CMS experiment at the CERN LHC. *Journal of Instrumentation*, 3(08):S08004, 2008. doi:10.1088/1748-0221/3/08/S08004. 30

[32] LHCb collaboration. The LHCb detector at the LHC. *Journal of Instrumentation*, 3(08):S08005, 2008. doi:10.1088/1748-0221/3/08/S08005. 30

[33] ATLAS collaboration. Improved luminosity determination in pp collisions at $\sqrt{s} = 7$ TeV using the ATLAS detector at the LHC. Technical Report ATLAS-CONF-2012-080, CERN, Geneva, July 2012. 30, 59, 109, 111

[34] ATLAS Public. LuminosityPublicResults — ATLAS TWiki. Revision 40, updated March 2013. URL: TWiki:https://twiki.cern.ch/twiki/bin/view/AtlasPublic/LuminosityPublicResults. 30, 59

[35] TOTEM collaboration. First measurement of the total proton-proton cross-section at the LHC energy of $\sqrt{s} = 7$ TeV. *EPL (Europhysics Letters)*, 96:21002, 2011. arXiv:1110.1395, doi:10.1209/0295-5075/96/21002. 31

[36] T. A. Collaboration et al. The ATLAS Experiment at the CERN Large Hadron Collider. *Journal of Instrumentation*, 3(08):S08003–S08003, August 2008. URL: http://stacks.iop.org/1748-0221/3/i=08/a=S08003?key=crossref.b2ac868e8992413771c34191a8138368, doi:10.1088/1748-0221/3/08/S08003. 40

[37] *ATLAS liquid-argon calorimeter: Technical Design Report*. Technical Design Report ATLAS. CERN, Geneva, 1996. URL: http://cdsweb.cern.ch/record/331061. 40, 42

[38] ATLAS collaboration. Readiness of the ATLAS Liquid Argon Calorimeter for LHC collisions. *European Physical Journal C*, 70:723–753, December 2010. arXiv:0912.2642, doi:10.1140/epjc/s10052-010-1354-y. 42

[39] ATLAS collaboration. Readiness of the ATLAS Tile Calorimeter for LHC collisions. *European Physical Journal C*, 70:1193–1236, December 2010. arXiv:1007.5423, doi:10.1140/epjc/s10052-010-1508-y. 42

[40] ATLAS collaboration. Performance of the ATLAS Trigger System in 2010. *Eur. Phys. J. C 72 (2012) 1849*. arXiv:arXiv:1110.1530v2, doi:{10.1140/epjc/s10052-011-1849-1}. 44

[41] ATLAS collaboration. *ATLAS high-level trigger, data-acquisition and controls: Technical Design Report*. Technical Design Report ATLAS. CERN, Geneva, 2003. 44

[42] J. Zhang. ATLAS data acquisition. In *Real Time Conference, 2009. RT '09. 16th IEEE-NPSS*, pages 240 –243, may 2009. doi:10.1109/RTC.2009.5321758. 46

[43] R. Brun and F. Rademakers. Root — an object oriented data analysis framework. *Nuclear Instruments and Methods in Physics Research Section A: Accelerators, Spectrometers, Detectors and Associated Equipment*, 389(1–2):81 – 86, 1997. URL: http://www.sciencedirect.com/science/article/pii/S016890029700048X, doi:10.1016/S0168-9002(97)00048-X. 47

[44] G. Aad, J. Adelman, et al. Data quality from the Detector Control System at the ATLAS experiment. *Journal of Physics: Conference Series*, 219(2):022037, 2010. URL: http://stacks.iop.org/1742-6596/219/i=2/a=022037. 50, 136

[45] ATLAS collaboration. Data Quality Monitoring Framework for the ATLAS experiment: performance achieved with colliding beams at the LHC. *J. Phys.: Conf. Ser.*, 331:22–27. doi:10.1088/1742-6596/331/2/022027. 50

[46] A. Valassi, R. Basset, et al. COOL, LCG conditions database for the LHC experiments: development and deployment status. In *Nuclear Science Symposium Conference*

Record, 2008. NSS '08. IEEE, pages 3021 –3028, October 2008. doi:10.1109/NSSMIC.2008.4774995. 50, 52

[47] M. Verducci. ATLAS conditions database experience with the LCG COOL conditions database project. *Journal of Physics: Conference Series*, 119(4):042031, 2008. URL: http://stacks.iop.org/1742-6596/119/i=4/a=042031. 50

[48] T. Golling, H. S. Hayward, P. U. E. Onyisi, H. J. Stelzer, and P. Waller. The ATLAS data quality defect database system. *European Physical Journal C*, 72:1960, April 2012. arXiv:1110.6119, doi:10.1140/epjc/s10052-012-1960-y. 51

[49] [Retrieved July 2012]. URL: http://atlasdqm.web.cern.ch/atlasdqm/defect_graph/. 56

[50] ATLAS collaboration. ATLAS computing: Technical design report. 2005. 59

[51] ATLAS collaboration. The ATLAS simulation infrastructure. *The European Physical Journal C*, 70(3):823–874, 2010. arXiv:1005.4568, doi:10.1140/epjc/s10052-010-1429-9. 59, 135

[52] T. Sjöstrand, S. Mrenna, and P. Skands. PYTHIA 6.4 physics and manual. *Journal of High Energy Physics*, 2006(05):026–026, May 2006. doi:10.1088/1126-6708/2006/05/026. 59

[53] M. Whalley, D. Bourilkov, and R. Group. The Les Houches accord PDFs (LHAPDF) and LHAGLUE. 2005. arXiv:hep-ph/0508110. 59

[54] S. Agostinelli, J. Allison, K. Amako, et al. Geant4—a simulation toolkit. *Nuclear Instruments and Methods in Physics Research Section A: Accelerators, Spectrometers, Detectors and Associated Equipment*, 506(3):250 – 303, 2003. URL: http://www.sciencedirect.com/science/article/pii/S0168900203013688, doi:10.1016/S0168-9002(03)01368-8. 59

[55] Wikipedia. Relativistic Breit-Wigner distribution — Wikipedia, the free encyclopedia, 2013. [Online; accessed 17-June-2013]. URL: http://en.wikipedia.org/w/index.php?title=Relativistic_Breit%E2%80%93Wigner_distribution&oldid=551264127. 62

[56] ATLAS collaboration. Expected Performance of the ATLAS Experiment - Detector, Trigger and Physics. 2009. arXiv:0901.0512. 68, 72, 135

[57] ATLAS collaboration. Search for diphoton events with large missing transverse momentum in 7 TeV proton-proton collision data with the ATLAS detector. *Phys.Lett.*, B718:411–430, 2012. arXiv:1209.0753, doi:10.1016/j.physletb.2012.10.069. 69

[58] ATLAS collaboration. Measurement of the isolated diphoton cross section in pp collisions at $\sqrt{s} = 7$ TeV with the ATLAS detector. *Physical Review D*, 85(1):012003, 2012. arXiv:1107.0581, doi:10.1103/PhysRevD.85.012003. 69

[59] ATLAS collaboration. Measurement of inclusive jet and dijet cross sections in proton-proton collisions at 7 TeV centre-of-mass energy with the ATLAS detector. *European Physical Journal C*, 71:1512, 2011. arXiv:1009.5908, doi:10.1140/epjc/s10052-010-1512-2. 69

[60] W. Lampl et al. Calorimeter clustering algorithms: Description and performance. Technical Report ATL-COM-LARG-2008-003, CERN, Geneva, April 2008. URL: https://cdsweb.cern.ch/record/1099735. 71

[61] Expected electron performance in the ATLAS experiment. Technical Report ATL-PHYS-PUB-2011-006, CERN, Geneva, April 2011. URL: https://cdsweb.cern.ch/record/1345327. 71, 79

[62] ATLAS collaboration. Measurements of the photon identification efficiency with the atlas detector using 4.9 fb^{-1} of pp collision data collected in 2011. Technical Report ATLAS-CONF-2012-123, CERN, Geneva, August 2012. 73, 80, 110, 111

[63] Expected photon performance in the atlas experiment. Technical Report ATL-PHYS-PUB-2011-007, CERN, Geneva, April 2011. 78

[64] ATLAS collaboration. Electron performance measurements with the ATLAS detector using the 2010 LHC proton-proton collision data. *European Physical Journal C*, 72:1909, 2012. arXiv:1110.3174, doi:10.1140/epjc/s10052-012-1909-1. 79

[65] M. Hance. *Measurement of inclusive isolated prompt photon production at $\sqrt{s} = 7$ TeV with the ATLAS detector*. PhD thesis, University of Pennsylvania, 2011. URL: http://repository.upenn.edu/dissertations/AAI3485700. 80

[66] G. Aad, T. Abajyan, B. Abbott, et al. Search for high-mass resonances decaying to dilepton final states in pp collisions at sqrt{s}=7 TeV with the ATLAS detector. *Journal of High Energy Physics*, 11:138, November 2012. arXiv:1209.2535, doi:10.1007/JHEP11(2012)138. 83

[67] S. Alekhin, S. Alioli, R. D. Ball, et al. The PDF4LHC Working Group Interim Report. *ArXiv e-prints*, 2011. arXiv:1101.0536. 87

[68] ATLAS Internal. Search for evidence of extra dimensions in the diphoton final state in $\sqrt{s} = 7$ TeV pp collisions. Technical Report ATL-COM-PHYS-2011-1078, CERN, Geneva, August 2011. 88, 107

[69] K. Cranmer. Kernel estimation in high-energy physics*. *Computer Physics Communications*, 136:198–207, May 2001. arXiv:arXiv:hep-ex/0011057, doi:10.1016/S0010-4655(00)00243-5. 90

[70] W. Verkerke and D. Kirkby. The RooFit toolkit for data modeling. *ArXiv Physics e-prints*, June 2003. arXiv:arXiv:physics/0306116. 90, 106

[71] Babar collaboration. Babar glossary, retrieved April 2013. URL: http://www.slac.stanford.edu/babar-pro-new/search.pl?letter=N. 91

[72] Wikipedia. Crystal ball function — Wikipedia, the free encyclopedia, 2013. [Online; accessed April 2013]. URL: http://en.wikipedia.org/w/index.php?title=Crystal_Ball_function&oldid=544117166. 91

[73] Wikipedia. Voigt profile — Wikipedia, the free encyclopedia, 2013. [Online; accessed 20-June-2013]. URL: http://en.wikipedia.org/w/index.php?title=Voigt_profile&oldid=541315730. 99

[74] J. Campbell, K. Ellis, and C. Williams. MCFM - Monte Carlo for FeMtobarn processes, 2013. [Online; accessed June 2013]. URL: http://mcfm.fnal.gov. 105

[75] J. Campbell and R. K. Ellis. Radiative corrections to $Zb\overline{b}$ production. *Phys. Rev. D*, 62(11):114012, December 2000. arXiv:arXiv:hep-ph/0006304, doi:10.1103/PhysRevD.62.114012. 105

[76] ATLAS collaboration. Search for Extra Dimensions in the Diphoton Channel using 4.9/fb of Proton-Proton Collisions recorded at 7 TeV with the ATLAS Detector. Technical Report ATLAS-CONF-2012-087, CERN, Geneva, July 2012. 108, 110, 111

[77] K. Liu, Y. Liu, and G. Marchiori. Measurement of the identification efficiency of isolated prompt photons using the matrix method and 4.9 fb^{-1} of atlas data. Technical Report ATL-COM-PHYS-2012-242, CERN, Geneva, March 2012. 110

[78] E. Gross and O. Vitells. Trial factors for the look elsewhere effect in high energy physics. *European Physical Journal C*, 70:525–530, November 2010. arXiv:1005.1891, doi:10.1140/epjc/s10052-010-1470-8. 113

[79] G. Choudalakis. On hypothesis testing, trials factor, hypertests and the BumpHunter. *ArXiv e-prints*, 2011. arXiv:1101.0390. 114

[80] A. Caldwell, D. Kollár, and K. Kröninger. BAT - The Bayesian Analysis Toolkit. *Computer Physics Communications*, 180:2197–2209, November 2009. arXiv:0808.2552, doi:10.1016/j.cpc.2009.06.026. 118, 119

[81] BAT Authors. BayesianAnalysisToolkit: BCMTF Class Reference, 2013. [Online; accessed June 2013]. URL: http://www.mppmu.mpg.de/bat/docs/refman/html-0.9.2/class_b_c_m_t_f.html. 118

[82] BAT Authors. BayesianAnalysisToolkit: BCMTFAnalysisFacility Class Reference, 2013. [Online; accessed June 2013]. URL: http://www.mppmu.mpg.de/bat/docs/refman/html-0.9.2/class_b_c_m_t_f_analysis_facility.html. 120

[83] ATLAS collaboration. Observation of a new particle in the search for the Standard Model Higgs boson with the ATLAS detector at the LHC. *ArXiv e-prints*, July 2012. arXiv:1207.7214. 131

[84] CMS collaboration. Observation of a new boson at a mass of 125 GeV with the CMS experiment at the LHC. *ArXiv e-prints*, July 2012. arXiv:1207.7235. 131

[85] Search for high-mass dilepton resonances in 20 fb^{-1} of pp collisions at $\sqrt{s} =$ 8 TeV with the ATLAS experiment. Technical Report ATLAS-CONF-2013-017, CERN, Geneva, Mar 2013. 132

[86] ATLAS Internal. Revision 7, updated September 2011. URL: https://twiki.cern.ch/twiki/bin/viewauth/Atlas/DQDefects. 136

[87] J. Ellson, E. R. Gansner, E. Koutsofios, S. C. North, and G. Woodhull. Graphviz and dynagraph – static and dynamic graph drawing tools. In *GRAPH DRAWING SOFTWARE*, pages 127–148. Springer-Verlag, 2003. 136

[88] ATLAS Internal. Revision 1, updated August 2011. URL: https://twiki.cern.ch/twiki/bin/viewauth/Atlas/DQUtils. 136

[89] J. Ebke and P. Waller. The A4 project: physics data processing using the Google protocol buffer library. *Journal of Physics Conference Series*, 396(2):022012, December 2012. arXiv:1208.1600, doi:10.1088/1742-6596/396/2/022012. 136

[90] The rootpy developers. rootpy: A feature-rich pythonic interface with the ROOT libraries on top of the PyROOT bindings — GitHub, 2013. [Online; accessed June 2013, if unavailable contact author by e-mail at p@pwaller.net]. URL: http://rootpy.org. 136

[91] N. Dawe. ROOT Users Workshop 2013 – rootpy: Pythonic ROOT, 2013. [Online; accessed June 2013, if unavailable contact author by e-mail at p@pwaller.net]. URL: http://indico.cern.ch/contributionDisplay.py?contribId=15&confId=217511. 136

[92] P. Waller. bumphunter.pw: Simple implementation of the BumpHunter algorithm — GitHub, 2013. [Online; accessed May 2013, if unavailable contact author by e-mail at p@pwaller.net]. URL: https://github.com/pwaller/bumphunter.pw/. 151

[93] W. Buttinger. StatTools: Implementation of the BumpHunter algorithm — GitHub, 2013. [Online; accessed May 2013]. URL: https://github.com/wbuttinger/StatTools/. 151

Appendix A

BumpHunter Implementation

The source code in this appendix can be found at [92] and was loosely based on the implementation found at [93].

```
#! /usr/bin/env python

from math import log, sqrt

from numpy import array, random
from scipy.stats import percentileofscore, poisson

def evaluate_statistic(data, mc, verbose=False, edges=None):
    # Get search range (first bin with data, last bin with data)
    nzi, = mc.nonzero() # nzi = non-zero indices
    search_lo, search_hi = nzi[0], nzi[-1]

    def all_windows():
        "Iterator returning [lo, hi) for all windows"
        # Try windows from one bin in width up to half of the full range
        min_win_size, max_win_size = 1, (search_hi - search_lo) // 2
        for binwidth in xrange(min_win_size, max_win_size):
            if verbose: print " --- binwidth = ", binwidth
            step = max(1, binwidth // 2) # Step size <- half binwidth
            for pos in xrange(search_lo, search_hi - binwidth, step):
                yield pos, pos + binwidth
```

```
22
23      def pvalue(lo, hi):
24          "Compute p value in window [lo, hi)"
25          d, m = data[lo:hi].sum(), mc[lo:hi].sum()
26          if m == 0:
27              # MC prediction is zero. Not sure what then..
28              assert d == 0, "Data = {0} where the prediction is zero..".format(d)
29              return 1
30          if d < m: return 1 # "Dips" get ignored.
31
32          # P(d >= m)
33          p = 1 - poisson.cdf(d-1, m)
34
35          if verbose and edges:
36              print "{0:2} {1:2} [{2:8.3f}, {3:8.3f}] {4:7.0f} {5:7.3f} {6:.5f} {7:.2f}".format(
37                  lo, hi, edges[lo], edges[hi], d, m, p, -log(p))
38
39          return p
40
41      min_pvalue, (lo, hi) = min((pvalue(lo, hi), (lo, hi))
42                                 for lo, hi in all_windows())
43
44      return -log(min_pvalue), (lo, hi)
45
46  def make_toys(prediction, n):
47      "fluctuate ‘prediction‘ input distribution ‘n‘ times"
48      return random.mtrand.poisson(prediction, size=(n, len(prediction)))
49
50  def bumphunter(hdata, hmc, n):
51      "Compute the bumphunter statistic and run ‘n‘ pseudo-experiments"
52      data = array([hdata[i] for i in xrange(1, hdata.GetNbinsX())])
53      mc   = array([hmc[i]   for i in xrange(1, hmc.GetNbinsX())])
54
55      pseudo_experiments = [evaluate_statistic(pe, mc)[0]
56                            for pe in make_toys(mc, n)]
57
58      measurement, (lo, hi) = evaluate_statistic(data, mc)
59
60      pvalue = 1. - (percentileofscore(pseudo_experiments, measurement) / 100.)
61      pvalue_uncertainty = sqrt(pvalue * (1. - pvalue) / n)
62
63      return measurement, (lo, hi), pseudo_experiments, pvalue, pvalue_uncertainty
```

Appendix B

Discriminating Variables of the Highest Mass Events

Run	191715		186934		189288		186178		190618	
Event	37274906		4101410		8202117		360016		54000790	
Mass	1.59		1.48		1.37		1.36		1.19	
	Lead	Sublead	Lead	Sublead	Lead	Sublead	Lead	Sublead	Lead	Sublead
pt	806	776	504	471	530	524	241	213	178	82.3
pt(corr)	787	760	508	471	528	521	251	203	175	83.4
etas2	1.29	1.02	-1.60	0.342	-0.504	1.02	1.85	-1.70	-2.30	2.26
phi	1.69	-1.46	-0.581	2.58	1.06	-2.08	2.57	-1.25	-1.45	2.78
iso	6.75	8.16	4.06	5.36	2.31	5.91	2.31	5.27	0.173	6.29
iso(corr)	2.66	2.54	1.19	1.86	-0.293	2.96	0.0254	2.93	-4.49	2.17
rhad1	0.000377	0.000265	0.00260	0.000821	0.000168	0.0000749	0.00175	0.00841	0.000188	-0.00143
rhad	0.000324	0.000277	0.00221	0.000680	0.000258	0.000121	-0.000212	0.0105	-0.000231	0.00150
E277	1.20e+3	930	858	379	473	702	720	526	622	263
reta	0.959	0.958	0.963	0.968	0.966	0.966	0.961	0.967	0.931	0.928
rphi	0.953	0.965	0.964	0.963	0.965	0.968	0.969	0.969	0.939	0.935
weta2	0.00975	0.00937	0.00971	0.00925	0.00891	0.00927	0.00997	0.00910	0.0117	0.0116
f1	0.129	0.136	0.269	0.207	0.182	0.0734	0.0752	0.0301	0.266	0.316
fside	0.287	0.270	0.279	0.179	0.185	0.312	0.150	0.294	0.146	0.206
wstot	2.33	2.03	2.20	1.75	1.85	2.23	1.48	2.29	1.15	1.37
ws3	0.652	0.620	0.618	0.559	0.614	0.624	0.552	0.565	0.589	0.641
deltae	0	32	100	17	5	30	55	57	53	0
eratio	1	0.995	0.994	0.986	0.993	0.990	0.993	0.971	0.997	1
conv	Yes	Single	Yes	Yes	Single	No	No	No	Yes	Single

Run	191139		182516		191426		180710		182726	
Event	72902862		27413769		14315718		64525366		3232763	
Mass	1.13		1.02		1.01		0.973		0.902	
	Lead	Sublead	Lead	Sublead	Lead	Sublead	Lead	Sublead	Lead	Sublead
pt	128	118	167	116	457	445	150	148	230	93.0
pt(corr)	131	121	163	119	458	444	153	145	222	94.5
etas2	2.15	-2.25	-1.71	2.24	-0.0999	0.876	-1.62	2.10	1.30	-2.31
phi	0.505	-0.163	0.637	-1.52	0.636	-2.42	0.511	3.02	0.239	-2.84
iso	1.95	3.39	0.964	3.40	1.41	2.16	2.26	0.810	1.06	3.39
iso(corr)	-1.66	-0.119	-1.80	1.04	-1.78	-2.40	0.0252	-1.16	-1.19	1.93
rhad1	-0.00123	-0.0000581	-0.000561	0.00252	0.000919	-0.000194	0.00308	0.00140	0.000263	-0.000145
rhad	0.0000298	0.00502	-0.00138	-0.000828	0.000486	-0.000315	0.00409	0.000705	0.000417	-0.00404
E277	460	528	321	422	383	560	292	470	358	379
reta	0.942	0.948	0.949	0.926	0.964	0.956	0.957	0.942	0.957	0.927
rphi	0.947	0.961	0.967	0.950	0.975	0.965	0.965	0.956	0.957	0.952
weta2	0.0108	0.0107	0.00958	0.0108	0.00884	0.00928	0.00958	0.0108	0.00938	0.0114
f1	0.161	0.0416	0.250	0.215	0.139	0.0640	0.209	0.183	0.0997	0.175
fside	0.110	0.115	0.265	0.146	0.164	0.202	0.257	0.122	0.332	0.142
wstot	1.06	1.08	2.04	1.14	1.67	2.34	1.91	1.10	2.29	1.21
ws3	0.554	0.515	0.660	0.580	0.560	0.545	0.594	0.555	0.636	0.537
deltae	0	24	64	0	16	2	19	0	12	16
eratio	1	0.986	0.993	1	0.994	0.985	0.993	1	0.994	0.993
conv	No	No	Single	No	No	Single	Single	No	No	Single

Table B.1: Properties of the photons for the ten highest mass diphoton events observed in 2011 data. Energy values are given in TeV for the mass and GeV everywhere else. (`corr`) denotes values corrected by official tools; `Single` denotes single track conversions.

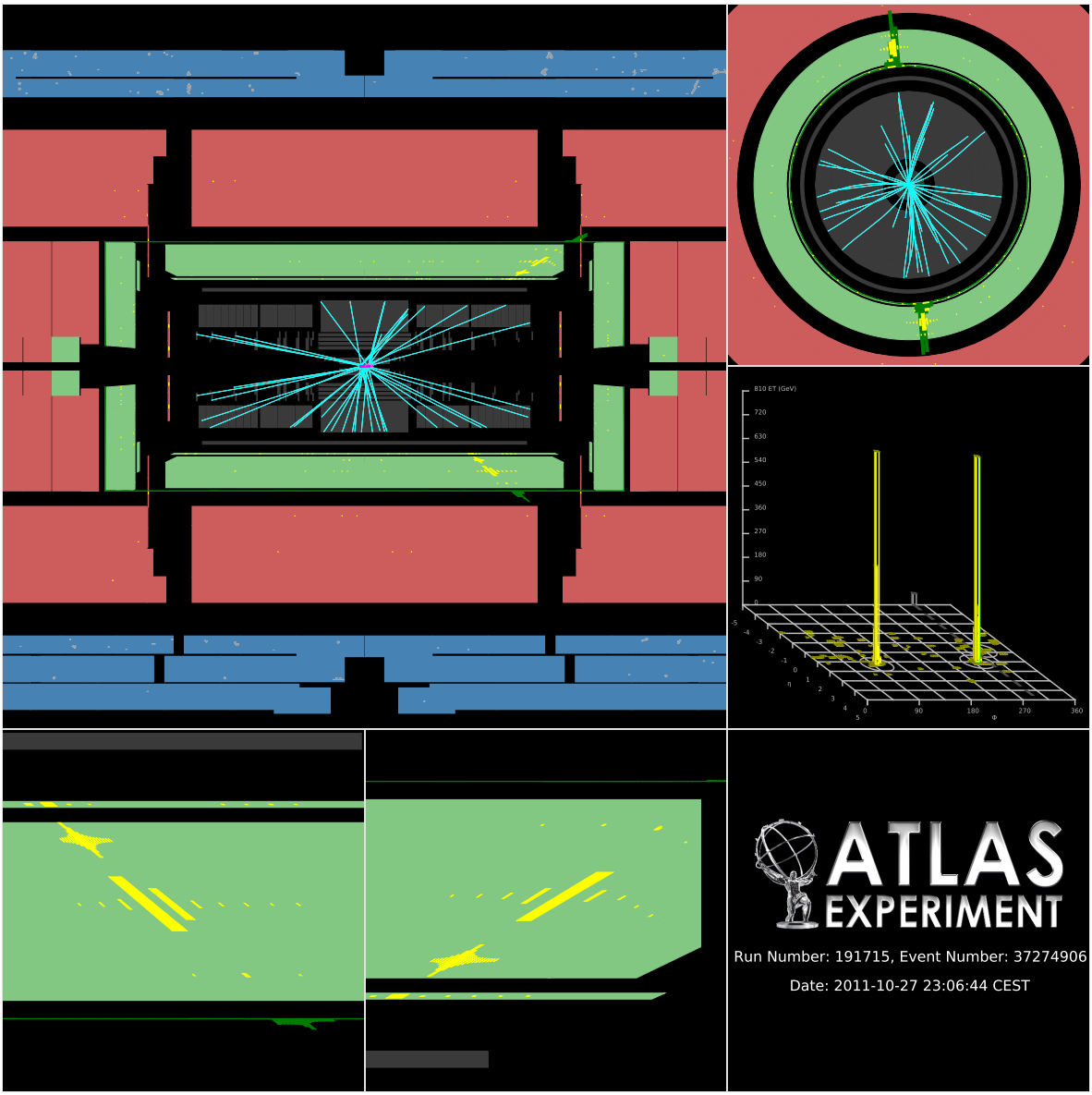

Figure B.1: Event display for the highest mass event. Tracks are shown above 1 GeV and calorimeter cells > 200 MeV.